RELATIVE NUMBER SQUEEZING IN A SPIN-1 BOSE-EINSTEIN CONDENSATE

A Thesis
Presented to
The Academic Faculty

by

Eva M. Bookjans

In Partial Fulfillment
of the Requirements for the Degree
Doctor of Philosophy in
Physics

School of Physics
Georgia Institute of Technology
December 2010

RELATIVE NUMBER SQUEEZING IN A SPIN-1 BOSE-EINSTEIN CONDENSATE

Approved by:

Professor Michael S. Chapman,
Advisor
School of Physics
Georgia Institute of Technology
Atlanta GA

Professor Chandra Raman
School of Physics
Georgia Institute of Technology
Atlanta GA

Professor Ken Brown
School of Chemistry & Biochemistry
Georgia Institute of Technology
Atlanta GA

Professor Jennifer Curtis
School of Physics
Georgia Institute of Technology
Atlanta GA

Professor Jean Bellissard
School of Mathematics and School of
Physics
Georgia Institute of Technology
Atlanta GA

Date Approved: November 12 2010

To my parents:

Christa and Gerhard Bookjans

ACKNOWLEDGEMENTS

I would like to take this opportunity to thank the people who have made the work in this thesis possible and have supported me throughout this endeavor. First, I would like to thank my thesis advisor Dr. Michael Chapman for not only providing me with opportunity to work in his laboratory but also for sharing his knowledge and advice.

I am very grateful to Dr. Ming-Shien Chang for introducing me to the Bose-Einstein condensate experiment. I would also like to thank Chris Hamley and Dr. Peyman Ahmadi, who worked on this experiment with me, for their collaboration, contributions, and invaluable help. I would also like to acknowledge former and present members in this research lab for their help and support: Dr. Ghazal Behin-Aein, Dr. Layne Churchill, Michael DePalatis, Dr. Kevin Fortier, Corey Gerving, Michael Gibbons, Thai Hoang, Soo Kim, Dr. Jacob Sauer, Chung-Yu Shih, Dr. Adam Steele, Qishu Qin. They have truly made my time at Georgia Tech a unique and unforgettable experience.

I would also like to express my thankfulness to all my friends and family, who have been part of this journey. Without their kindness, guidance, and unwavering support I would not be here today. I wish to thank Joanna Hass and Stephanie Barthe for their friendship and the good times we had together during these PhD years. A special thanks to my parents and brother for their constant support, which made me what I am today. I owe them so much. Last but no least, I would like to thank Jean Savinien for his relentless support and endless patience. I am fortunate to have him by my side as we journey through life together.

TABLE OF CONTENTS

LIST OF FIGURES

SUMMARY

The quantum properties of matter waves, in particular quantum correlations and entanglement are an important frontier in atom optics with applications in quantum metrology and quantum information. In this thesis, we report the first observation of sub-Poissonian fluctuations in the magnetization of a spinor ^{87}Rb condensate. The fluctuations in the magnetization are reduced up to 10 dB below the classical shot noise limit. This relative number squeezing is indicative of the predicted pair-correlations in a spinor condensate and lay the foundation for future experiments involving spin-squeezing and entanglement measurements.

We have investigated the limits of the imaging techniques used in our lab, absorption and fluorescence imaging, and have developed the capability to measure atoms numbers with an uncertainly < 10 atoms. Condensates as small as ≈ 10 atoms were imaged and the measured fluctuations agree well with the theoretical predictions. Furthermore, we implement a reliable calibration method of our imaging system based on quantum projection noise measurements.

We have resolved the individual lattice sites of a standing-wave potential created by a CO_2 laser, which has a lattice spacing of 5.3 μm. Using microwaves, we site-selectively address and manipulate the condensate and therefore demonstrate the ability to perturb the lattice condensate on a local level. Interference between condensates in adjacent lattice sites and lattice sites separated by a lattice site are observed.

CHAPTER I

INTRODUCTION

In a gaseous Bose-Einstein condensate (BEC), all the atoms occupy the same quantum state. In a simplified quantum mechanical picture, the atoms can be thought of as particles that simultaneously have a wave-like character described by the de Broglie wavelenth $\lambda_{dB} = h/\sqrt{2\pi m k_B T}$, where m is the mass of the particles, T is the temperature, h is the Planck constant, and k_B is the Boltzman constant. At high temperatures (e.g. room temperature), the de Broglie wavelength is very small and the atoms can basically be considered as classical point-like particles. As the temperature is lowered λ_{dB} increases and eventually becomes comparable to the inter-particle separation. At this temperature, the particles are no longer distinguishable and bosons start to form a Bose-Einstein condensate in which every particle posseses an identical spatial wavefunction; the coherent superposition of these wavefunctions results in a macroscopic coherent matter wave.

The experimental realization of BEC in 1995 [1, 2, 3, 4] was a very significant achievement in the field of atom optics. In analogy to a coherent optical field, a BEC can be considered as a source of coherent or "laser-like" atoms [5], which when coupled out of the trap form a so-called atom laser [6, 7, 8]. Although BEC is a quantum mechanical phenomenon, it can be described by a classical matter wave field just as a laser beam is described by a classical electromagnetic wave.

In the field of atom optics there recently has been much interest in the quantum properties of matter waves, in particular quantum correlations and entanglement. In analogy to quantum optics one could consider this the emergence of the field of quantum atom optics. A variety of fascinating experiments with ultracold atoms

have demonstrated nonclassical effects in atomic fields by studying noise correlations. These include the Hanbury-Twiss effect for bosons [9, 10], anti-bunching for fermions [11, 12], correlations in a Mott-insulator [13], and atom pair correlations from molecular disassociation [14] and from two colliding BECs [15]. Sub-Poissonian number fluctuations have been directly observed in a BEC [16, 17, 18, 19], in a Mott insulator [20], and in a degenerate Fermi gas [21] confirming the quantum statistics of these quantum degenerate gases. Besides giving insight into fundamental principles of quantum mechanics, correlated systems are predicted to have a wide range of applications such as quantum metrology and quantum information.

In quantum metrology, for example, measurements on an ensemble of uncorrelated particles are limited by quantum projection noise. This standard quantum limit (SQL) originates from the Heisenberg uncertainty principle and fundamentally limits the precision of measurements on independent atoms. However, by introducing quantum correlations this limit can be surpassed. Spin states that are correlated and demonstrate entanglement are defined as spin squeezed states (SSS) [22]. However, it is important to note that the spin-squeezing requirement for metrological gain is more stringent than for entanglement [23]. In dilute atomic gases, spin squeezed states were first realized by transferring entanglement of nonclassical light to atoms [24] and through quantum non-demolision (QND) measurements [25]. In a quantum non-demolision measurement, the nondestructive measurements project the system on a SSS. Using this method sub-projection noise measurements have successfully been made in atomic clocks [26, 27, 28] and in atomic magnetometry [29]. Sub-projection noise magnetometry has also been shown in a system of two entangled atomic ensembles [30]. In this case the entanglement was generated by a light pulse.

In order to generate spin-squeezing through a unitary transformation, the Hamiltonian requires a nonlinear interaction term [22]. In a Bose-Einstein condensate (BEC) the repulsive interaction between the atoms is nonlinear and can consequently

2

lead to spin squeezed states. A suppression of number fluctuations or so-called number squeezing has been indirectly observed in deep optical lattices and double-well potentials where the on-site interaction leads to the localization of exact atom numbers at the individual lattice sites indicating the realization of Fock states [31, 32, 33, 34, 35, 36]. The number squeezing in a lattice potential has been measured directly and spin-squeezing was verified [18]. The nonlinear interaction between the atoms has also been exploited to create spin-squeezed states of a two-component BEC, where the nonlinear interaction was controlled either by a Feshbach resonance [37] or by changing the overlap of the two components [38]. Both these experiments show that the classical precision limit (SQL) of a Ramsey interferometer can be surpassed and therefore demonstrate that spin-squeezed states have the potential of improving quantum metrology measurements, such as atomic clocks, which currently use Ramsey spectroscopy to define the current time standard.

In quantum optics, correlated photon pairs or entangled photon beams can be generated in nonlinear media through parametric down-conversion and four-wave mixing [39, 40]. These ideas have been extended to the field of atom optics and consequently have generated many proposals concerning the generation of atomic squeezed states and demonstrating nonlocal Einstein-Podolsky-Rosen (EPR) correlations. Examples of such proposals include [41, 42, 43, 44, 45, 46, 47, 48, 49], but the list is far from complete. In the collisions of two or three BECs [50, 15, 51, 52, 53] the atom-atom interactions play the role of the nonlinear medium resulting in the generation of the coherent matter waves. Similarly, molecular dissociation can be considered an analog to parametric down-conversion [14].

The experiments mentioned above exploit nonlinear elastic scattering processes to generate spin-squeezing. However, as proposed in [41, 42], spin-exchange collisions can also create spin-squeezing and pair correlations. In a spin-1 BEC, the atomic interaction not only has a density-dependent term but also a spin-dependent term,

which couples the different internal Zeeman levels and leads to spinor dynamics such as spin-mixing. For example, in a spin $F = 1$ BEC, spin-mixing occurs when two $m_F = 0$ atoms collide and become one $m_F = -1$ atom and one $m_F = 1$ atom or vice versa. This process also represents a type of four-wave mixing, and leads to correlated internal quantum states. A spin-1 ^{87}Rb condensate used as a magnetometer [54] has already shown to have a greater sensitivity per unit volume than superconducting quantum interference devices (SQUIDs). The spin-squeezing generated by spin-mixing is predicted to potentially reduce the variance of the atomic magnetization and nematicity as far as 20 dB below the standard quantum limits [55].

1.1   *Contributions of this Thesis*

In this thesis, we report on the direct observation of sub-Poissonian fluctuations in the magnetization of a spin-1 ^{87}Rb condensate after spin-mixing from a pure $F = 1, m_F = 0$ condensate. For $300 < \tilde{N} = N_{+1} + N_{-1} < 2300$ atoms in the $m_F = \pm 1$ states, the fluctuations in the magnetization $\Delta M = \Delta(N_{+1} - N_{-1})$ are reduced up to 10 dB below the classical shot noise limit. This is the first demonstration of sub-Poissonian spin statistics in a spin-1 condensate and provides a solid foundation for future experiments involving the demonstration of squeezing in a spinor condensate.

The detection of sub-Poissonian fluctuations requires an imaging system that can detect atoms with a noise under the atom shot noise limit, which is equal to $\Delta N = \sqrt{N}$ for N atoms. To reach this limit for small atoms numbers ($N \approx 100$), we improved our imaging system by implementing a high numerical aperture lens (NA = 0.31) and investigating the limits of the imaging techniques used in our lab, namely absorption and fluorescence imaging. As a result, we have been able to improve our imaging resolution to ≈ 3 μm and have developed the capability to measure atom numbers with an uncertainty < 10 atoms.

In order to demonstrate the sensitivity of our imaging techniques, we excite a small

fraction of a $F = 1, m_F = 0$ condensate to the $F = 2, m_F = 0$ ground state using microwaves. In this experiment, we have been able to image condensates as small as ≈ 10 atoms and the measured fluctuations agree well with the theoretical predictions given the imaging noise, quantum projection noise, and the fluctuations of the total atom number due to technical noise in the experiment. These measurements give us confidence in our understanding of imaging noise. By measuring both the atoms in the $F = 1$ and the $F = 2$ state, we can renormalize the number of atoms in the $F = 1$ state to the total atom number. This normalization eliminates the noise due to fluctuations of the total atom number and allows us to measure the quantum projection noise of the atoms in the $F = 2$ state. Furthermore, we implement a reliable calibration method of our imaging system based on quantum projection noise measurements in a spin-1 system.

With the improved resolution, we have been able to resolve the individual lattice sites of a standing-wave potential created by a CO_2 laser, which has a lattice spacing of 5.3 μm. Additionally, we have shown that we can address and manipulate the individual lattice condensates using microwaves. This single-site addressability allows us not only to reliably count the atoms in a single lattice site, but also to modify and perturb the condensate on a local level. We have verified the coherence of the site-selective state-transfer to the $F = 2$ hyperfine state by interfering adjacent lattice sites and lattice sites separated by one site. The visibilities of fringes in the interference pattern are on average 0.3 and 0.15, respectively.

In this thesis, we will start with the description of the experimental set-up and procedure (Chapter 2). Then we will present the theory and the limitations of the imaging techniques used in our lab, namely absorption (Chapter 3) and fluorescence (Chapter 4) imaging. In Chapter 5, we present the experimental parameters of the lattice BEC used in our experiments, our ability to address and manipulate single lattice sites, and the interference of two independent lattice condensates. In Chapter

6 we will explain the concept of quantum projection noise, present our initial imaging tests using small condensate in the $F = 2$ state, and describe a calibration method based on quantum projection noise. Before reporting on the observation of sub-Poissonian fluctuations in the magnetization (Chapter 8), we will provide a brief overview of the theoretical description of a spin-1 condensate (Chapter 7). Finally, we will give a summary of our results and give an outlook on future experiments (Chapter 9).

CHAPTER II

EXPERIMENTAL PROCEDURE AND SET-UP

The first achievements of Bose-Einstein condensation (BEC) in dilute atomic gases in 1995 [1, 2, 3, 4] was made possible by previous advances in laser cooling, in particular the first realization of a magneto-optical trap (MOT) in 1987 [56]. The MOT has remained an important and very popular tool in ultra-cold atomic physics due to its robustness and its ability to efficiently capture and cool millions of atoms at room temperature to the microkelvin regime. In almost all BEC experiments up to date, the atoms are pre-cooled using laser cooling techniques, before they are cooled to quantum degeneracy through evaporation. Although laser cooling methods, in general, do not produce atomic clouds cold and dense enough for the formation of BEC, they provide a very reliable cold atom source necessary for loading a sufficiently large number of atoms into the atom trap used for evaporation.

For the creation of a BEC, we use an all-optical approach, which was pioneered in our laboratory in 2001 [57] as an alternative to a magnetic trap. The efficiency of this all optical approach has since then been improved [58] and has proven to be a simple and fast approach for creating atomic BECs. Optical dipole traps have two important advantages over magnetic traps. Firstly, the trapping potential of optical dipole traps, unlike that of magnetic traps, does not rely on the internal spin state of the atoms. Under appropriate conditions, they are essentially spin-independent. They therefore have the capability to trap atoms or molecules that are not susceptive to magnetic trapping and are also well suited for studying internal dynamics, including spinor dynamics. Secondly, optical dipole traps can provide a large variety of different trapping geometries, such as multi-well potentials.
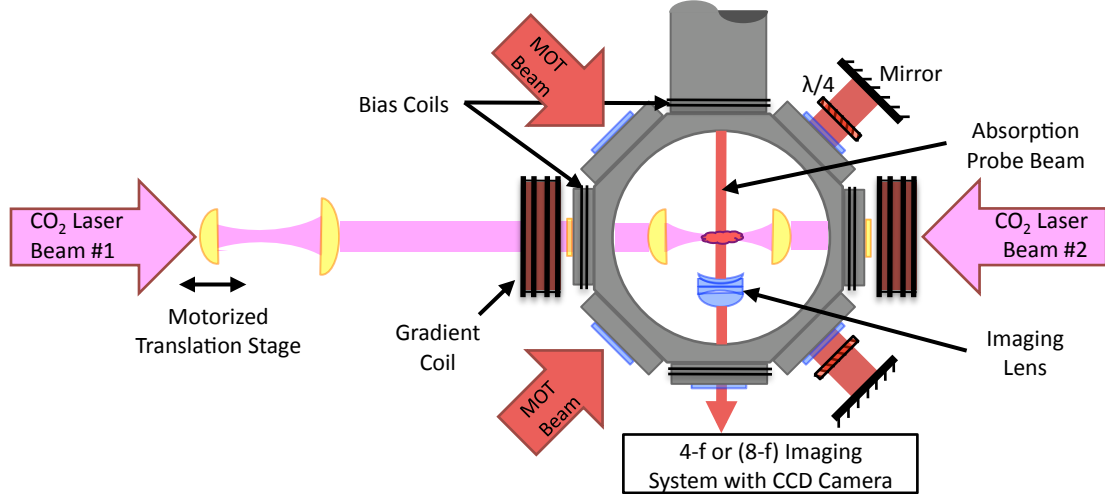
Figure 2.1: Simplified Schematic of the Experimental Set-up.

Our experimental procedure is almost identical to the one used in previous ^{87}Rb BEC experiments performed in our lab [58]. We start with a vapor cell MOT and then load the pre-cooled atoms into the single focus of a CO_2 laser. By compressing our CO_2 laser trap and reducing its trap depth, we evaporatively cool the atoms to BEC. This chapter briefly describes our experimental procedure and set-up. A simplified schematic of the experimental set-up is given is Figure 2.1.

2.1 Vacuum Chamber

BEC experiments require ultra-high vacuum in order to reduce collisions of the trapped ultracold atoms with the background gas. If the trap lifetime is shorter than the rethermalization rate during evaporative cooling, the trap will be depleted before BEC is reached. The pressure in our vacuum chamber is between low 10^{-10} and high 10^{-11} Torr giving us a vacuum limited trap lifetime of about 10 s. Since our evaporative cooling takes less than 3 s, this is sufficient for our experiments.

2.2 Atom Source

As a ^{87}Rb source we use a heated rubidium getter dispenser, which is turned on together with a UV-lamp. The UV-light induces atomic de-absorption (light induced

atomic de-absoprtion, LIAD) [59] from the glass windows of our vacuum chamber, which increases the background rubidium vapor pressure during the loading phase of the magneto-optical trap (MOT) (see Section 2.3) and as a consequence increases the number of atoms trapped. After the MOT is loaded both the dispenser and the UV-light are turned off, since for the remaining experimental steps a lower background pressure is favorable.

2.3 Magneto-optical Trap

Our experiments start with loading around 200×10^6 ^{87}Rb atoms from the thermal background gas into a standard magneto-optical trap (MOT), which consists of three orthogonal pairs of counter-propagating circularly polarized laser beams and a pair of anti-Helmholtz coils (MOT coils).

In Figure 2.2, we show the detailed hyperfine structure of the D_2 transition line of ^{87}Rb and highlight the transitions relevant for the MOT operation. The cooling beams of our MOT are detuned 25 MHz to the red of the $F = 2 \longleftrightarrow F' = 3$ cycling transition for Doppler laser cooling. They act as an optical molasses slowing down the atoms that enter the region of intersection. However, there is a small but non-negligible probability that the atoms are off-resonantly excited to the $F' = 2$ state and consequently decay to the $F = 1$ ground state. Once in the $F = 1$ ground state, the atoms no longer interact with the cooling beams and, as a result, are no longer cooled or trapped. We therefore, in addition to the cooling lasers, apply a repump laser resonant with the $F = 1 \longleftrightarrow F' = 2$ transition. The repump laser pumps the atoms that have decayed to the $F = 1$ ground state back into the cycling transition so they continue to be cooled. The typical intensity of our cooling beams is 35 mW/cm^2 and of the repump beam is 4.7 mW/cm^2 and the $1/e^2$ radius of the beams is 12.5 mm.

Our MOT coils provide a magnetic quadrupole field with a field gradient of about 7 G/cm along the axis of the coil, which creates a spatially varying Zeeman shift.

$F' = 3$

$5^2P_{3/2}$

266.650(9) MHz

72.9113(32) MHz

$F' = 2$

156.947(7) MHz

$F' = 1$

72.218(4) MHz

$F' = 0$

D_2

780.241 209 686(13) nm

Cycling Transition

Re-pump

$F = 2$

2.563 005 979 089 11(4) GHz

$5^2S_{1/2}$

6.834 682 610 904 29(9) GHz

$F = 1$
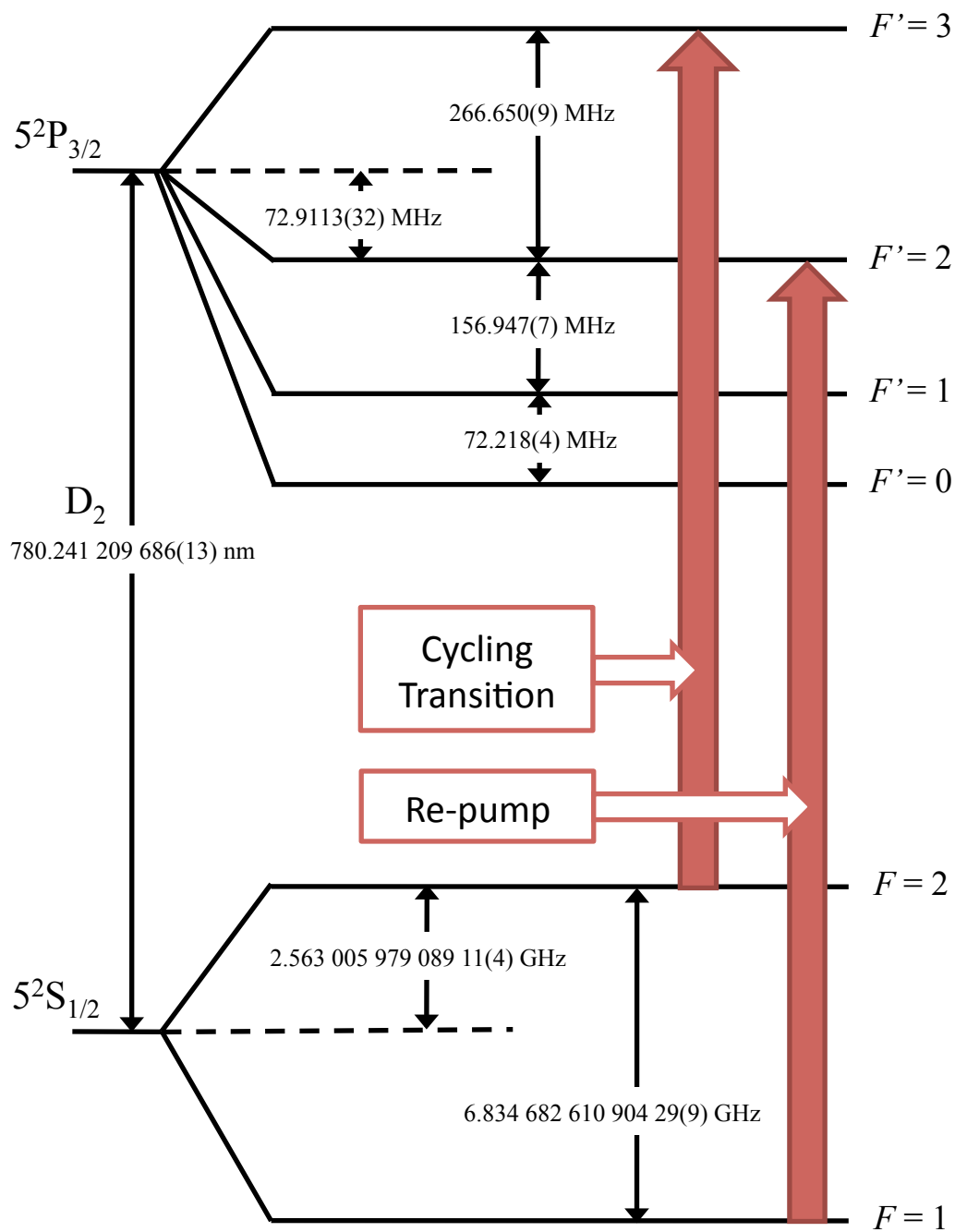
Figure 2.2: ^{87}Rb D_2 transition hyperfine structure [60]. The cycling transition and the re-pump transition are used to form a MOT.

The circular polarization of the cooling beams favors the $\sigma^\pm$ transitions ($\Delta m = \pm 1$) between the different Zeeman levels creating an imbalance in the scattering forces between the counter-propagating σ^+ and σ^- cooling beam. The handedness of the polarization of the three orthogonal pairs of σ^+ - σ^- cooling beams is chosen such that the resulting position dependent radiation pressure pushes the atoms to the center of the trap and therefore traps and confines the atoms.

For more details on the mechanism of a MOT see [61, 62], for instance.

2.3.1 Diode Lasers

The laser light for the MOT beams is generated by a system of laser diodes and a tapered amplifier (TA) [58], which are controlled by low-noise temperature and current controllers to ensure frequency stability. We use a master-slave configuration for both the repump and the cooling beams (see Figure 2.3 for a schematic of the cooling beam set-up). The diode lasers serving as master lasers are set-up with a diffraction grating (1800 lines/nm) in the Littrow configuration. The grating together with the diode creates an external cavity, which allows the linewidth of the laser to be reduced to below 1 MHz. The output frequency of the laser is fine-tuned by adjusting the cavity length with a piezoelectric actuator (PZT) mounted behind the grating.

For long-term frequency stability, the master laser is locked to an atomic transition of ^{87}Rb using frequency modulation (FM) spectroscopy on a saturated absorption signal. Figure 2.4 shows a typical saturation spectroscopy set-up and the resulting absorption and locking signals. We modulate the frequency of the laser light by a small amplitude high frequency signal either by dithering the injection current of the diode with a frequency $\sim$ 6 MHz (as in the case of our cooling laser master) or the RF frequency ($\sim$ 150 kHz) of an acousto-optic modulator (AOM) (as it is the case for our repump master). Near an absorption line the FM will cause a modulation of the absorption signal, which is detected by a photodiode. To first order, the
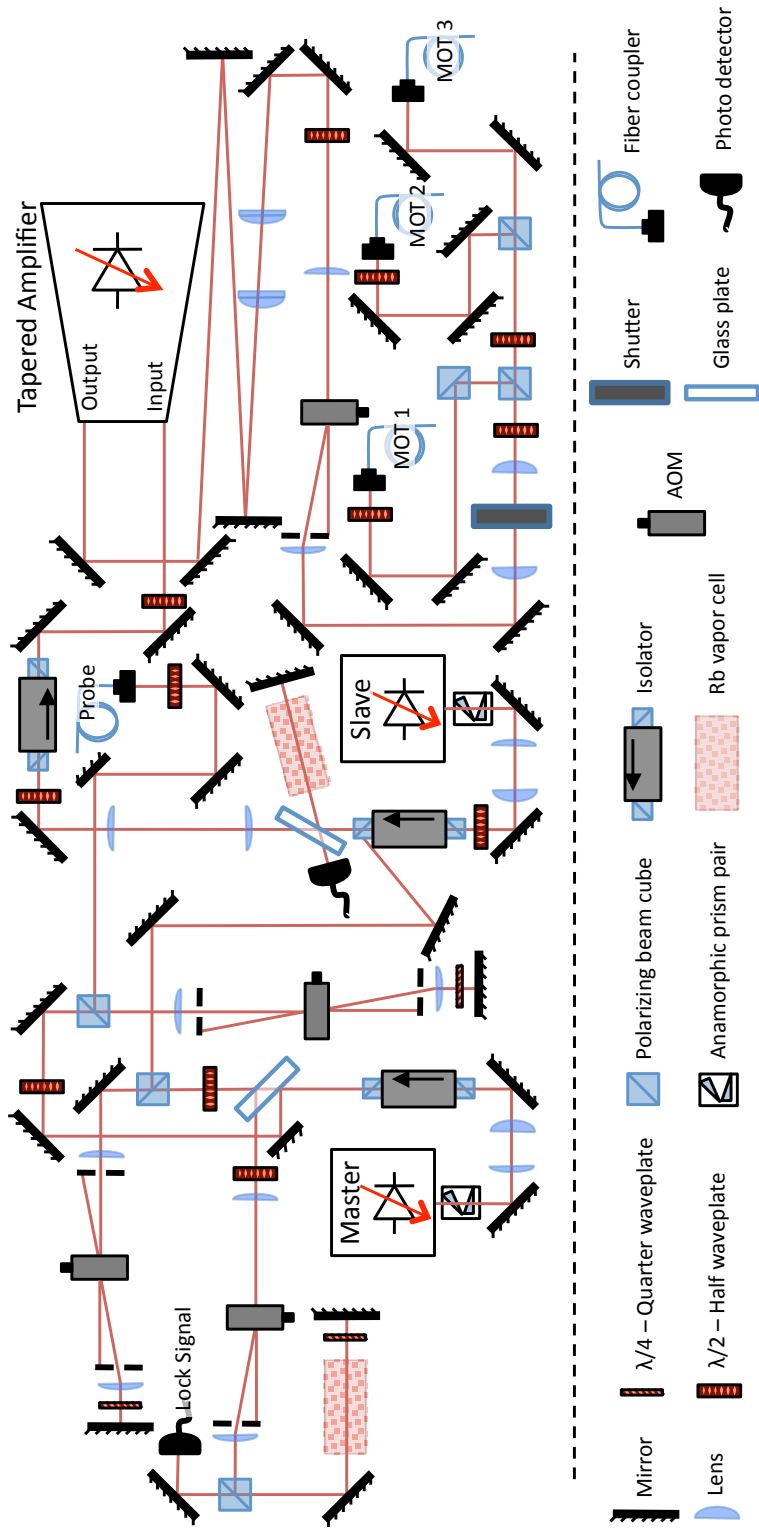
Figure 2.3: Schematic of the MOT laser set-up.

absorption signal contains a DC term, which corresponds to the absorption signal and a term oscillating at the modulation frequency, whose amplitude is proportional to the derivative of the absorption signal. By making a phase-sensitive detection relative to the modulating signal, we extract the derivative of the absorption signal. The resulting error signal is fed to a lock-box, which contains a PI (proportional-integral) controller. For optimal frequency stability, the proportional output is fed back to the injection current of the diode for fast adjustments with a bandwidth of up to 10 kHz and the integrator output is fed back to the PZT to compensate long term drifts of the laser frequency. A schematic of the locking set-up is shown in Figure 2.5. The master laser for the MOT is locked to the crossover of the $F = 2 \longleftrightarrow F' = 3$ and the $F = 2 \longleftrightarrow F' = 1$ transitions and the repump master is locked to the $F = 1 \longleftrightarrow F' = 2$ transition.

A slave laser, unlike the master, does not have a diffraction grating and is not actively stabilized using a lock circuit. Instead, the frequency of the slave diode is set by injecting a small amount of power (a few hundreds of microwatts) from the master laser into the slave diode. In order to prevent feedback into the master diode, the slave diode is seeded through the rejection port of an optical isolator. If the temperature and the current of the slave diode are adjusted properly, the frequency of the slave output will follow the injection frequency without mode-hops. To verify that the slave is stable and is properly coupled to the master, a small fraction of the slave laser light is sent through a saturation absorption set-up.

For the cooling beams of the MOT, the output of the slave laser ($\sim$ 30 mW) is seeded into a tapered amplifier (TA). The TA acts as a gain element, whose efficiency is determined by how well the seed is coupled into the amplifier chip (i.e. the spatial mode of the seeding beam), the power of the seeding beam, and the current driving the TA chip. It is not necessary to monitor the frequency output of the TA, since it acts merely as an amplifier and will, with proper injection, preserve the spectral
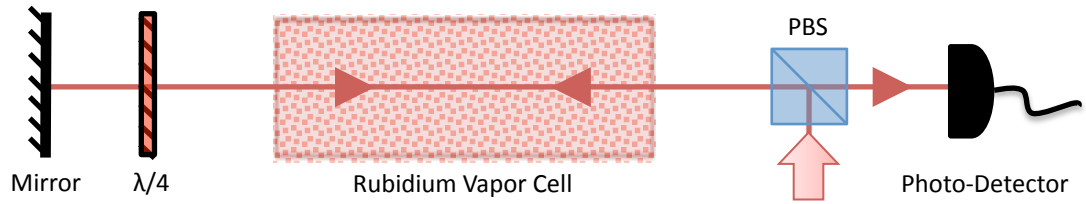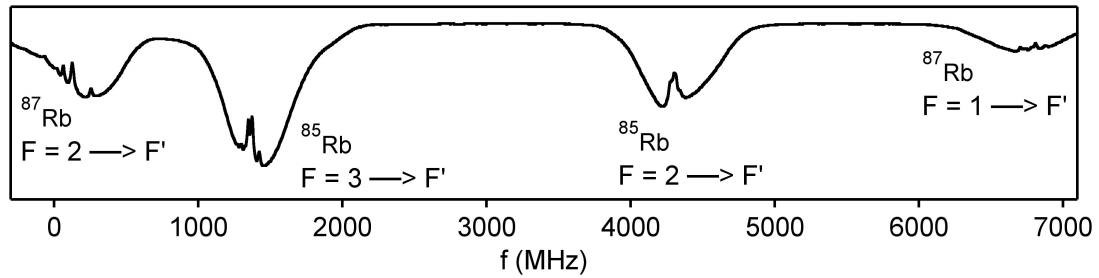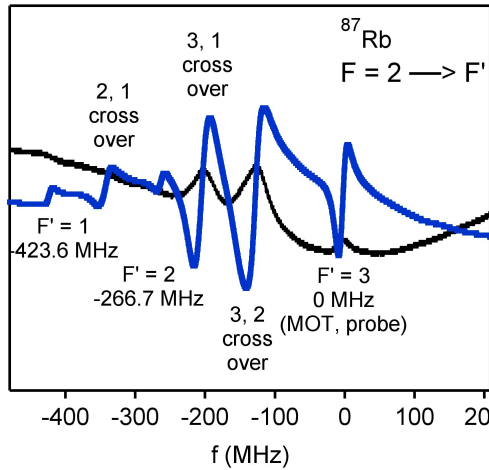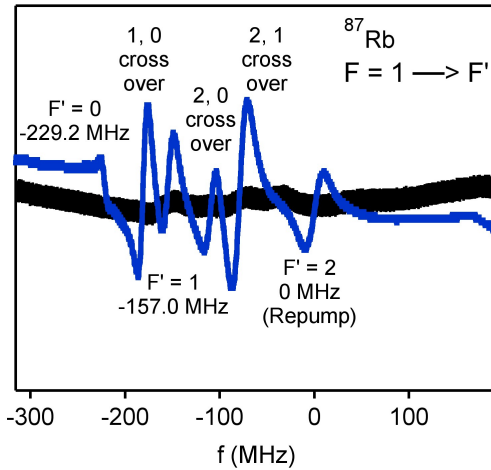
Figure 2.4: Saturation absorption spectroscopy set-up and spectra of the D_2 transitions. (a) A schematic of a typical saturation absorption spectroscopy set-up. (b) The spectra of the D_2 transitions of ^{85}Rb and ^{87}Rb. (c) The saturated absorption (black line) and FM (blue line) spectra of the $F = 2 \longleftrightarrow F'$ transitions for the ^{87}Rb. (d) The saturated absorption (black line) and FM (blue line) spectra of the $F = 1 \longleftrightarrow F'$ transitions for the ^{87}Rb.
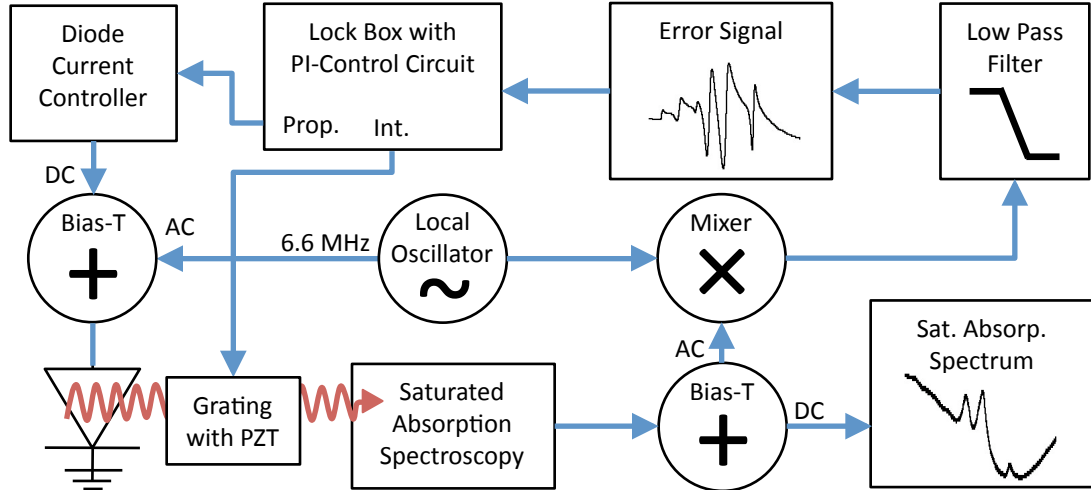
Figure 2.5: Schematic of the locking set-up.

properties of the injection laser. However, a tapered amplifier does emit a broad spectral background due to amplified spontaneous emission (ASE), which is emitted both in the forward and backward direction of the output direction. We operate the TA with an injection power above saturation to reduce the fraction of ASE but keep the injection power below 40 mW to prevent damages to the chip. For optimal seeding of the TA, the injection beam is mode-matched to the backward ASE of the TA. The optical isolators in our laser set-up prevent any unwanted feedback into the laser diodes or the tapered amplifier, which can cause them to become unstable or, in the worse case, cause permanent damage.

The acousto-optical modulators (AOM) in our set-ups are used as fast switches, to control the laser beam power, or to shift the frequency of the laser beam by externally controlling the radio-frequency (RF) power and the frequency to the AOM. In order to quickly shift the frequency during an experiment, an AOM needs to be set-up in a double-pass configuration (see Figure 2.6) to prevent the laser beam from steering, as the diffraction angle of the beam depends on the RF to the AOM. Such a double-pass configuration allows us to shift the frequency of our cooling beams from -5 MHz to -250 MHz relative to the cycling transition, which is crucial for the temporal dark
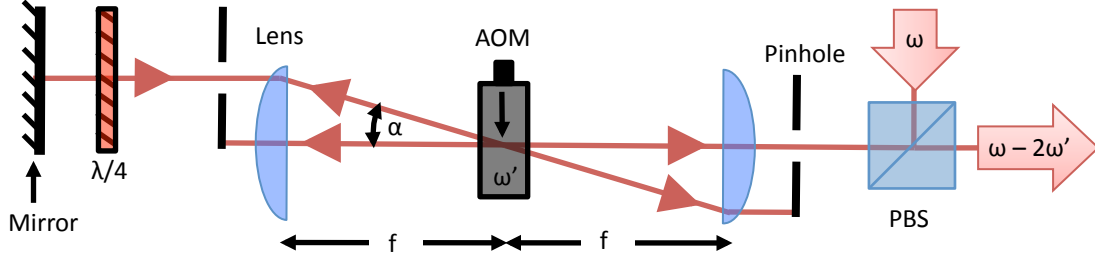
Figure 2.6: Schematic of a double passed AOM.

MOT during the final stage of the MOT.

2.3.2 Magnetic Coils

The magnetic fields and field gradients are controlled by three orthogonal pairs of Helmholtz coils (bias coils) and two pairs of anti-Helmholtz coils (gradient coils), respectively.

The bias coils are used to cancel ambient magnetic fields (such as the Earths magnetic field or other stray fields generated by equipment in lab) and to apply external magnetic fields necessary for the experiment. These bias coils, made of copper wire, are wrapped directly onto the flanges of the vacuum chamber keeping the experimental set-up compact and uncluttered. As a result, however, the coils are not in a perfect Helmholtz configuration.

The gradient coils used for the MOT formation are aligned along the direction of gravity. The position of the MOT, and consequently also its overlap with the CO_2 laser optical dipole trap, can be adjusted by moving the MOT coils relative to each other. In our set-up, the bottom MOT coil has a fixed height but can be moved left-right and in-out with a two dimensional translation stage, whereas the top MOT coil can only be moved up and down. The second pair of gradient coils is aligned along the CO_2 laser axis and allows us to address the single sites of a CO_2 laser lattice using microwaves (see Chapter 5.2.2). One of the coils is mounted on a 3D translation stage, so that the center of the gradient can be adjusted, while the other coil is kept

fixed.

Magnetic field gradients are also used for Stern-Gerlach experiments on the spinor condensate. The CO_2 laser dipole potential is turned off and the condensate falls under the influence of gravity. During this time of flight (TOF) of the condensate a magnetic field gradient is pulsed on, separating the different Zeeman states as they fall under gravity. As a result, the individual spin components, which are now spatially separated, are imaged and the spin populations of the condensate can be measured. The initial spin populations of the condensate can be controlled by applying different field gradients during the evaporation process. Generally, we use this technique to create either a pure $m_F = -1$ condensate or a pure $m_F = 0$ condensate. A pure $m_F = -1$ condensate is achieved by applying a magnetic field gradient (~ 25 G/cm) during the initial phase of the evaporative cooling. For a pure $m_F = 0$ condensate, we apply a magnetic field gradient of 25 G/cm during the final stage of the evaporation process removing the magnetic field sensitive spin projections from the trap.

Both set of gradient coils are made of copper refrigerator tubing and are water cooled as they can get very hot ($> 100°$ C) when run at full power without cooling. They are both mounted as close to the chamber as practical and their inner diameters are kept larger than the respective viewports so they dont reduce the optical access to the chamber.

2.4   Trap-loading and Evaporation

Our MOT is loaded for about 12 s, after which we implement a temporal dark MOT technique in order to maximize the transfer of atoms into the purely optical trap of the CO_2 laser. First, the intensities of the repump beam and the MOT beams are lowered to 15 μW/cm^2 and 20 mW/cm^2, respectively. Then, after 20 ms, the MOT coils are turned off and the MOT beams are detuned to the red of the trapping transition by 200 MHz for the last 40 ms of the dark MOT phase. As a result, the

atoms are optically pumped into the lower $(F = 1)$ hyperfine ground state. Since this state is decoupled from the MOT beams, the radiation pressure is reduced and higher densities can be achieved. This is a crucial step for efficient loading as it increases the effective overlap between the MOT and the optical dipole potential of the CO_2 laser. At the end of the dark MOT phase all lasers except the CO_2 laser are turned off. Using this technique, we typically load 12×10^6 pre-cooled atoms ($\sim 30 - 40 \ \mu K$) into an optical dipole trap formed by a single CO_2 laser beam of 60 W focused to a waist of 80 μm. Immediately after loading our optical dipole trap, we continue to cool the atom cloud using evaporative cooling until it condenses to a BEC. In evaporative cooling, the atoms with higher-than-average energy are removed from the trap, while the temperature of the remaining atoms decreases as they rethermalize through elastic collisions in the trap.

We force evaporative cooling by ramping down the power of our CO_2 laser. This lowers the trap depth of the confining potential and consequently expels the hottest atoms from the trap. Because a significant fraction $(> 99\%)$ of the trapped atoms is removed during the evaporation process, it is necessary to start with a sufficiently large number of atoms. Efficient evaporative cooling, however, also requires high atomic densities to ensure a fast rethermalization of the remaining atoms. The large initial waist of the single focus CO_2 laser creates a relatively large trapping volume, which is advantageous for loading but only provides weak confinement. In order to increase the atomic density, the trap is compressed immediately after loading by adiabatically reducing the waist of the CO_2 laser from 80 μm to 25 μm in less than 1 s. As a result, the total evaporation time is less than 2.3 s [63, 64, 58]. Just above the onset of quantum degeneracy, when the laser power of the single focus beam has reached about 60 mW, a second counter-propagating CO_2 laser beam is adiabatically ramped up to create a lattice potential. The trap depth of the lattice potential is then lowered until BEC is achieved creating an independent array of BECs. Typically, the

final power in each of the beams is $10-30$ mW. If we want to load a single lattice site, we use an additional tightly focused 850 nm diode laser perpendicular to the CO_2 laser trap axis to funnel the atoms to the position of the desired lattice site before ramping up the lattice potential. This cross-trap is turned off as soon as the lattice potential reaches its maximum depth.

2.4.1 CO_2 Laser Set-up

As mentioned above, the optical dipole trap used for evaporation and for trapping the BEC is generated by a CO_2 laser, which has a wavelength of 10.6 microns. Since this wavelength is very large compared to the resonance wavelength of the first excited state of ^{87}Rb (795 nm), the light field of a CO_2 laser can be regarded as a quasi-static electric field polarizing the atom. The dipole potential, as for all optical dipole traps, results from the dispersive interaction between the light field and the induced electric dipole of the atom. In the quasi-static approximation, the dipole potential is given by $U_{\text{dip}}(\vec{r}) = -\alpha_{\text{stat}} I(\vec{r})/2\epsilon_0 c$ with the static polarizability α_{stat}, and the intensity of the laser I [65]. For the ground state of ^{87}Rb the polarizability is given by $\alpha_{\text{stat}} = 5.3 \times 10^{-39}$ m^{2}C/V [60]. In the case of a quasi-electrostatic trap (QUEST), as created by a CO_2 laser, the scattering rate is negligible making it an essentially conservative trap. A ^{87}Rb atom trapped in a CO_2 laser with a trap depth of 100 μK, for example, scatters 1.1 photons per hour, while our experiments are conducted in less than 5 s.

The set-up of our CO_2 laser is shown in Figure 2.7. The output of the CO_2 laser that we use in our experiments (Coherent-DEOS GEM-100L) is about 100 W. We split off 5% of the beam power from our main beam in order to obtain a second counter-propagating beam for generating a lattice potential. The lattice spacing of the CO_2 laser lattice potential is 5.3 microns, which is sufficiently large to optically resolve the individual lattice sites and to address them individually [66]. Both beams
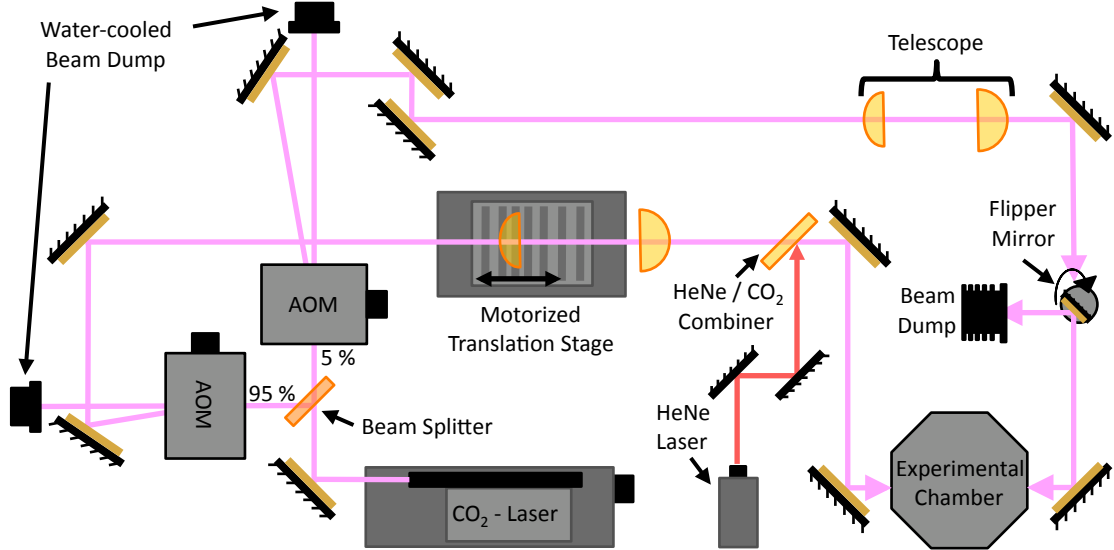
Figure 2.7: Schematic of the CO_2 laser set-up.

pass through acousto-optic modulators (AOMs), which allow us to independently control the power in each of the beams. The RF power to the AOMs, and thus the power in the corresponding CO_2 laser beams, are controlled using a variable gain amplifier and can be fully turned off using an RF switch. To ensure a frequency-stable lattice potential, we use the -1 diffraction order for both beams and use the same RF source for both AOMs. Following the AOM, the main CO_2 laser beam passes through an adjustable telescope and then enters the vacuum chamber, where it is focused onto the MOT with a 3.8 cm focal length aspheric lens. The first lens of the telescope is mounted on a motorized translation stage, so that the beam waist can be changed from large, for optimal loading, to small, for efficient evaporation. The second lens in the telescope and the third lens, the lens mounted in the chamber, remain fixed. The initial position of the first lens is chosen to maximize the trapping volume of the single focus trap for loading. As illustrated in Figure 2.8, this loading configuration is achieved by minimizing the size of the CO_2 laser beam at the third lens. To compress the trap for evaporative cooling, the first lens is moved toward the second lens of the telescope increasing the beam size at the third lens and therefore
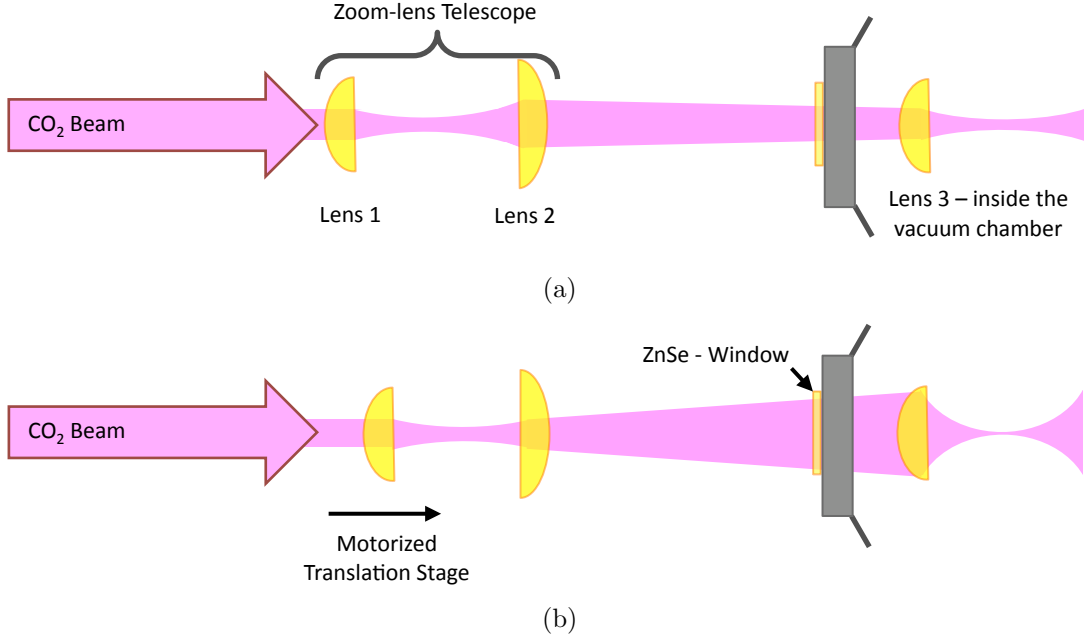
Figure 2.8: Schematic of trap compression mechanism due to the zoom-lens telescope. (a) The CO_2 laser is slightly converging after passing through a telescope formed by lenses 1 and 2. This results in a small beam radius on the input side of lens 3 and a large beam waist at the trap location. (b) After trap loading, the trap is compressed by increasing the beam radius at lens 3. This is done by moving lens 1 towards lens 2.

creating a tightly focused trap. The position of the trap moves about 1 mm as the beam waist of the trap is changed. The second beam used to generate the lattice potential also passes through a telescope before entering the vacuum chamber and passing through a 3.8 cm focal length aspheric lens. The telescope is used to adjust the location of the beams focus inside the chamber, so that it overlaps with the focus of the compressed single focus trap.

2.5 Microwave and RF source

We manipulate the spin state of the condensate using microwave and/or radio frequency (RF) radiation. In order to be able to control the transitions between the different Zeeman levels in the $F = 1$ and $F = 2$ hyperfine ground states, we apply an external magnetic field during the microwave or RF pulse. This lifts the degeneracy of
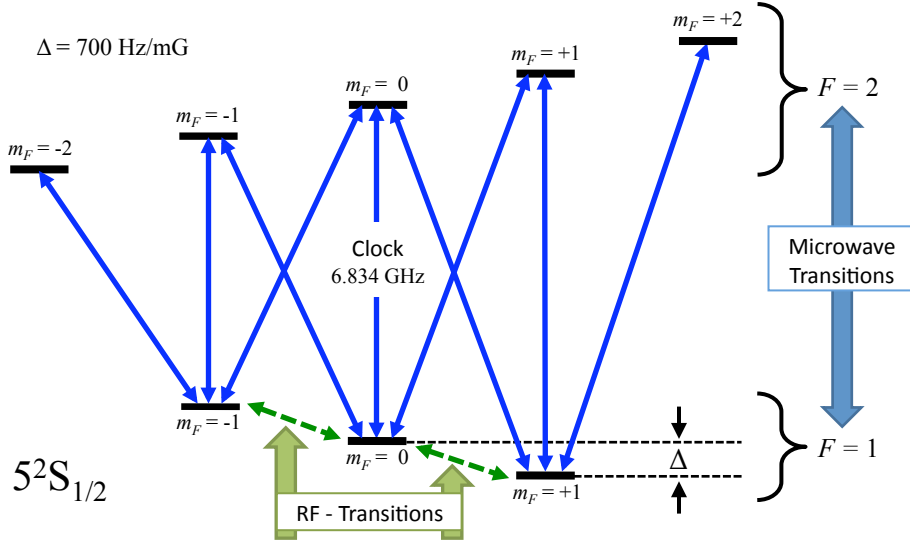
Figure 2.9: Zeeman splitting of the hyperfine ground states. The magnetically allowed transitions between the $F = 1$ and $F = 2$ states are indicated with blue solid arrows. The dashed green arrows show the RF transitions within the $F = 1$ manifold.

the Zeeman levels ensuring that they are spectroscopically resolvable. The microwave radiation is tuned to the hyperfine splitting of the ground state (≈ 6.835 GHz) and is used to drive transitions between the $F = 1$ and $F = 2$ states, whereas the RF radiation is used to drive transitions within the $F = 1$ hyperfine manifold. The capability to apply both RF fields as well as microwave fields allows us to create arbitrary coherent superpositions of the Zeeman states in the $F = 1$ and $F = 2$ ground states.

The exact dependency of the Zeeman shift on the magnetic field is given by the Breit-Rabi formula (see [60] or Equations 7.7 for the $F = 1$ ground state). For low fields, the shifts are linear with the magnitude of the magnetic field to first order, and are given by $\mp m_F \cdot 0.7$ MHz/G for the $F = 1$ ($F = 2$) manifold, respectively. Figure 2.9 shows the Zeeman splitting of the ground $F = 1$ and $F = 2$ hyperfine states for low magnetic fields, and indicates the magnetically allowed transitions. Since we know that dependence of the Zeeman energy levels on the magnitude of the magnetic field, we can measure the magnetic field by taking a microwave spectrum.

The microwave radiation is generated by a frequency synthesizer (HP E4422B),
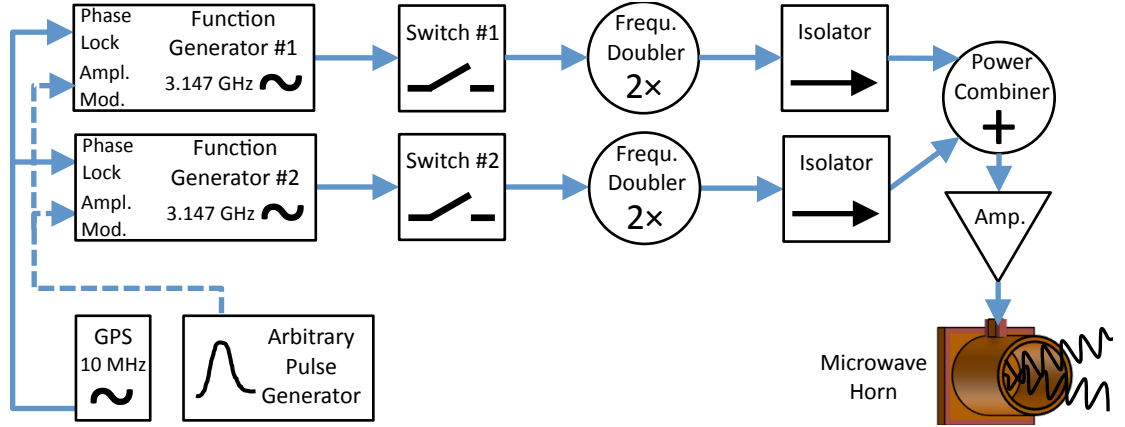
Figure 2.10: Schematic of the microwave set-up.

which is referenced to a global positioning system (GPS) stabilized quartz oscillator (EndRun Technology Præcise Gfr.). It is then doubled (Marki Microwave D0204LA), amplified (Mini-Circuits ZFL-7G and Varian TWT VZC6961K1DFGJ), and is finally directed towards the condensate using a homemade cylindrical horn (see [58]. The set-up is illustrated in Figure 2.10. We use two microwave generators in order to be able to pulse on two different microwave frequencies and/or powers in rapid succession as it takes over 500 ms to set the output of the frequency synthesizer using computer control. In order to apply a simple square pulse, the microwave radiation is turned on and off using a fast switch (Mini-Circuits ZYSWA-2-50DR) with a pulse generator (Stanford Research Systems DG535) after the frequency and the amplitude of microwaves has been set with the function generator. The frequency spectrum of a square pulse is proportional to the sinc-function ($\mathrm{sinc}(x) \equiv \sin x/x$). To change the frequency spectrum to a more Gaussian shape without the "feet" of the sinc-function, we shape the amplitude of the pulse by modulating the output of the function generator with an arbitrary pulse generator (Stanford Research Systems DS 345). The desired pulse shape is pre-programmed into the pulse generator.

The RF radiation is generated by a homemade coil, which is driven by a frequency generator (Standford Research System DS345). The coils is made of 2 turns and has
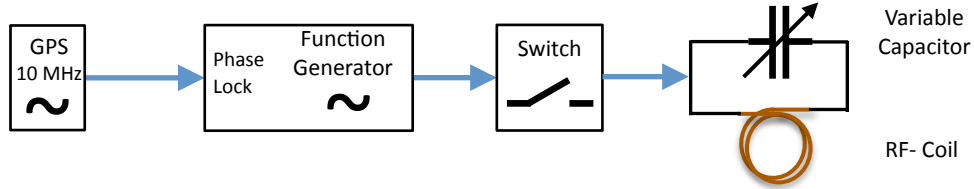
Figure 2.11: Schematic of the RF set-up.

a diameter of 8.9 cm. The coil is put in parallel with an adjustable capacitor to maximize the transmission of the radiation for a given frequency and prevent over-heating. The capacitor value for a given frequency is determined by maximizing the amplitude of the RF. Again, we use a switch (Mini-Circuits ZYSWA-2-50DDR) to pulse on the radiation. A schematic of the RF set-up is shown in Figure 2.11.

2.6   Imaging

We probe the atomic cloud using either fluorescence or absorption imaging. In both imaging methods, the atoms are illuminated with laser light tuned to the cycling transition. We simultaneously pulse on the repump laser, in order to image the atoms in the $F = 1$ state or to prevent the atoms from leaving the cycling transition. For fluorescence imaging we use the MOT beams to probe the atoms, whereas for absorption imaging we use a separate probe beam. More details on absorption and fluorescence imaging are given in Chapters 3 and 4, respectively.

To diagnose the MOT and the efficiency of our trap-loading, we use fluorescence imaging with a 1:1 imaging system. The signal is recorded on a CCD camera that is mounted diagonally above the chamber. The probe time is 100 μs.

The imaging set-ups used for taking higher quality images are shown in Figure 2.12. The images are recorded on with a high performance scientific CCD camera. The models of the cameras used are Andor iXon DV887DCS-UV and Andor iKon-M DU934N-BR-DD). The imaging lens has a focal length of 50 mm (Linos HALO 03 8904) and is mounted inside the chamber. The next lens is adjusted such that the
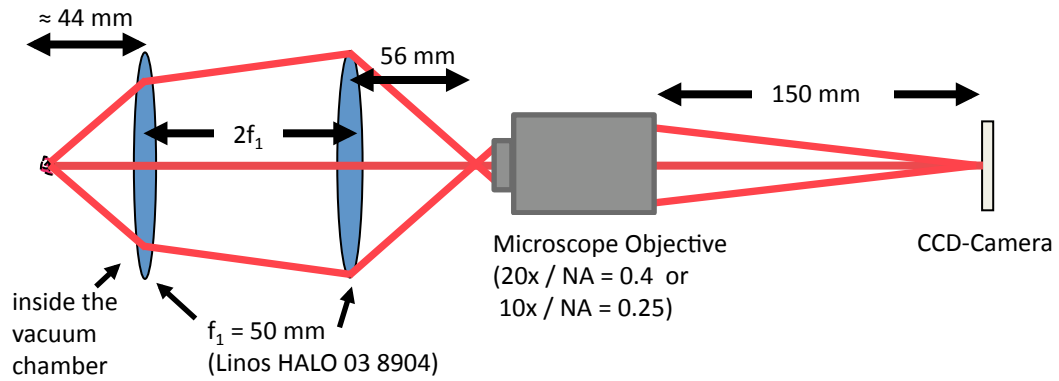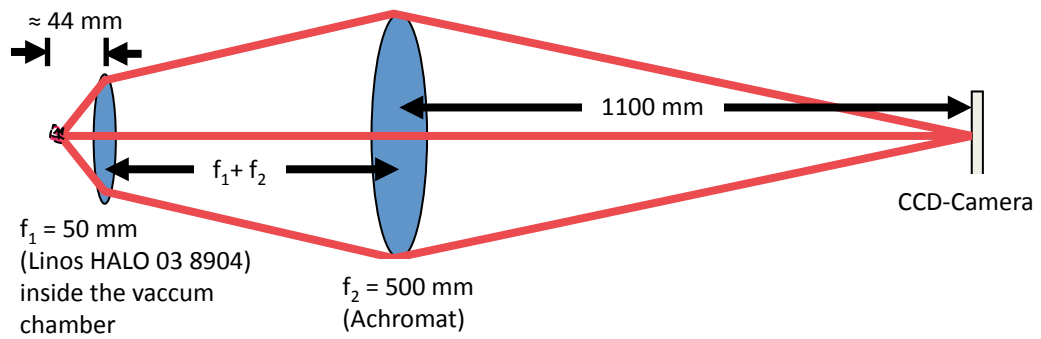
Figure 2.12: Schematic of our imaging set-ups. (a) shows the imaging set-up used for the experiments described in Chapter 5. The magnification can be changed by using different microscope objectives. (b) shows the imaging set-up used in the rest of the thesis. The magnification of the imaging system is $10\times$.

absorption probe beam is re-collimated after this lens. The set-up allows us to probe the atomic cloud both with fluorescence and absorptive imaging.

CHAPTER III

ABSORPTION IMAGING

Quantum degenerate gases are traditionally imaged using absorption imaging because this method provides a reliable image of the density distribution of the atom cloud and therefore can give insight into the physical properties of the ultracold atom cloud. For example, in the first BEC experiments the existence of a condensate was confirmed by absorption images of the atom cloud after its release from a non-spherical trap [1, 2]. The density distribution showed an anisotropic expansion, which is characteristic for a BEC and is absent in a thermal cloud (which expands isotropically independent of the trap shape). Even today, the achievement of quantum degeneracy is usually verified through a measurement of the density distribution of the atom cloud either after a ballistic expansion or within the trap. Absorption imaging therefore continues to be an important tool for probing ultracold atom clouds. The increasing interest in quantum correlations has motivated the improvement of absorption imaging. For example, atom pair correlations from molecular disassociation [14] were demonstrated by measuring density-density correlations in an atom cloud. Another example includes the observation of sub-Poissonian number fluctuations and spin-squeezing in a BEC [18], which required measuring the number of atoms in two adjacent lattice sites. In this experiment, the atom noise was reduced to 10-12 atoms. Fluorescence imaging does not provide the same spatial resolution as absorption imaging because the atom cloud is generally distorted and blurred during the imaging. As a result, fluorescence imaging is not usually used to measure local density fluctuations.

In order to measure small number of atoms (< 100), fluorescence imaging is generally used because it provides a higher signal-to-noise ratio in this regime. For example, in the experiment described in [16], both absorption and fluorescence imaging are employed. For atoms numbers of order 1000 or larger, absorption imaging is used, whereas for lower atom numbers fluorescence imaging is used. In order to probe the small condensates using fluorescence they are, in this case, transferred into a MOT and are probed for 100 ms. This technique is capable of detecting atoms at the single atom level. Other experiments that have demonstrated the ability to detect single atoms using fluorescence imaging include [67, 68, 69]. In all the examples mentioned, the atoms are held in tight traps and are probed for long times (from ~ 100 ms to ~ 1s).

We investigate the limits of both of these imaging methods, in order to determine the imaging method that gives us the best signal-to-noise for our experiment.

In absorption imaging the atoms are illuminated by a single probe beam and the shadow cast by the atoms is imaged on the CCD camera (see Figure 3.1). As the probe beam passes through the atom cloud, the atoms absorb photons out of the probe beam reducing its intensity. The atom cloud is, in this case, detected by imaging the transmitted probe beam intensity I'. To quantify the fraction of light that is transmitted, it is necessary to additionally take a reference image of the probe beam profile, i.e. an image without the atoms I_0. This chapter describes the theory, calibration, and limitations of absorptive imaging. The derivation for the theory is based on [62, 70].

3.1 Theory

Consider a beam of light with uniform intensity I and angular frequency ω incident on a cloud of atoms with a uniform density n. As the light passes through an infinitesimal slice of the cloud with thickness Δz, the atoms absorb photons out of the beam with
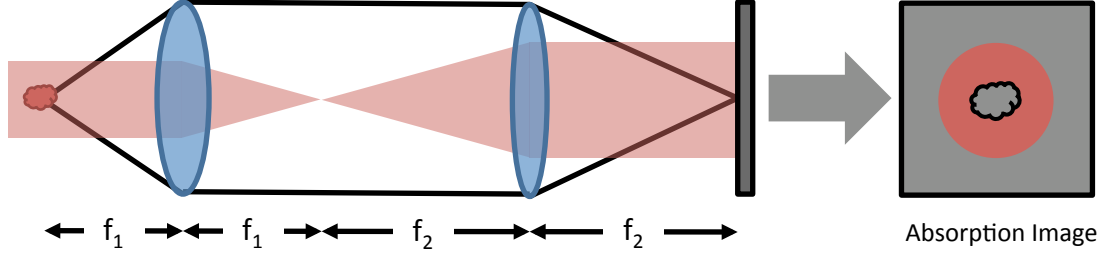
Figure 3.1: Schematic of the absorption imaging set-up.

the probability $n\sigma(\omega)\Delta z$, where $\sigma(\omega)$ is the absorption cross-section. The absorption cross-section characterizes the probability that a photon is absorbed by an atom. In a simple model, it can be interpreted as the target area covered by an atom, i.e. the light "sees" the atom as a disk with area $\sigma(\omega)$ (see Figure 3.3). The absorption cross-section depends on the angular frequency of the incident light ω and is maximum for on-resonant light $\sigma_0 = \sigma(\omega_0)$. The fraction of intensity that is lost as the beam passes through the thin slice corresponds to the absorption probability $\Delta I/I = -n\sigma(\omega)\Delta z$. Consequently, the attenuation of the beam due to the atoms can be described by

$$\frac{dI}{dz} = -n\sigma(\omega)I = -\kappa(\omega)I, \tag{3.1}$$

where $\kappa(\omega)$ is the extinction coefficient. This equation is also known as Beer's law [71].

Beer's law only applies to the limit of low-intensity light that leaves most of the atom population in the ground state ($N \approx N_g$). For intense light, however, a significant fraction of the atom population is excited out of the ground state reducing the probability of absorption. Additionally, once in an excited state, an atom can undergo stimulated emission, which leads to a gain in intensity. For a two-level system, the rate of stimulated emission is equal to the rate of absorption. The two processes therefore have the same cross-section ($\sigma(\omega)$) and equation 3.1 can be modified to take into account saturation effects:

$$\frac{dI}{dz} = -\kappa(\omega)I = -(n_g - n_e)\sigma(\omega)I, \tag{3.2}$$
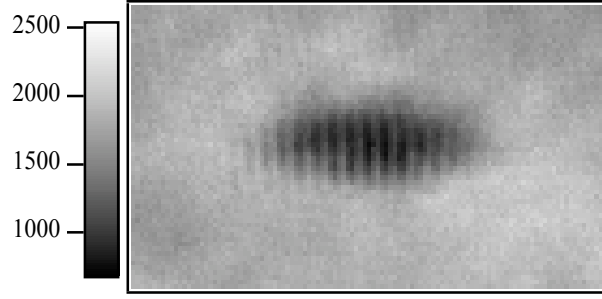
(a)
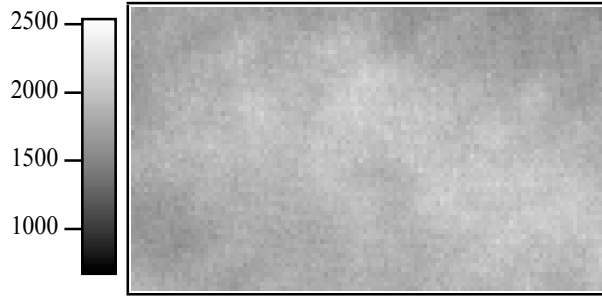
(b)
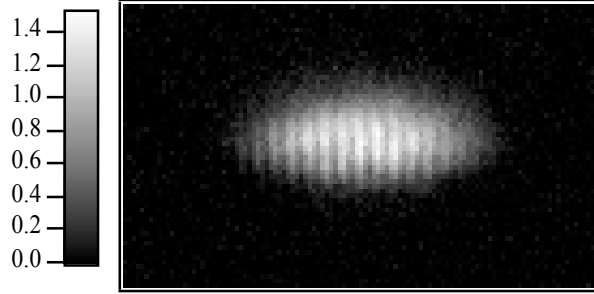
(c)

Figure 3.2: Example of the raw data images taken in absorptiom imaging in order to obtain an image of the atoms. (a) is an image of the shadow that the atom cloud casts on the probe beam profile. This image is referred to as the signal image. In order to determine the fraction of light the atoms absorb, it is also necessary to take a reference image of the atom cloud (c), i.e. an image of the probe beam profile without the atoms. (c) is an image of the atoms in units of the optical depth OD, which is determined using Equation 3.9. This image shows the interference of two lattice sites of a BEC after a time of flight of 7 ms, where the total number of atoms is $N = 7800$. The image was taken with a probe power $I_0 \approx I_{sat}^0$ and with a probe time of 100 μs. The field of view is 176 x 96 μm^2.

σ - absorption crosssection

I'

$\Delta I = - n \, \sigma \, I_0 \, \Delta z$

n - atom density

I_0

Δz
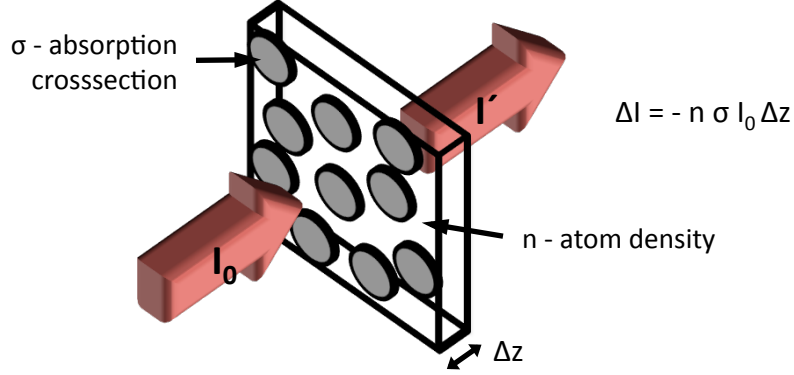
Figure 3.3: Illustration of the theory behind absorptionimaging

where n_g is the density of the atoms in the ground state and n_e the density of the excited state.

The conservation of energy requires that the energy absorbed is equal to the energy emitted. In the steady state, this corresponds to

$$n_g \sigma(\omega) I(\omega) = n_e \sigma(\omega) I(\omega) + n_e \Gamma \hbar \omega. \tag{3.3}$$

Γ is the decay rate of the excited state, i.e. the rate of spontaneous emission. Given the conservation of atom numbers $n = n_e + n_g$, equation 3.3 can be re-written as

$$n_g - n_e = n \frac{1}{1 + \frac{I(\omega)}{I_{sat}(\omega)}}, \tag{3.4}$$

with the saturation intensity I_{sat} for a two-level atom defined by

$$I_{sat}(\omega) \equiv \frac{\frac{\Gamma}{2} \hbar \omega}{\sigma(\omega)}. \tag{3.5}$$

Using equations 3.3 and 3.4, we can relate the attenuation of the incident beam to n, the total atom density of the cloud. For resonant incident light, Beer's law in the presence of saturation can therefore be expressed as

$$\frac{dI}{dz} = -n\sigma_0 \frac{1}{1 + I/I_{sat}^0} I, \tag{3.6}$$

where $\sigma_0 = \sigma(\omega_0)$ is the on-resonance absorption cross-section and $I_{sat}^0 = I_{sat}(\omega_0)$ is the on-resonance saturation intensity.

30

In general, the atomic density of the ultracold cloud is not uniform but varies in space $n(x, y, z)$. Similarly, the intensity profile of the probe beam is not necessarily uniform $I = I(x, y, z)$. In this case, the probe beam can be regarded as a collection of rays, each of which has a uniform intensity and each of which interacts with a separate small region of the atom cloud with a uniform density. Beer's law applies as long as the path of each ray through the cloud is known and its attenuation can be measured. Ideally, each of the rays enter and exit the cloud at the same (x, y) coordinates such that the attenuated ray (measurement with atoms) and the unattenuated ray (reference measurement without atoms) follow the same path through the imaging system and hit the CCD camera at the same location. Integration of equation 3.6 gives the expression of the optical depth

$$OD(x, y) \equiv \sigma_0 \tilde{n}(x, y) = -\ln \frac{I'(x, y)}{I_0(x, y)} - \frac{I'(x, y) - I_0(x, y)}{I_{sat}^0}, \qquad (3.7)$$

where $\tilde{n}(x, y) = \int n(x, y, z) dz$ is the column density, $I'(x, y)$ $(I_0(x, y))$ is the intensity profile of the incident probe beam without (with) the atoms. In the low-intensity limit $(I' << I_{sat}^0)$, the optical depth (defined in Equation 3.7) reduces to the optical density, which is defined as

$$od(x, y) \equiv -\ln \frac{I'(x, y)}{I_0(x, y)}. \qquad (3.8)$$

The local column density $\tilde{n}(x, y)$ can be determined by imaging the probe beam on a CCD camera in the presence and in the absence of the atoms. The two above images are referred to as the signal $S'(x, y)$ and reference $S_0(x, y)$ image, respectively. In practice, however, it is also necessary to take a third image, a background image $S_b(x, y)$ without the probe beam. By subtracting this background from both the signal and the reference image, contamination of the probe image due to stray light and the camera background is eliminated. Without correcting for the background, the column density would be underestimated. In terms of the actual measurements

31

made, the local column density is determined by

$$\tilde{n}(x, y) = \frac{OD(x, y)}{\sigma_0} \tag{3.9a}$$

$$OD(x, y) = -\ln\left(\frac{S'(x, y) - S_b(x, y)}{S_0(x, y) - S_b(x, y)}\right) - \frac{S'(x, y) - S_0(x, y)}{I_{sat}^0}, \tag{3.9b}$$

where I_0^{sat} is in units of camera counts. For low-intensity imaging, only the relative transmission $T(x, y) = \frac{S'(x,y) - S_b(x,y)}{S_0(x,y) - S_b(x,y)}$ is measured. In this case, the conversion of photons to camera counts is irrelevant, i.e. the column density can be determined without knowing the camera efficiency, the losses through the imaging system, or the solid angle.

Furthermore, the local column density can be integrated in order to obtain the total number of atoms N, *i.e.* the column densities of the individual camera pixels are summed up

$$N = \int \tilde{n}(x, y) dx dy = \sum_{pix} \tilde{n}_{pix} dA_{pix} = \frac{A_{pix}}{\sigma_0} \sum_{pix} OD(pix), \tag{3.10}$$

where $OD(pix)$ is the optical depth measured at a given pixel, $A_{pix} = A_{pix}^{act}/m^2$ is the effective area of a pixel, m is the magnification of the imaging system, and A_{pix}^{act} is the physical area of a camera pixel.

3.2 Limitations

In this subsection we discuss potential limitations of absorption imaging.

3.2.1 Optically Dense Clouds

In the derivation of the optical depth, we have assumed that the atomic cloud is dilute enough so that atoms in the next layer of thickness Δz are not in the shadow of the previous layer. In optically thick clouds, the atoms can "hide" behind the previous atoms and therefore do not interact with the probe light. This will cause a reduction in the absorption signal. Additionally, we have ignored the fact that the photons scattered out of the probe beam can be reabsorbed by other atoms in the cloud. The

rescattering of photons causes the atoms to spend more time in the excited state and therefore to absorb less photons from the probe beam. This rescattering of photons is more likely for denser clouds and can be neglected for optically thin clouds.

Optically dense clouds can also magnify errors caused by other limitations of the imaging system, for example the the maximum observable optical density (see Section 3.2.6). These effects will be discussed separately in the individual subsection. In order to ensure a proper counting of the atoms, we therefore generally let the condensate expand to an optical depth of ≤ 2.

3.2.2 Atom Motion

The above derivation of the optical depth did not take into consideration the motion of the atoms. For a condensate, the assumption that the atoms are stationary is, in general, valid. However, the condensate is often imaged after a time of flight t of several ms. As the condensate falls under the influence of gravity, it will gain a velocity $v = gt$ with $g = 9.8$ m/s. For a probe time τ and a transverse observation to, this causes the image to blur by $z = v\tau$. For a time of flight of $t = 10$ ms and a probe time $\tau = 100$ μs, $z = 9.81$ μm.

Besides blurring the image, any motion of the atoms along the probe beam can Doppler-shift the atoms out of resonance. This can become a problem as the atoms are heated during imaging (see Subsection 3.2.4). The effect of the atom's motion on the absorption can be taken into account by using the Doppler-shifted cross-section $\sigma(\omega - \vec{k} \cdot \vec{v})$, where $\vec{k}$ is the wavevector of the probe beam and $\vec{v}$ the velocity of the atom. For a two-level system, the absorption cross-section is given by

$$\sigma(\Delta) = \sigma_0 \frac{1}{1 + \left(\frac{2\Delta}{\Gamma}\right)^2}, \tag{3.11}$$

where $\Delta = \omega - \vec{k} \cdot \vec{v}$ is the detuning and Γ is the linewidth of the two-level system. If the atoms a velocity of 2.4 m/s along the direction of the probe beam, the absorption cross-section is reduced by 50% as a result of the Doppler effect. If the atoms have

a velocity distribution $f(\vec{v})$, the correct absorption cross-section can be determined by $\sigma_{corr}(\omega) = \int f(\vec{v})\sigma(\omega - \vec{k} \cdot \vec{v})d\vec{v}$, where the integration goes over all velocities. The reduction in the absorption cross-section can be corrected by replacing the ideal absorption cross-section with an effective cross-section $\sigma_{eff} = \sigma_0/\alpha$ in Equation 3.7 and keeping in mind that $I_{sat}^{eff} = \alpha I_{sat}^0$. More details on this method of correction are given in Section 3.3.

3.2.3 Dispersion

The interaction of the atoms with light can be described by the complex index of refraction of the atoms $n_{ref} = \sqrt{1 + 4\pi n\alpha}$, where α is the static polarizability and n the density of the atoms. For a two-level system (in the rotation wave approximation) the index of refraction $n_{ref} - 1 \ll 1$ can be written:

$$n_{ref} = 1 + \frac{\sigma_0 n}{2k}\left[\frac{i}{1 + \delta^2} - \frac{\delta}{1 + \delta^2}\right] \tag{3.12a}$$

$$= n_R + i\tilde{\kappa}, \tag{3.12b}$$

where $\delta = 2\Delta/\Gamma$ is the detuning in half linewidths and k is the wavevector of the incident light. Here we have assumed the limit of a a weak probe intensity. To correct for saturation effects δ^2 has to be replaced by $\delta^2 + I/I_{sat}$ in the denominator [72]. For non-zero detunings the real component of the index of refraction is unequal to 1 and therefore causes the cloud to refract. The imaginary part $\tilde{\kappa}$ reduces the intensity of the light and is therefore also referred to as the extinction coefficient. We note that this definition of the extinction coefficient is slightly different that the one given in Equation 3.1, where it was defined with respect to the reduced intensity. After traveling through an atom cloud of thickness z, the electric field of the incident light is given by

$$E' = e^{ikn_{ref}z}E_0 = e^{-k\tilde{\kappa}z}e^{ikn_R z}E_0 = tE^{i\phi'}, \tag{3.13}$$

where t is the transmission and ϕ' is the overall phase shift. The phase shift due to the atoms is $\phi = k n_R z - k n_{vacuum} z = k(n_R - 1)z$ and is given by

$$\phi = -\frac{\tilde{n}\sigma_0}{2}\frac{\delta}{1+\delta^2}.$$ (3.14)

The refraction angle for a cloud of atoms with a diameter d and a maximum phase shift ϕ can be estimated as $2\phi\lambda/\pi d$. If the phase shift is less than $\pi/2$, the refraction angle is smaller than the diffraction angle λ/d due to the finite size of the object. If the refraction angle is larger than the diffraction angle, the spatial resolution of a diffraction limited imaging system will be degraded [72]. The refraction angle is maximum for a detuning of $\Delta = \pm\Gamma/2$ and is given by $\phi = -\frac{\tilde{n}\sigma_0}{4}$. Therefore for optical depths $OD = \tilde{n}\sigma_0 > 2\pi$, diffraction effects become significant and reduce the imaging resolution. This can cause errors when trying to determine the total number of atoms (see Section 3.2.5). Additionally, the diffracted rays that are not collected by the imaging system will appear as false absorption signals. The magnitude of this effect depends on the density and therefore will vary across the cloud. As the refraction is not uniform across the cloud, it will not only affect the absolute measurement of the density but also relative measurements. In summary, dispersively dense atomic clouds will reduce the imaging resolution and can make it difficult to reliably determine the atom number. Ideally, the atoms are therefore probed with on-resonance light.

3.2.4 Heating of the Cloud

The heating of the atom cloud due to the recoil induced motion can blur the image signal and reduce the absorption signal by Doppler-shifting the atoms out of resonance. During imaging, the atoms will absorb photons out of the probe beam at the scattering rate γ_p. After absorbing a photon out of the probe beam, an atom will acquire a velocity $v_{rec} = \hbar k/m$ along the direction of the probe beam, where $\vec{k}$ is the wavevector of the incident light and m is the mass of the atom. For the D_2-line of ^{87}Rb v_{rec} is equal 5.9 mm/s. After a probe time Δt, the atoms will have absorbed

35

$N_p(\Delta t) = \gamma_p \Delta t$ photons and the velocity of the atom in the direction of the probe beam will have increased by $\Delta v = v_{rec}\gamma_p\Delta t$. Neglecting the Doppler-shift of the atoms due to the increase in the atom's velocity, the velocity and the displacement along the direction of the probe due to absorption can be written as $v_z = v_{rec}\gamma_p\tau$ and $z = \frac{1}{2}v_{rec}\gamma_p\tau^2$. For every photon that is absorbed, the atom scatters a photon. After each scattering event the atom will recoil opposite the direction of emission. Assuming that the photons are scattered uniformly in all directions, the gain in velocity can be modeled by a three-dimensional random walk in momentum space with a step length of v_{rec} and step number $N_p(\Delta t) = \gamma_p\Delta t$. The root mean squared velocity after a probe time Δt is therefore equal to $\Delta v_{rms} = v_{rec}\sqrt{\gamma_p\Delta t}$. Integrating the root mean squared velocity along a given direction $\Delta v_x^{rms} = (v_{rec}/\sqrt{3})\sqrt{\gamma_p\Delta t}$, we obtain the resulting blurring $x = \frac{2}{3\sqrt{3}}v_{rec}\sqrt{\gamma_p}\tau^{3/2}$ of the atom cloud.

If we assume the incident probe intensity $I_0 = I_{sat}^0$ then $\gamma_p = \frac{\Gamma}{4}$, where Γ is the linewidth of the transition. For a probe time $\tau = 100$ μs ($\tau = 10$ μs), the atom cloud will have a velocity $v_z = 5.6$ m/s ($v_z = 0.56$ m/s) in direction of the probe and will have been pushed along this direction by $z = 230$ μm ($z = 2.3$ μm). For long probe times the cloud will therefor be pushed out of the depth of focus. Additionally, the cloud will have a root mean velocity $v_{x,rms} = 0.105$ m/s ($v_{x,rms} = 0.033$ m/s) and will be blurred by $x = 7.0$ μm ($x = 0.22$ μm). This estimation of the blurring of the cloud is an overestimation because we did not take into account the velocity distribution of the cloud but simply considered the root mean squared velocity and did not correct the scatter rate for the increasing Doppler-shift. It is also important to note that for a trapped cloud the blurring is expected to be much less as the atoms are spatially confined by the trap.

Besides blurring, the atom motion Doppler-shifts the atoms our of resonance $\Delta = -\vec{k}\cdot\vec{v}$ and therefore causes dispersion (see Subsection 3.2.3) and reduces the absorption signal (see Subsection 3.2.2). For a velocity $v_z = 5.6$ m/s ($v_z = 0.56$ m/s) along the

probe direction, the Doppler shift in units of the half linewidths is $2\Delta/\Gamma = 2.4\ (0.24)$. As a result, the absorption cross-section is reduced to 15% (95%) of the on-resonant cross-sections (see Equation 3.11).

In summary, the efficiency of absorption imaging is limited by the heating of the cloud. This limitation puts an upper bound on the probe time τ and we there generally do not use probe times longer that 100 μs. The probe power affects the velocity through the scatter rate γ_p, which saturates at $\frac{\Gamma}{2}$ for $I_0 \longrightarrow \infty$. The heating of the atom cloud is therefore less dependent on the probe power compared to the probe time.

3.2.5 Imaging Resolution

A fundamental limit in absorption imaging is the imaging resolution. Not only does the imaging resolution limit the quality of the image, but it also limits the ability to reliably count the total number of atoms. The number of atoms N_i (in a region of uniform density) does not linearly depend on the relative transmission of the probe beam intensity $T_i = I'/I_0$ but is given by

$$N_i = -\frac{A}{\sigma_0}\left[od_i + \frac{I' - I_0}{I_0^{sat}}\right] = \frac{A}{\sigma_0}\left[-\ln T_i + \frac{I_0}{I_{sat}^0}(1 - T_i)\right], \qquad (3.15)$$

where we have simply rewritten the optical depth (see Equation 3.7) in Equation 3.10 in terms of the relative transmission of the probe beam intensity. The total number of atoms $N = \sum_i N_i$ (in a cloud with a non-uniform density) cannot simply be determined by measuring the total relative transmission of the probe beam, because $\sum_i \ln T_i \neq \ln \sum_i T_i$, the superposition principle does not hold and the total number of atoms $N = \sum_i N_i$ (in a cloud with a non-uniform density) cannot simply be determined by measuring the total relative transmission of the probe beam. As mentioned in Section 3.1, the derivation of the optical depth can be extended to non-uniform clouds by considering the light as a collection of rays that each interact with a small uniform section of the cloud. However, it is necessary to keep track of each

of these individual rays and measure the atom number for each uniform section.

The imaging resolution determines how well one can distinguish between the different rays. The image of an object that is smaller than the imaging resolution will be smeared out approximately to the resolution limit. Consider N atoms with a uniform density that are imaged on an area A_1 with a uniform probe intensity I_0. The optical density will be given by $od = -ln(I'/I_0)$. If this cloud of atoms is smaller than the resolution limit, its image (or more precisely its shadow) will be smeared out over a larger area A_2. Let us assume that this area is twice as large as the original area A_1 and that the smearing of the image effectively acts like binning. In this case, the measured optical density od_{meas} will be

$$od_{meas} = -\ln \frac{I' + I_0}{2I_0} = od - \ln\left(\frac{1 + e^{od}}{2}\right). \tag{3.16}$$

So the atom number will be underestimated, and this underestimation is larger for clouds with a larger optical density. For a reliable quantitative analysis, it is therefore necessary that the column density of the atom cloud is uniform on the length scale of the imaging resolution and the pixel size.

3.2.6 Maximum Observable Optical Density

A common limitation of any absorption imaging system is the maximum observable optical density. Any light collected by the camera that cannot be absorbed by the atoms will reduce the observed optical density and cause a systematic error. The two most common sources are off-resonant light in the probe beam and probe-light that does not pass through the atomic cloud, yet scatters onto the camera and fills in the shadow of atoms. Any off-resonant scatter not part of the probe can be subtracted out by taking a background with the probe beam off.

The frequency spectrum of diodes and tampered amplifiers often have a broad pedestal of light (≈ 10 nm wide) that is not in the main frequency mode of the laser. Since our probe beam is from a diode laser, we expect off-resonant light to reduce our

maximum observable optical density. Additionally, the maximum observable optical density can be limited by probe light scattered off of objects other than the atoms: such as any dirt, dust, or any other imperfections of the optical elements in the imaging system. Since this light is scattered mainly in the forward direction, it is collected by the camera and can therefore fill in the shadow cast by the atoms and make the optical density appear smaller than it actually is. This effect is increased for spatially smaller atomic clouds, since a smaller forward scattering angle is necessary for light scattered near the edge of the clouds shadow to fill the center. Similarly, probe light reflected off of objects can indirectly scatter onto the camera and cause a reduction of the observable optical density. Especially, optical elements with a poor anti-reflection coating can cause the probe light to reflect off of multiple surfaces and into the camera. In general, a smaller probe beam and smaller magnification will reduce the unwanted scattering into the camera. It is difficult to make a precise measurement of the off-resonant light scattered into the imaging system because it depends on the individual imaging system, can vary across the image, and can vary with the size of the cloud. The best estimate can be made by imaging a large and dense object and measuring the maximum observable optical density. An example, of such a measurement is shown in Figure 3.4, where we image a wire and determine the maximum observable density to be ≈ 3.5. In this case, the maximum density is limited by scattered light. For an atom cloud the maximum observable density is potentially higher because off-resonant light in the probe beam will further reduce the maximum observable density.

The limit on the maximum observable optical density leads to an underestimation of the number of atoms in the cloud. By modeling the maximum observable optical density as light that is present in the probe light but cannot be absorbed by the atoms independent from the source, one can take this effect into account and can correct the measured atom number. The total intensity of the probe light I_0 can be written

as the sum of two terms: light that can be absorbed by the atoms I_{res} (referred to as resonant light in this section) and light that cannot be absorbed by the atoms I_{offres} (referred to as off-resonant light in this section): $I_0 = I_{res} + I_{offres}$. When the probe light passes through the atoms, only the resonant part of the beam will absorb light and the total probe intensity will be reduced to

$$I' = I_{res}e^{-od} + I_{offres}. \tag{3.17}$$

As a result the optical density measured od_{meas} is given by

$$od_{meas} = -\ln\left(\frac{I_{res}e^{-od} + I_{offres}}{I_{res} + I_{offres}}\right). \tag{3.18}$$

The maximum optical density od_{max} is observed when all of the resonant is absorbed and can be written as

$$od_{max} = -\ln\left(\frac{I_{offres}}{I_{res} + I_{offres}}\right). \tag{3.19}$$

Solving the above equation for the actual optical density od of the atoms and substituting in the maximum observable optical density od_{max} one gets the corrected optical density od_{corr}

$$od_{corr} = -\ln\left(\frac{e^{-od_{meas}} - e^{-od_{max}}}{1 - e^{-od_{max}}}\right) \tag{3.20}$$

and the actual optical depth OD_{corr} is given by

$$OD_{corr} = od_{corr} + (1 - e^{-od_{corr}})\frac{I_0}{I_0^{sat}}. \tag{3.21}$$

The maximum observable od_{max} can be measured by imaging a large and optically dense cloud. The center of the large cloud will have a flat top where the od is saturated at the maximum value. Depending on the imaging system, typical values for od_{max} range from 2.0 - 3.5. If 1% of the probe beam is off-resonant light, the maximum measurable optical density is given by $od_{max} = -ln(0.01) = 4.6$. For example, a condensate with an optical depth $OD = 2.86$, that is probed with an

intensity $I_0 \approx I_{sat}^0$ has an actual optical density $od = 2$. If the maximum observable density is $od_{max} = 3$, the raw measurement will given an optical density $od_{meas} = 1.72$ and an optical depth $OD = 2.54$, which underestimates the number of atoms by 10% if image is not corrected for the maximum observable density.

For optically dense clouds ($od \geq od_{max}/2$), od_{meas} approaches od_{max} and the correction factor between od_{meas} and od_{corr} becomes large increasing the potential for error. Effects such as the spatial structure of the scattered light and its dependence on the size and position of the atomic cloud become important. In order to ensure a proper measurement of the atomic number, the expansion of the cloud should be increased until $od \leq od_{max}/2$.

3.2.7 Multilevel Structure

In the above derivation of the optical depth, we have assumed a two-level atom. However, in reality, there are five Zeeman levels in the $F = 2$ ground state and seven Zeeman levels in the $F' = 3$ excited state of a ^{87}Rb atom. So, depending on the polarization of the light there are many allowed electric dipole transitions, whose strengths vary. The relative strengths of the different transitions are determined by the hyperfine dipole matrix elements. By probing the atoms with circularly polarized light that propagates along the atoms' quantization axis, we exclusively drive the $\Delta m_F = +1$ ($\Delta m_F = -1$) transition, also referred to as the σ^+ (σ^-) transition. As a result, the atoms cycle on the $F = 2$, $m_F = +2 \longleftrightarrow F' = 3$, $m_F = +3$ ($F = 2$, $m_F = -2 \longleftrightarrow F' = 3$, $m_F = -3$) transition and the system is effectively reduced to a two-level system. Additionally, this cycling transition has the advantage of having the maximum absorption cross-section.

In practice, however, it is very difficult to perfectly control the polarization of the probe beam. The quality of the polarization is limited by the quality of the optics, such as polarizing beam cubes, waveplates, and the viewports of the chamber. The
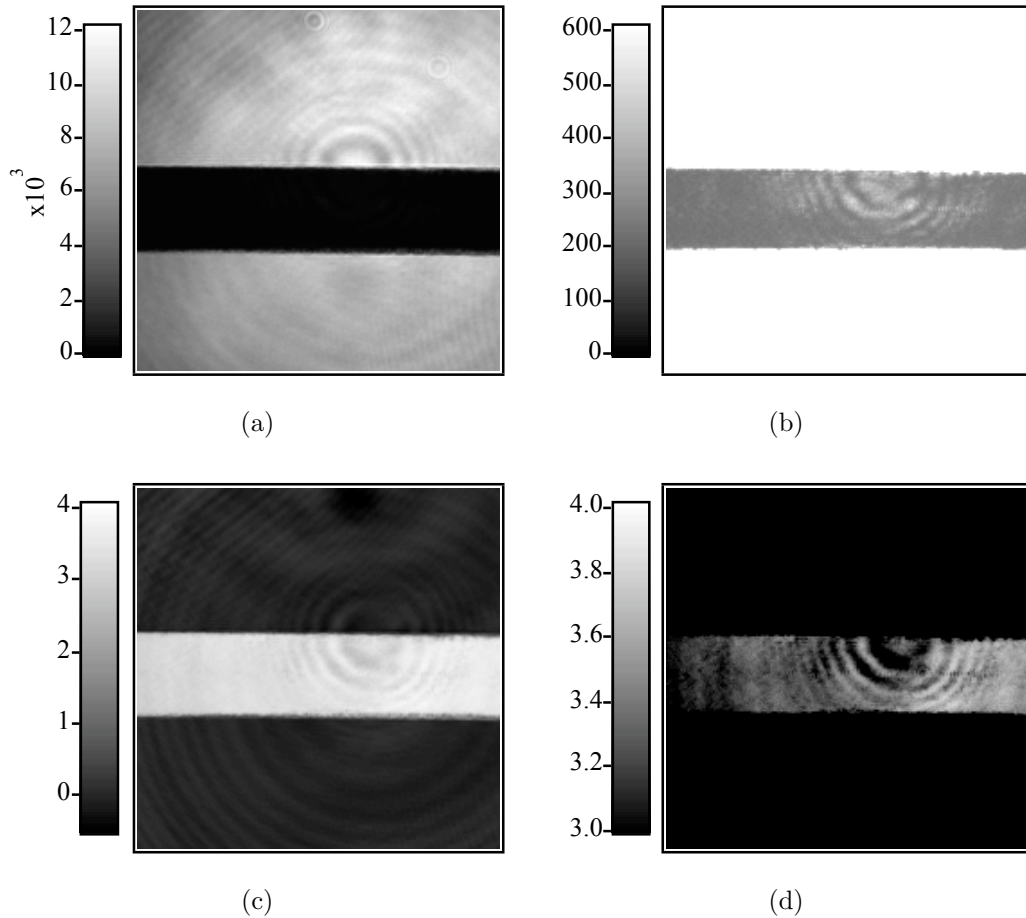
Figure 3.4: In a bench test, we image a wire in order to illustrate the effects of light scatter and probe beam intensity variations on an absorptive image. (a) and (b) show the probe beam intensity profile after passing through a wire. (b) was rescaled to show that light is filling in the shadow of the wire. In a perfect imaging system, the shadow of the wire should be totally blackened out, because it is an opaque object. We determined the optical density ((c) and (d)) after taking a reference image (not shown here). The maximum optical density of the wire is 3-4, which corresponds to the maximum observable optical density of this imaging set-up. The patterns in the background of the image (c) are caused by variations in the probe beam intensity profile. (c). The patterns also manifest themselves on the image of the wire (c).

polarization of the probe beam is therefore not guaranteed to be purely circularly polarized. Moreover, the propagation direction of the probe beam is not necessarily aligned with the magnetic field, which defines the quantization axis. In either of these two cases, there is a probability to also drive the $\Delta m_F = 0$ and the $\Delta m_F = -1$ ($\Delta m_F = +1$) transitions, which leads to a smaller overall absorption cross-section.

For the transition of the atoms between the levels we have assumed the steady state. In reality, however, it takes a finite amount of time to reach the steady state, and this time is of the order of lifetime of the excited state $1/\Gamma = 26$ ns. As long as as the probe time is at least 10 times longer than the lifetime, we can safely assume the steady state.

The absorption signal will also depend on the initial distribution of the populations in the Zeeman levels. Before reaching the cycling transition the atoms need to be optically pumped to the stretched state $m_F = +2$ ($m_F = -2$). Ideally, the time to spin-polarize the atoms is much less than the total probe time as otherwise the absorption signal is reduced and dependent on the initial Zeeman state of the atom. When we image atoms in the $F = 1$ state, we pulse on a repump beam in order to transfer the atoms to the $F' = 2$ state, from which they decay to the $F = 2$ state. As a result, the atoms will be randomly distributed among the Zeeman levels of the $F = 2$ state as they are being imaged. For more details on optical pumping see [60]. To ensure the steady state and reduce the fraction of time it takes the atoms to be pumped to the stretched state, we use probe times equal to or larger than 10 μs.

The imperfections described above all reduce the absorption cross-section. Rather than separately quantifying of all the mechanisms reducing the absorption cross-section (including the heating of the atoms cloud described in Section 3.2.4), we can experimentally determine the effective absorption cross-section through a calibration of our absorption imaging system. The details of this calibration method are explained in more detail in Section 3.3.

3.2.8 Photon Shot Noise

In the previous subsection, we described the mechanisms limiting the absorption signal. In the next two subsections, we will address the noise present in absorption imaging. The fundamental limit in detecting atoms using absorption imaging is given by the photon shot noise of the probe beam, or more precisely by the shot noise of the electrons that are counted by the camera as a result of the incident photons. The photon shot noise on a pixel is $\sigma^2_{\text{PSN}} = N_e = qN_p$, where q is the quantum efficiency of the camera and N_p is the number of photons incident on the pixel, and $N_e = qN_p$ is the number of photons converted to electrons. In terms of the probe intensity I the photon number is given by $N_p = (I\tau A_{pix}/\hbar\omega_0)$, where τ is the probe time, A_{pix} is the effective area of a pixel, and $\hbar\omega_0$ is the energy of a single photon. The noise on a pixel in units of the atom numbers (N_a) is given by

$$\sigma^2\left(N_a\right) = \left(\frac{\partial N_a}{\partial N_e^0}\right)^2 \sigma^2_{\text{PSN\_of\_}N_e^0} + \left(\frac{\partial N_a}{\partial N_e'}\right)^2 \sigma^2_{\text{PSN\_of\_}N_e'}, \tag{3.22}$$

where N_e^0 and N_e' are the number of electrons counted for the pixel of the reference and signal image, respectively. Taking derivatives and using the equation 3.5, the noise can be written in terms of the probe intensity of the reference I' and signal I_0

$$\sigma^2\left(N_a\right) = \frac{A_{pix}}{\sigma_0 \frac{\Gamma}{2} q\tau}\left[4 + \left(1 + \frac{I_0}{I'}\right)\frac{I_{sat}^0}{I_0} + \left(1 + \frac{I'}{I_0}\right)\left(\frac{I_0}{I_{sat}^0}\right)\right]. \tag{3.23}$$

Using this equation the photon shot noise on a pixel can be determined. Preferably, the atom noise is written in terms of the total number of atoms N_a imaged on the pixel and the incident probe beam I_0. However, the equation for the number of atoms (on a pixel)

$$N_a = -\frac{A_{pix}}{\sigma_0}\left(\ln\frac{I'}{I_0} + \frac{(I' - I_0)}{I_{sat}^0}\right) \tag{3.24}$$

cannot be analytically solved for the transmitted intensity I'. Therefore the noise has to be determined numerically for a given experimental setting. The behavior of the
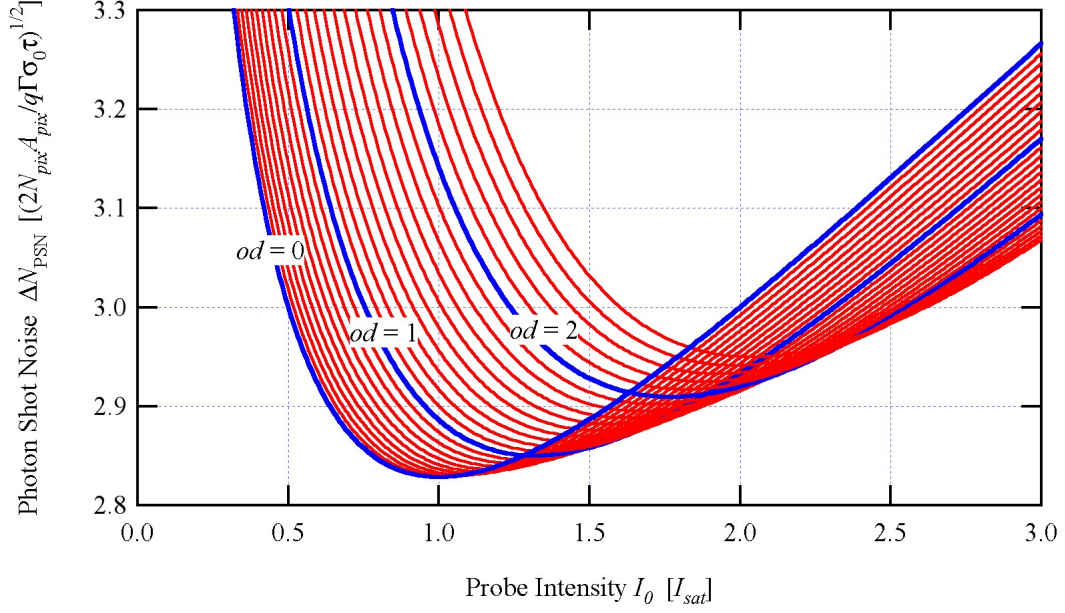
Figure 3.5: Graph of photon shot noise in absorption imaging as a function for the probe intensity.

noise is illustrated in Figure 3.5, and the noise curve is plotted in units of

$$\sqrt{\frac{N_{pix}A_{pix}}{\sigma_0 \frac{\Gamma}{2} q \tau}}, \tag{3.25}$$

where N_{pix} is the total number of pixels in the region of interest. The pixels are assumed to be independent and therefore the noise adds in quadrature. The photon shot noise depends on the size of the region of interest $N_{pix}A_{pix}$, which is determined by the size of the condensate. For lower photon shot noise, it is therefore preferable to work with the shorter time of flights. For $\tau = 10$ μs ($\tau = 100$ μs), $q = 0.9$, $N_{pix}A_{pix} = 90$ μm^2, $I_0 = I_{sat}^0$, and $OD = 1$, the noise on a pixel is 38 atoms (12 atoms). The photon shot noise depends most strongly on the probe time and the size of the condensate. It is important to note that the probe time cannot be arbitrarily increased as this leads to heating of the condensate (see section 3.2.4). Similarly, the atom numbers in a cloud cannot be reliably counted for arbitrary dense clouds (see Sections 3.2.1, 3.2.5, and 3.2.6).

For a small number of photons incident on a pixel, the shot noise of the probe

beam σ_{PSN} can be comparable to the readout noise of the camera ($\sigma_{cam} \sim 10$ electrons per pixel). For example, for a camera with $q = 0.9$ ($q = 0.32$) if 110 (310) photons are incident on a pixel, the resulting shot noise is 10 electrons per pixel. In this case, the camera noise cannot be neglected but has to be taken into account. So the total noise on a pixel in equation 3.18 should read $\sigma^2_{Total} = \sigma^2_{PSN} + \sigma^2_{cam}$ instead of simply σ^2_{PSN}. In our example, this would be $\sigma^2_{PSN} = 200$ electrons.

3.2.9 Technical Limitations

In order to have shot noise limited absorption imaging, it is crucial to suppress the shot-to-shot variations in the probe beam intensity profile. Potential errors due to long term experimental drifts are eliminated by taking the reference and the signal image in rapid succession. The time between reference and signal generally is limited by the pixel readout of the camera. The first image has to be read by the camera before the second one can be taken. In this case, the time between images is around $200-300$ ms. The limitation due to the readout rate can be circumvented by masking part of the chip, quickly shifting the first image to the masked region, and storing it there while the second image is taken. After taking both images the camera can then slowly readout both images. The minimum time between images is now determined by the vertical shift speed of the camera and can be reduced to a few ms.

Any patterns on the probe beam, such as interference patterns or scatter from imperfections in the imaging system, can manifest if there are high frequency vibrations in the imaging set-up. It is therefore important to use high-quality optics in the imaging system and to avoid using any devices that can cause vibrations, such as shutters during (and slightly before) imaging.

3.3 Calibration

To account for the mechanisms that reduce the effective absorption cross-section (such as heating of the atom cloud Subsection 3.2.4, off-resonant light Subsection

3.2.6, and the multilevel structure of the hyperfine levels see Subsection 3.2.7), we introduce the dimensionless parameter α and define the effective saturation cross-section $\sigma_{eff} = \sigma_0/\alpha$ [70]. As a result, the effective saturation intensity is given by $I_{sat}^{eff} = \alpha I_{sat}^0$ (see equation 3.5). Inserting the effective cross-section and saturation intensity into Equation 3.7, the total number of atoms in the cloud N can be recast in the form

$$N = A_{pix} \sum_{pix} \tilde{n}(x,y) = -A_{pix} \sum_{pix} \left[\frac{\alpha}{\sigma_0} ln \frac{I'(x,y)}{I_0(x,y)} + \frac{I'(x,y) - I_0(x,y)}{\sigma_0 I_{sat}^0} \right]. \qquad (3.26)$$

The number of atoms N in the cloud is an intrinsic property of the cloud and does not depend on the probe intensity. We therefore can determine the value of α by measuring N versus various different probe intensities. For each image, we calculate the number of atoms $N(\alpha)$ for different values of α ranging from 1 to 4.0. The value of α for which the atom number N remains constant over the whole range of probe beam intensities is the correct calibration parameter. In practice, the calibration parameter α is the one that has the minimum standard deviation of the atom numbers over the range of incident intensities used to image the cloud.

Examples of such a calibration are shown in Figure 3.6. In this experiment, we measured the calibration parameter for different orientations of the magnetic field. In the first case, the magnetic field is aligned with the probe beam and in the second case it is perpendicular to the probe beam. We find $\alpha = 2.2 \pm 0.1$ and $\alpha = 2.7 \pm 0.1$, respectively. This result clearly illustrates the sensitivity of absorptive imaging on the orientation of the magnetic field. The absorption cross-section is reduced by a factor of 1.22 for a magnetic field perpendicular to the probe beam compared to the case where it is parallel to the probe. In both cases, the absorption cross-section is reduced compared to the ideal value. This is in part due to the sidebands of the probe caused by the modulation of the laser current. The sidebands are detuned 6 MHz (= the frequency of the modulation) from resonance and constitute approximately 28% of the total probe power. The resonant cross-section for this detuning is reduced by
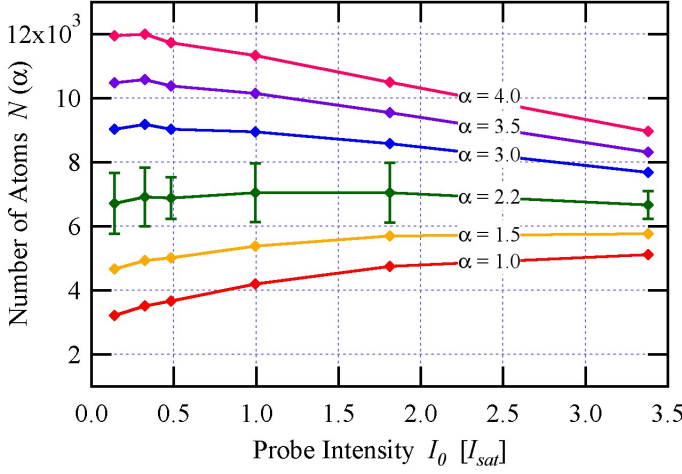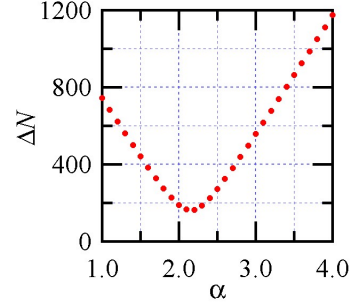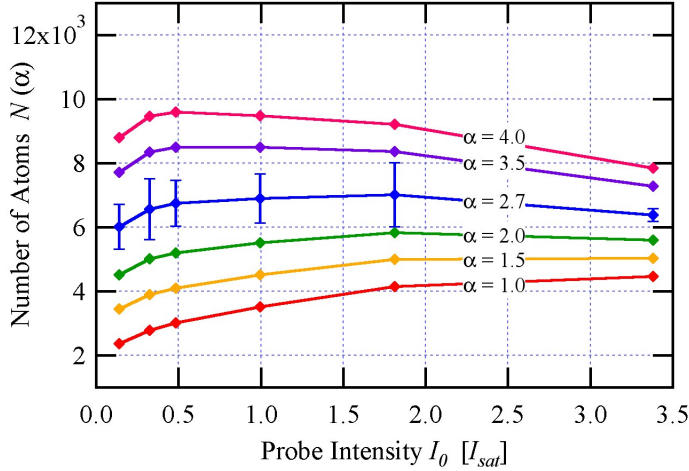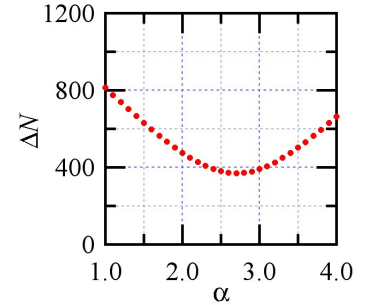
Figure 3.6: Calibration of the absorption imaging set-up. The BEC is imaged with a range of different probe intensities. For each image, the total number of atoms N is determined for several values of α. The calibration was done for both a magnetic field parallel ((a), (b)) and perpendicular ((c), (d)) to the probe beam. The error bars shown in the graph are the experimental standard deviation, and each data point is an average of 22 experimental runs. The actual calibration constant is found by finding the value for α that gives the minimum standard deviation of the data sets $\Delta N(\alpha)$ (see (b) and (d)). The absorption calibration constant was determined to be $\alpha = 2.2 \pm 0.1$ and $\alpha = 2.7 \pm 0.1$, respectively.

$\approx 30\%$ (see Equation 3.11). The overall absorption cross-section is reduced by 20%. In our calibration, we have determined that the absorption cross-section is reduced by $\approx 50\%$ compared to the ideal value. Therefore we assume that are also other factors contributing to the reduction in the absorption cross-section. For example, the heating of the atom cloud.

CHAPTER IV

FLUORESCENCE IMAGING

Fluorescence imaging relies on detecting the photons the atoms re-emit as they are being probed. In our experiment, we use all of the MOT beams to illuminate the atoms. The scattered light, or a fraction thereof, is then collected and focused on a charged coupled device (CCD) camera to form an image (see Figure 4.1). The quality of the image is, in part, determined by the fraction of the scattered light that is collected by the imaging system; the larger the fluorescence signal, the larger the signal to noise ratio. Ideally, we only collect light emitted by the atoms because light from other sources, such as the probe beams (in our case the MOT beams) or the room lights, adds noise to the fluorescence signal of the atoms.

4.1 Theory

The interaction of a two-level atom with radiation of angular frequency ω close to resonance can be described by the optical Bloch equations (OBE) (see [61]). For a closed two-level system (with ground state g and excited state e) including spontaneous emission, the OBE can be written in terms of the population difference $w = \rho_{gg} - \rho_{ee}$
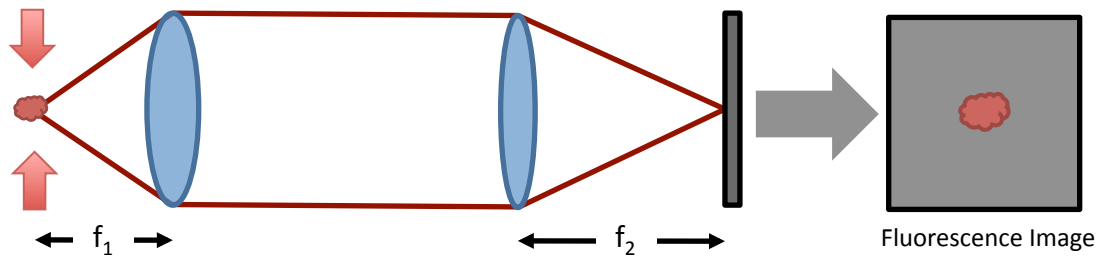
Figure 4.1: Schematic of the fluorescence imaging set-up.
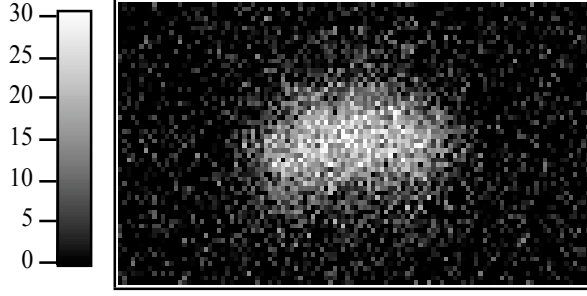
Figure 4.2: Example of a fluorescence image. This image shows the interference of two lattice sites of a BEC after a time of flight of 7 ms, where the total number of atoms is $N = 7800$. Because the atoms are probed from multiple directions with a large probe power $I_0 \approx 30 I_{sat}^0$, the atom cloud is distorted and the image is blurred. As a resutl, unlike for absorption imaging (see Figure 3.2(c)), the interference pattern can not be resolved. The probe time was 100 μs and the field of view is 176 x 96 μm^2. This images was taken with a camera with $q = 0.32$.

and the optical coherence $\rho_{eg} = \rho_{ge}^*$:

$$\frac{dw}{dt} = -\Gamma w - i \left(\Omega \rho_{eg}^* - \Omega^* \rho_{eg} \right) + \Gamma \tag{4.1a}$$

$$\frac{d\rho_{eg}}{dt} = -\left(\frac{\Gamma}{2} - i\Delta \right) \rho_{eg} + \frac{iw\Omega}{2}, \tag{4.1b}$$

where Γ is the decay rate of the excited state, Ω the on-resonance Rabi frequency, $\Delta = \omega - \omega_0$ is the detuning from resonance, and ρ_{ij} are the elements of the the density matrix

$$\rho = \begin{pmatrix} \rho_{ee} & \rho_{eg} \\ \rho_{ge} & \rho_{gg} \end{pmatrix}. \tag{4.2}$$

For the steady-state case $dw/dt = d\rho_{eg}/dt = 0$, and the resulting equations can be solved for the population ρ_{ee} of the excited state:

$$\rho_{ee} = \frac{(1 - w)}{2} = \frac{\Omega^2/4}{\Delta^2 + \Omega^2/2 + \Gamma^2/4}. \tag{4.3}$$

Defining the on-resonance saturation parameter

$$s_0 \equiv 2|\Omega|^2/\Gamma^2 = I/I_{sat}^0 \tag{4.4}$$

with the saturation intensity given by

$$I_{sat}^0 = \frac{\Gamma \hbar \omega_0^3}{12\pi c^2}, \tag{4.5}$$

the excited state population can be re-written as

$$\rho_{ee} = \frac{s_0/2}{1 + s_0 + (2\Delta/\Gamma)^2}. \tag{4.6}$$

In the steady state the excitation rate is equal to the decay rate of the excited state population due to spontaneous emission. Hence an atom interacting with radiation scatters photons with a scatter rate

$$\gamma_p = \Gamma\rho_{ee} = \frac{s_0\Gamma/2}{1 + s_0 + (2\Delta/\Gamma)^2}. \tag{4.7}$$

In fluorescence imaging we determine the number of atoms in a cloud by counting the number of photons with a CCD camera. More precisely, the scattered photons are converted to electrons on the sensor of the CCD camera. The efficiency of the conversion is referred to as the quantum efficiency q. The camera then counts the number of electrons N_e that are generated due to the incident photons. Since the photons are randomly scattered in all directions, only a small fraction of the photons ($\approx 1\%$) is collected by the imaging system. The maximum fraction of photons that can be collected is determined by the solid angle of the maximum cone of light collected by the imaging system. For an apex angle 2θ the imaging lens subtends the solid angle $4\pi \sin^2(\theta/2)$ and has the numerical aperture $\mathrm{NA} \equiv \sin(\theta)$ (for vacuum). For small angles θ the solid angle is approximately $4\pi(\theta/2)^2 \approx 4\pi\mathrm{NA}^2/4$ and the fraction of photons collected by the imaging lens is approximately $\mathrm{NA}^2/4$. Consequently, the total number of atoms N_a is given by

$$N_a = \frac{4N_e}{q\mathrm{NA}^2} \frac{1}{\gamma_p\tau}. \tag{4.8}$$

As mentioned earlier, in the steady state the number of photons absorbed is equal to the number of scattered. Therefore the same photons that are counted as missing in absorption imaging are scattered in fluorescence imaging. However, in fluorescence imaging only a small fraction of the photons are collected and so the signal strength in fluorescence imaging is much weaker for the same probe power.

4.2 Limitations

In this chapter, we discuss the limitations of fluorescence imaging. Some of the limitations are very similar to those given in absorption imaging, such as corrections due to the atomic motion, optically dense clouds, or the multi-level structure of the transition. For the sake of completeness these limitations will be mentioned and discussed briefly in this chapter, and the differences will be pointed out in more detail.

4.2.1 Optically Dense Clouds

In the above derivation, we have neglected the fact that the probe beams lose intensity as they travel through the cloud. For high probe intensities and sufficiently optically dilute clouds, however, the reduction in probe intensity as the beam passes through the cloud does not lead to a noticeable reduction in the scatter rate. Consider the scatter rate for on-resonant light

$$\gamma_p = \frac{s_0}{1 + s_0} \frac{\Gamma}{2},\tag{4.9}$$

which saturates to $\Gamma/2$ for very high intensities $I_0 >> I_{sat}^0$. For example, a probe beam with intensity of 30 I_{sat}^0 that travels through an atom cloud with an optical depth $OD = 23$ is reduced by $\approx 75\%$ to the value 7.7 I_{sat}^0. The resulting reduction in the scatter rate, however, is only $\approx 10\%$. In this example, we have use a very dense atom cloud. A more reasonable value for the optical depth is $OD = 5$. In this case, the probe intensity is reduced by 16% to 25 I_{sat}^0 and the resulting reduction in probe intensity is less than 2%. For high probe intensities (and reasonably dilute atom clouds) we can therefore safely assume that the intensity of the probe beams remain constant as they travel through the cloud. This example also illustrates that fluorescence imaging with high probe intensities is relatively insensitive to intensity fluctuations.

It is important that the cloud is sufficiently optically dilute not only to ensure that the intensity does not decease significantly as the probe beams travel through the cloud but also to prevent the re-scattering of photons. In an optically dense cloud, the photon scattered by an atom can be reabsorbed by another atom in the cloud. As a result, the scattered photon never leaves the cloud and is not accounted for. In this case the number of atoms will be underestimated.

4.2.2 Atom Motion

As in the case of absorption imaging, in the above derivation the motion of the atoms has been neglected, which in general is a safe assumption for a condensate. The heating of the atom cloud during imaging can Doppler-shift the atoms out of resonance and therefore reduces the scatter rate (see Equation 4.7), although for high probe intensities this effect is negligible as the linewidth is significantly power broadened. For example, if we probe the atoms with a probe intensity 30 I_{sat}^0 for 100 μs, the atoms will acquire a root mean squared velocity $v = 0.15$ m/s (see Subsection 4.2.3) along a given direction. For a probe beam along that direction the detuning as a result of the atom motion in units of line halfwidths is $2\Delta/\Gamma = 0.06$, which for a probe intensity 30 I_{sat}^0 reduces the scatter rate by $\ll 1\%$.

4.2.3 Heating of the Cloud

Every time an atom absorbs or emits a photon it will experience a recoil, which increases its kinetic energy. In fluorescence imaging we probe the cloud with pairs of counterpropagating beams, namely the MOT beams. This prevents the cloud from being pushed along a single direction as is the case in absorption imaging. However, in order to eliminate any residual push or distortions of the cloud, the probe beams need to be carefully balanced, which is technically challenging. As a result, fluorescence imaging is not well suited for determining the shape of small clouds or for resolving small structures. Independent of the probe beam alignment

and the distributions of probe beam intensities, the cloud will heat up as it scatters photons. After a probe time τ the atom will have acquired a root mean squared velocity along a given direction $v_x^{rms} = \left(v_{rec}/\sqrt{3}\right)\sqrt{\gamma_p \tau}$ and the image will be blurred by $x = \frac{2}{3\sqrt{3}} v_{rec} \sqrt{\gamma_p} \tau^{3/2}$. (For more details see Section 3.2.4) For our experimental parameters, $I_0 \approx 30 I_{sat}^0$ and $\tau = 100$ μs, $v_x^{rms} = 0.15$ m/s and $x = 9.9$ μm.

If long probe times ($\gtrsim$ ms)are necessary, for example in order to image single atoms in a trap, the probe beams can be detuned to the red of the cycling transition. The probe beams then create an optical molasses as in the case of a MOT. The atoms will therefore not continue to heat up with increasing probe times but will be cooled to a few tens of μK. This method can be used for continuous observation of small atoms numbers in a sufficiently deep trap (for example see [69]). If the trap is shallower than the temperature of the optical molasses the atoms will eventually boil out of the trap and are lost.

4.2.4   Imaging Resolution

The spatial resolution of a fluorescence image is in most cases limited by the distortion and the blurring of the cloud due to the probe beams. Fluorescence imaging is therefore mainly used to count atoms and not to resolve structures within the cloud. Because the signal, namely the number of photons scattered, depends linearly on the number of atoms, the spatial resolution does not affect the ability to reliably count the number of atoms. As a result, binning the pixels on the camera chip does not introduce errors in determining of the atom number. However, an imaging set-up with a higher numerical aperture is still desirable because it collects a larger fraction of the scattered photons and therefore increases the signal to noise ratio (see Section 4.2.6).

4.2.5 Multilevel Structure

As in the case of absorption imaging, we have assumed an ideal two-level system in the derivation of the scattering cross-section, whereas in reality there are five Zeeman levels in the $F = 2$ ground state and seven Zeeman levels in the $F' = 3$ excited state. As a result, the scatterrate will depend on the polarization of the probe beams and can also depend on the initial distribution of the populations in the Zeeman levels. For fluorescence imaging we use the MOT beams which consist of three orthogonal pairs of σ^+ - σ^- probe beams, each of intensity I_0. For this complex system it is difficult to determine the actual saturation intensity as the probe beams can interfere and create lattice-like intensity maxima and minima. However, if one assumes that the atoms are on average illuminated with a total probe intensity $6I_0$, the polarization of the light can be considered to be isotropic, i.e. it has equal components in all three possible polarizations. In this case, the saturation intensity is independent of the population distribution among the Zeeman levels and the system can be considered to effectively be a two-level system. For the $F = 2 \longleftrightarrow F' = 3$ cycling transition $I_{sat}^0 = 3.576$ mW/cm^2 [60].

Since we probe with high intensities ($\approx 6 \times 20$ mW/cm^2), the scatter rate is nearly its maximum ($\Gamma/2$) and this minimizes errors in the estimation of the saturation intensity.

4.2.6 Photon Shot Noise

The fundamental limit in counting the atom numbers in fluorescence imaging is given by the photon shot noise of the scattered photons detected by the camera. For N_p photons collected by the imaging system the photon shot noise is equal to $\sigma_{\text{PSN}}^2 = qN_p = N_e$, where q is the quantum efficiency and N_e the number of electrons counted by the camera as a result of the incident photons. Given an imaging system with a numerical aperture NA and given a scatter rate γ_p, and a probe time τ the photon

shot noise in terms of the number of atoms N_a is

$$\sigma_{\text{PSN}}^2(N_a) = \frac{4}{q\text{NA}^2\gamma_p\tau}N_a. \tag{4.10}$$

For $\tau = 100$ μs, $\gamma_p = \Gamma/2 = 19.5$ μs^{-1}, $q = 0.9$, and NA $= 0.22$, $\sigma_{\text{PSN}}(N_a) = 0.22\sqrt{N_a}$ and the signal to noise ratio is SNR $= 4.6\sqrt{N_a}$. The SNR is equal to one for 0.047 atoms indicating that it is possible to detect single atoms if the noise is indeed limited by photon shot noise.

4.2.7 Technical Limitations

In reality, fluorescence imaging is often limited by the technical noise of the camera or the photon shot noise of unwanted background scatter. The camera noise is dominated by the readout noise which is added to the signal in the process of reading out the signal on a pixel. The readout noise is given in terms of electrons per pixel. For the CCD cameras that we have used the readout noise is of the order of 10 electrons $(\sigma_{\text{RO}}^2 = 100$ (e$^-$)$^2)$. In units of atom numbers, the readout noise per pixel is

$$\sigma_{\text{RO}}^2(N_a) = \left(\frac{4}{q\text{NA}^2\gamma_p\tau}\right)^2 \sigma_{\text{RO}}^2. \tag{4.11}$$

Using the same parameters as above, the readout noise is $\sigma_{\text{RO}}(N_a) = 0.22$ atoms per pixel independent of the number of atoms imaged. The total readout noise on an area with N_{pix} number of pixels is $\sigma_{\text{RO}}(N_a) = 0.22\sqrt{N_{pix}}$ atoms assuming that the noise on the individual pixels is uncorrelated. In order to minimized the readout noise, one can bin the pixels, $i.e.$ form super-pixels by combing the electrons of multiple (adjacent) pixels into a larger bin, a super-pixel. For example, if 4 pixels are binned into a super-pixel, the camera will only readout one signal for these 4 pixels instead of 4 individual signals. As a result, the readout noise will be reduced by a factor of $\sqrt{4} = 2$ at the expense of the spatial information provided by the separate 4 pixels.

The noise due to unwanted background scatter is determined empirically by acquiring images without atoms. Assuming that $N_e^{bkg} = \gamma_e^{bkg}\tau$ electrons are counted

due to the background scatter after a the probe time τ, the resulting photon shot noise in units of atom number is

$$\sigma^2_{bkgscatt}(N_a) = \left(\frac{4}{q\mathrm{NA}^2\gamma_p\tau}\right)^2 \gamma_e^{bkg}\tau. \qquad (4.12)$$

Notice that both the photon shot noise and the scatter scale as $1/\tau$. Therefore the scatter can not be reduced by increasing the probe time unlike the readout noise which scales as $1/\tau^2$. In our experiment, the background scatter currently limits the noise floor of our imaging system (see Section 6.2).

Since the photon shot noise of the atom signal, the readout noise, and noise due to the background scatter are independent of each other, the total noise in fluorescence imaging can be written as

$$\sigma^2_{\mathrm{Tot}} = \sigma^2_{\mathrm{PSN}} + \sigma^2_{\mathrm{RO}} + \sigma^2_{bkgscatt}. \qquad (4.13)$$

Currently, our imaging system is limited by a background scatter of approximately 8 atoms on an area of 290 x 208 μm^2. To reduce the readout noise the camera pixels, are binned 16 by 16. (see Section 6.2). The noise due to background scatter can most likely be further reduced by decreasing the size of the probe beams, which currently have a $1/e^2$ waist of 12.5 mm.

4.3   Calibration

In order to determine the actual value of the saturation parameter s_0, we measure the number N_p of photons scattered by the atom in terms of the detuning and fit the data to the scatter rate (see Equation 4.7)

$$N_p = \frac{A}{1 + s_0 + (2\Delta/\Gamma)^2}, \qquad (4.14)$$

where the quantum efficiency, the numerical aperture, and probe time have all been absorbed into the constant A. This is a very reliable method for determining the saturation parameter. As it is independent of the collection efficiency of the camera
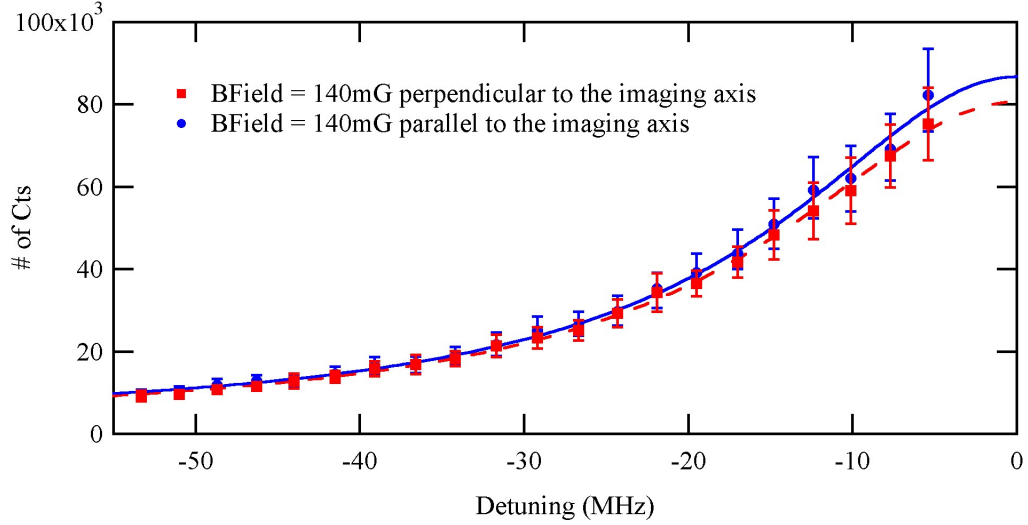
Figure 4.3: Measurement of the saturation parameter in fluorescence imaging for both a magnetic field parallel (blue circles and solid line) and perpendicular (red squares and dashed line) to the probe beam. The error bars are experimental standard deviation of 11 runs. The fit gives a saturation parameter of 30 ± 2 and 32 ± 1, respectively, and agrees with the expected value. Given the margin of error and experimental drifts, the saturation parameter can be considered to be independent of the orientation of the magnetic field

and the number of atoms, it does not allow the determination of the collection efficiency. The saturation parameter is determined for both a magnetic field along the imaging axis and perpendicular to the imaging axis to test if, in this configuration, there is any dependence of the scatter rate on the orientation of the magnetic field. In both cases the magnitude of the magnetic field was 140 mG. The data is shown in Figure 4.3. For a magnetic field parallel (perpendicular) to the probe beam, the saturation parameter was found to be 30 ± 2 (32 ± 1). Given the margin or error and experimental drifts, the saturation parameter can be considered to be independent of the orientation of the magnetic field. This is to be expected as the atoms are probed with three orthogonal pairs of counterpropagaging beams and therefore see the same polarization in all directions. The value for the saturation parameter also agrees with the expected value assuming isotropic polarization and given the power and beam

waist of our probe beams. As a side note, this method cannot be used for determining the saturation parameter for absorption imaging as changing the detuning will add diffraction effects making it difficult to actually measure the number of atoms or more exactly the number of photons that are being absorbed.

CHAPTER V

BEC IN A LATTICE

Bose-Einstein condensation in optical lattices [73] has been a continuously growing area of research. These systems are particularly interesting as model systems of pure quantum mechanical effects. Applications range from the investigation of solid-state systems (such as Bloch oscillations [74], Josephson junctions [75] and the Mott-insulator phase transition [76, 32]), the study of low-dimensional quantum gases [77, 78], the study of nonlinear effects (such as squeezed states [31]), to atom interferometry, just to mention a few. For a more complete review of this vast field see [79, 80, 81]. In optical lattices the parameters characterizing the lattice potential, such as its depth and shape, can easily be manipulated by changing the laser intensity, geometry, and frequency. Due to this versatility they have become a widely used tool in atom optics. Besides being an ideal testbed for quantum mechanical effects, optical lattices can be used to store quantum information [82, 83].

The ability to address and manipulate the quantum state of the atoms trapped in the individual sites of optical lattices opens up the possibility to perturb the system on a local scale and has been demonstrated using light [84], microwaves [67], and electron microscopy [85]. In addition to manipulating the quantum state, it's also important to be able to readout the local quantum state and to observe the local density distribution.

In our experiment, we use one-dimensional CO_2 laser lattice with a lattice spacing $\lambda/2 = 5.3\ \mu$m. We discuss the trap parameters, the resolution of our imaging system, our ability to address and manipulate single lattice sites using microwaves, and the interference between two lattice sites in the condensate.

5.1 Lattice Trap Parameters

5.1.1 Trap Depth

The spatial mode of our CO_2 laser can be approximated with a TEM_{00} mode of a Gaussian. The intensity of such a Gaussian beam traveling in the $\hat{z}$-direction focused at $z = 0$ is expressed as

$$I(x, y, z) = \frac{2P}{\pi w(z)} \exp\left[-2\frac{x^2 + y^2}{w(z)^2}\right], \tag{5.1}$$

where

$$w(z) = w_0\sqrt{1 + \left(\frac{z}{z_r}\right)^2}. \tag{5.2}$$

Here P is the laser power, $z_r = \pi w_0^2/\lambda$ is the Rayleigh range, $w_0 = w(0)$ is the minimum beam waist, and λ is the wavelength of the laser. In order to create a one dimensional lattice, we counterpropagate two beams to create an interference pattern with a distance $\lambda/2$ between the maxima and minima of the resulting light intensity:

$$I(x, y, z) = \frac{8P}{\pi w(z)} \exp\left[-2\frac{x^2 + y^2}{w(z)^2}\right] \cos^2(2\pi z/\lambda). \tag{5.3}$$

The corresponding trap potential is then

$$U(x, y, z) = \alpha\frac{I(x, y, z)}{2c\epsilon_0} \tag{5.4a}$$

$$= \frac{4U_0}{\sqrt{1 - \left(\frac{z}{z_r}\right)^2}} \exp\left[-2\frac{x^2 + y^2}{w(z)^2}\right] \cos^2(2\pi z/\lambda) \tag{5.4b}$$

where

$$4U_0 = \frac{1}{\pi\epsilon_0}\frac{16\alpha}{cw_0^2}P \tag{5.5}$$

is the trap depth. Here α is the static polarizability, and for ^{87}Rb ground states, $\alpha = 5.3 \times 10^{-39}$ m^{2}C/V. After compression and forced evaporative cooling, the CO_2 laser beam has a waist $w_0 = 25$ μm and a final power ≈ 25 mW. The resulting trap depth of the lattice is ≈ 7 μK.
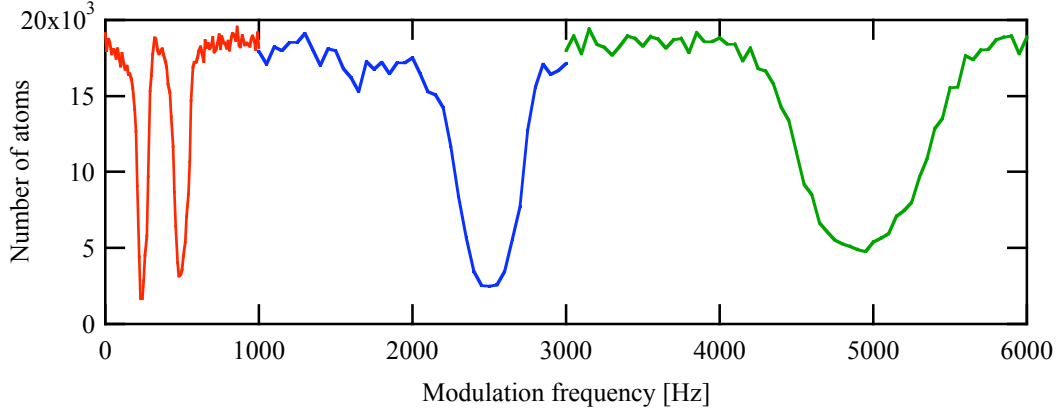
Figure 5.1: Spectrum of the resonances in the parametric heating of the atoms in the optical lattice. The lower two resonances are at the radial and at twice the radial trapping frequency and the higher two resonances are the axial and at twice the axial trapping frequency. The experimental conditions were changed throughout the scan to take into account the different strengths of the resonances. The red line is taken with an amplitude modulation of 10 % for 100 cycles, the blue line with a 20 % modulation for 500 cycles, and the green line with a 10 % modulation for 500 cycles.

5.1.2 Trap Frequencies

When the temperature of the trapped cloud is much lower than the trap depth, the potential can be expanded around $(x, y, z) = (0, 0, 0)$ and can be approximated with a simple harmonic oscillator. For the condensate, the typical values of the temperatures are a few hundred nK, which is over ten times smaller than the trap depth, therefore the harmonic oscillator approximation is applicable. The trap frequencies are

$$\omega_{r_i} = \left[-\frac{1}{m} \frac{\partial^2 U(x, y, z)}{\partial r_i^2} \right]_{(x,y,z)=(0,0,0)}^{1/2}, \tag{5.6}$$

where $r_i = x, y, z$, and m is the mass of the atoms. The frequencies of the middle lattice condensate are

$$\omega_\rho = \sqrt{\frac{16 U_0}{m w_0^2}}, \tag{5.7a}$$

$$\omega_z = \sqrt{\frac{U_0 (2\pi)^2}{m \lambda^2}}. \tag{5.7b}$$

Given the typical CO_2 laser parameters above, the trap frequencies are expected to be $\omega_\rho = 2\pi \times 340$ Hz and $\omega_z = 2\pi \times 3500$ Hz, where z is along the CO_2 laser axis.

The trap-frequencies can be verified using parametric heating [86]. The equation of motion of a sinusoidally driven harmonic oscillator is

$$\ddot{x} = \omega_0^2 \left(1 + A \sin \Omega t \right) x, \tag{5.8}$$

where ω_0 is frequency of the harmonic oscillator (in our case the trap frequency), A is the modulation amplitude, and Ω the modulation frequency. When the modulation frequency is twice the trap frequency $\Omega = 2\omega_0$ or a sub harmonic thereof, i.e. $\Omega = 2\omega_0/n$ where n is an integer, the energy of the oscillator grows exponentially. As a result, the atoms are heated up and are boiled out of the trap. An example of a trap frequency measurement for the trap parameters given above is shown in Figure 5.1. We modulate the trap frequency by modulating the power of the CO_2 by 10 - 20 % for 100 - 500 cycles and then measure the remaining number of atoms in the trap. For both the radial and the axial trap frequency we observe significant trap loss for $\Omega = 2\omega_0$ and $\Omega = \omega_0$. The measurements for the radial and axial trap frequencies are $\omega_\rho = 2\pi \times 240$ Hz and $\omega_z = 2\pi \times 2.5$ kHz, respectively.

5.1.3 Thomas-Fermi Radii

A condensate at zero temperature is described by the Gross-Pitaevskii equation in a mean-field approximation. Within the Thomas-Fermi (T-F) approximation [87], in which the kinetic energy term (also referred to as the quantum pressure) is neglected, the density in the trap is given by

$$n_{TF}(\vec{r}) = \max \left[\left(\frac{\mu - U(\vec{r})}{g} \right), 0 \right], \tag{5.9}$$

where $U(\vec{r})$ is the trap potential, μ the chemical potential, $g = 4\pi \hbar^2 a/m$ the two-body interaction strength, a the s-wave scattering length, and m the mass of the atoms. In this case, the interaction between the atoms is modeled as a contact potential, which is valid if the mean particle spacing is less than the scattering length a. For a

harmonic external potential

$$U(x, y, z) = \frac{1}{2}m(\omega_x x^2 + \omega_y y^2 + \omega_z z^2) \tag{5.10}$$

and

$$n_{TF}(x, y, x) = \frac{\mu}{g}\max\left[\left(1 - \sum_{i=x,y,z}^{3} \frac{r_i^2}{R_i^2}\right), 0\right] \tag{5.11}$$

with

$$R_i = \sqrt{\frac{2\mu}{m\omega_i^2}} \tag{5.12}$$

defined as the Thomas-Fermi radii. Using the normalization condition $N = \int n(\vec{r})\mathrm{d}^3 r$, the chemical potential is calculated as

$$\mu = \left(\frac{15\hbar^2 m^{1/2}}{2^{5/2}}N\bar{\omega}^3 a\right)^{2/5}, \tag{5.13}$$

where N is the total number of atoms in the condensate, $\bar{\omega} = \sqrt{\omega_x \omega_y \omega_z}$ is the mean trap frequency. The column density is obtained by integrating over one of the coordinates

$$\tilde{n}_{TF}(x, y) = \frac{4\mu}{3g}R_z\max\left[\left(1 - \sum_{i=x,y}^{3} \frac{r_i^2}{R_i^2}\right), 0\right]^{3/2}. \tag{5.14}$$

In terms of the atom number N and the T-F radii R_i, the density distribution and the column density are given by

$$n_{TF}(x, y, x) = \frac{15N}{8\pi \prod_i R_i}\max\left[\left(1 - \sum_{i=x,y,z}^{3} \frac{r_i^2}{R_i^2}\right), 0\right], \tag{5.15a}$$

$$\tilde{n}_{TF}(x, y) = \frac{5N}{2\pi R_x R_y}\max\left[\left(1 - \sum_{i=x,y}^{3} \frac{r_i^2}{R_i^2}\right), 0\right]^{3/2}, \tag{5.15b}$$

respectively. For typical parameters of our trap, i.e. frequencies $(\omega_\perp, \omega_z) = 2\pi \times (340, 3500)$ Hz, $N = 4000$, we get $\mu = 260$ nK, and $(R_\perp, R_z) = (3.3, 0.32)$ μm and the peak density $n_0 = \mu/g = 6.9 \times 10^{14}$ atoms/cm^3. The lifetime of the condensate was determined to be ≈ 1.3 s.

The T-F radii defined above are strictly speaking only valid for a condensate in a trap. However, the time of flight radii are simply described by the following

parameterization and equation of motion [88]:

$$R_i(t) = \lambda_i(t) R_i(0), \tag{5.16}$$

with

$$\ddot{\lambda}_i(t) = \frac{\omega_i}{\lambda_i \lambda_x \lambda_y \lambda_z}, \tag{5.17}$$

and $i = x, y, z$. In general, these equations have to be integrated numerically for a given set of trap frequencies ω_i. As a result, the time of flight density profile is a simple rescaling of the *in situ* spatial density (Equation 5.15) where $R_i(0)$ is substituted by $R_i(t)$ for a given time of flight t.

5.2 Addressing Single-Sites

5.2.1 Imaging the lattice

For a better imaging resolution, we mounted our imaging lens, a high aperture laser objective (HALO) with a numerical aperture NA $= 0.31$ and focal length $f = 50$ mm, inside the chamber. The diffraction limit of a lens is given by Rayleigh's criterion for just-resolvable diffraction patterns. The minimum separation x_{min} of two-just-resolved objects near the focal plane of the lens is given by

$$x_{min} = \frac{1.22\lambda}{\mathrm{NA}}, \tag{5.18}$$

where λ is the wavelength of the imaging light. In our case, $\lambda = 780$ nm and we expect $x_{min} = 1.5$ μm. This would allow us to resolve the single lattice sites, which are separated by 5.3 μm. To check the resolution, we did a bench test by imaging a target (AirForce1951 target) with structures of known width and separation (see Figure 5.2). The test imaging system consisted of our imaging lens (a HALO with $f = 50$ mm), an achromat lens with a focal length $f = 500$ mm and a CCD camera with a physical pixel size of 16 μm. A visual assessment of the target image clearly shows that structures less than 2.8 μm can be resolved. It is important to note that
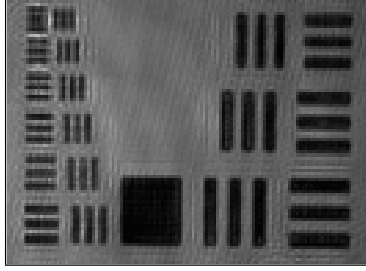
Figure 5.2: Image of an imaging target in order to estimate the imaging resolution of the system. The group of small lines on the left have the following widths and spacings starting from the top: 2.2 μm, 2.5 μm, 2.8 μm, 3.1 μm, 3.5 μm, 3.9 μm. The pixel size in the image is 1.6 μm limiting the resolution of the image.

the resolution of the target image is most likely limited by the pixel size of the camera as a pixel corresponds to 1.6 μm in this set-up.

To image the individual lattice sites of our condensate, we use a 20x microscope objective together with a telescope consisting of our imaging lens and a lens identical to the imaging lens (see Figure 2.12(a)). An example of the full lattice condensate and for a single lattice site imaged for 15 μs with a probe power $\approx 10I_{sat}^0$ is given in Figure 5.3(a) and 5.3(b), respectively. The Thomas-Fermi radius of a lattice condensate in the axial direction is only ≈ 0.32 μm, which is significantly smaller than the diffraction limit $x_{min} = 1.5$ μm of the imaging lens. Therefore, we will not be able to accurately count the atoms *in situ* using absorption imaging. Apart from the size of the condensate, the peak optical density for $N = 4000$ atoms in a lattice site is 880, which is over two orders of magnitude higher than the maximum observable optical density (see Chaper 3.2.6).

Firstly, the diffraction effects visible in the condensate images Figure 5.3 are a result of the high density of the atoms in the lattice and the limited imaging resolution compared to the axial size of the condensate. Secondly, we suspect that our actual imaging resolution is reduced to ≈ 3 mm by a misplacement of the lens inside the camera with respect to the trap location. The suspicion is based on the location of the image formed with our imaging system. Our simple 10x imaging set-up (see Figure

2.12(a)) consists of the imaging lens ($f_1 = 50$ mm) and an achromat ($f_2 = 500$ mm). The distance of the achromat with respect to the imaging system is chosen such that the probe beam is re-collimated after the achromat ($d = f_1 + f_2$) , so that the system can be used for both fluorescence and absorption imaging. If the condensate is in the focal plane of the imaging lens, the image of the condensate is expected to form $f_2 = 500$ mm after the second lens. In actuality, the image is formed 1100 mm after the second lens. Doing a simple ray-trace [89], we conclude that the condensate is not actually in the focal plane of the imaging lens but is slightly closer. The ray-trace estimates the distance between the condensate and the imaging lens to be 44 mm, which would indicate that the imaging lens is positioned 6 mm too close to the trap.

5.2.2 Addressing single sites with microwaves

We can address and manipulate the individual lattice sites separately using microwaves. The experiment starts with a pure $m_F = 0$ lattice condensate. We then apply a microwave π-pulse resonant with the $F = 1, m_F = 0 \longleftrightarrow F = 2, m_F = -1$ transition. The atoms are then imaged using absorption imaging with light resonant with the $F = 2 \longleftrightarrow F' = 3$ hyperfine transition. As a result, the atoms remaining in the $F = 1$ state are dark in the image. In order to spectroscopically resolve the individual lattice sites, we apply, similar to [67], an inhomogeneous magnetic field of the form

$$\vec{B}(\vec{r}) = (B_x, B_y, B_z) = (0, 0, B_0) + (-\frac{x}{2}, -\frac{y}{2}, z)B' \tag{5.19}$$

with $B_0 = 2$ G, $B' = 20$ G/cm, and $\hat{z}$ along the CO_2 laser axis. This magnetic field introduces a position-dependent hyperfine transition frequency via the Zeeman effect and therefore allows us to site-selectively address the individual condensates using microwaves (see Figure 5.3). We create this magnetic field with a pair of gradient coils whose symmetry plane is shifted 10 mm along the CO_2 laser axis with respect to the condensates. The relatively large homogeneous offset field B_0 ensures the
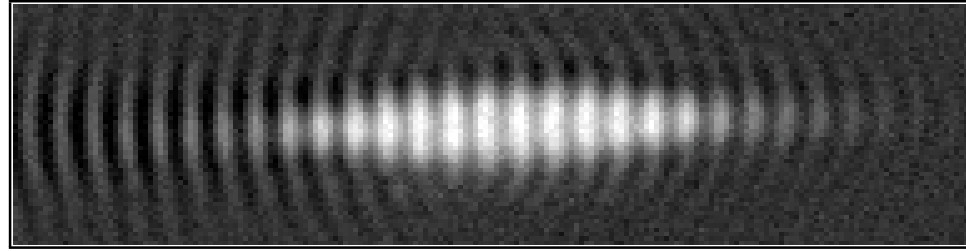
(a)
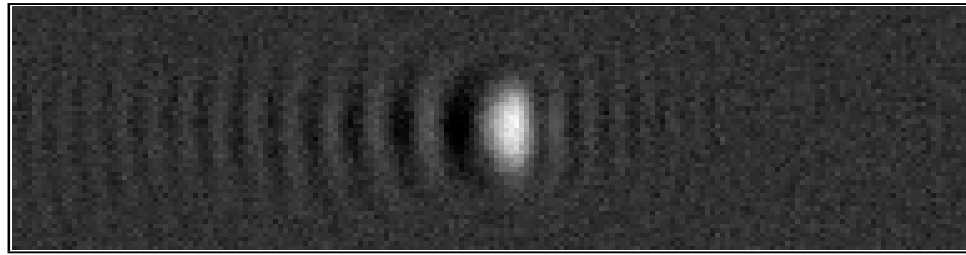
(b)
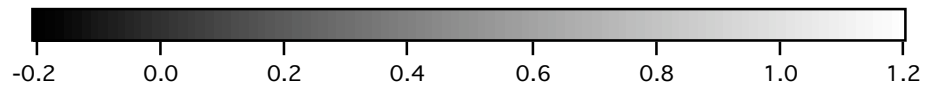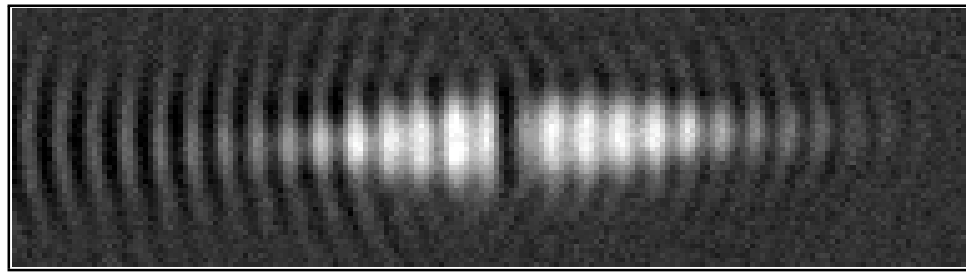
(c)

Figure 5.3: *In situ* images of the lattice condensates after the following manipulations: (a) a pure $F = 1, m_F = 0$ lattice condensate with no microwave manipulation, (b) excitation of a single lattice site from the $F = 1, m_F = 0$ state to the $F = 2, m_F = -1$ using microwaves, (c) excitation of a single lattice site to the $F = 2, m_F = -1$ state and removal of these atoms with light resonant with the $F = 2 \longleftrightarrow F' = 3$ transition. In images (a) and (c) the atoms in the $F = 1, m_F = 0$ are transferred to the $F = 2, m_F = 0$ before imaging.

degeneracy of the different microwave transitions and more importantly reduces the variation of the magnetic field strength along the radial direction of the condensates. In the discussion below, unless otherwise specified, we work with the hyperfine states $F = 1, m_F = 0$ and $F = 2, m_F = -1$. The offset field shifts the transition frequency from the $F = 1, m_F = 0 \longleftrightarrow F = 2, m_F = -1$ by -1.5 MHz with respect to the unperturbed value of 6.834 GHz. The gradient field along the lattice produces a position-dependent frequency shift of 1.4 kHz/μm, corresponding to a 7.5 kHz frequency shift between two adjacent lattice sites compared to a frequency shift in the radial direction of a condensate of less than 1.5 Hz. To excite the atoms to the $F = 2, m_F = -1$ state, we use a π-pulse with a Blackman shaped microwave amplitude $A(t) = A_{\text{eff}}(0.5 \cos(\pi[2t/\tau - 1]) + 0.08 \cos(2\pi[2t/\tau - 1] + 0.42)$ for $0 \leq t \leq \tau$ [90]. We use a Blackman shaped pulse because its frequency spectrum (or probability of transfer as a function of frequency) is very similar to that of a Gaussian function. It does not have the "feet" of the sinc-function $\text{sinc}(x) \equiv \sin x / x$, the frequency spectrum resulting from a square pulse. This helps prevent off-resonant excitation of atoms in the adjacent sites that would otherwise occur for a square pulse. Since every lattice site is filled, we also have to choose the pulse length carefully. For example, a very long pulse will transfer all the atoms in the target site to the $F = 2, m_F = -1$ state, but will also excite a large portion of the neighboring sites. Whereas a very short pulse leaves the neighboring sites in their initial state but will only transfer a fraction of the targeted condensate into the $F = 2$ state. The optimal pulse for single site addressability has a Fourier spectrum that has a high transfer probability over the whole condensate and goes to nearly zero transfer probability at the neighboring condensates. We found that a pulse length of $\tau = 520$ μs works very well for our experiment. The full width at half max of the frequency spectrum is 3.4 kHz and the full spectral width is 7.5 kHz, so that the transition probability from the neighboring sites is negligible. If the frequency of the pulse is resonant with the center of the
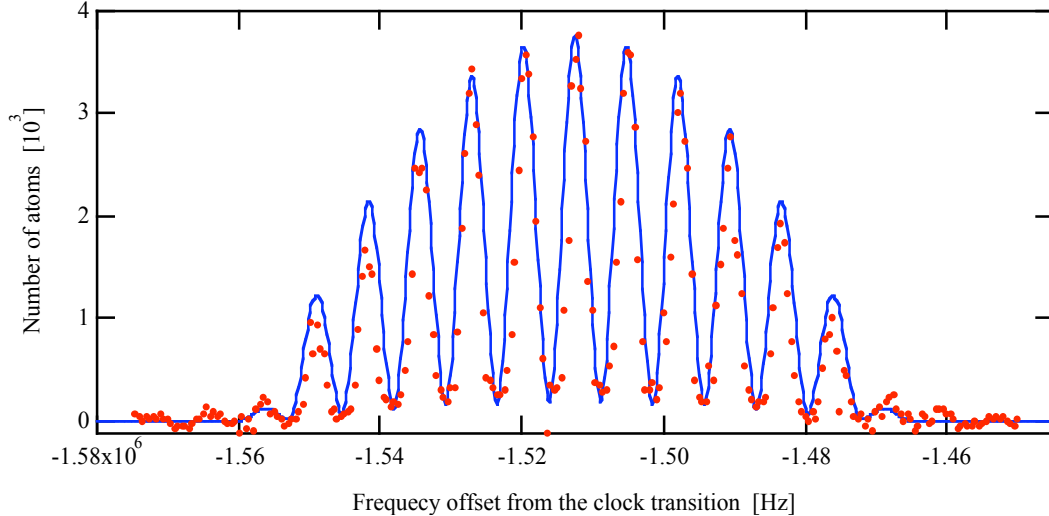
Figure 5.4: Resolving single lattice sites using microwaves. The figure shows the measured atom number versus the applied microwave frequency. The atoms were imaged after a time of flight of 5 ms. The microwave pulse was a Blackman pulse with $\tau = 520$ μs.

lattice site, then the edges of the condensate, each $R_z/2 = 0.16$ μm from the center, are transferred with a probability of over 99.5 %. A full microwave spectrum of the lattice condensate is show in Figure 5.4. For frequencies resonant with the half-distance between two lattice sites the spectral width of the pulse is just large enough to excite a small fraction of the two lattice sites and therefore the spectrum does not fully go to zero between the lattice sites. In this experiment, the atoms were probed after a time of flight of 5 ms, so that the optical density is low enough ($\approx$ 2) to properly count the atoms. In Figure 5.5, we show a comparison between spectra with different pulse lengths, $\tau = 520$ μs and $\tau = 1000$ μs. For a pulse length $\tau = 1000$ μs, the full width (the full width at half max) of the frequency spectrum is 4.0 kHz (1.8 kHz).

To illustrate the single-site addressability, we compare *in situ* images of a pure unperturbed $F = 1, m_F = 0$ lattice condensate, a single site, and the lattice condensate with a single site removed (see Figure 5.3). In all images the atoms are probed with light resonant with the $F = 2 \longleftrightarrow F' = 3$ transition such that only atoms in the
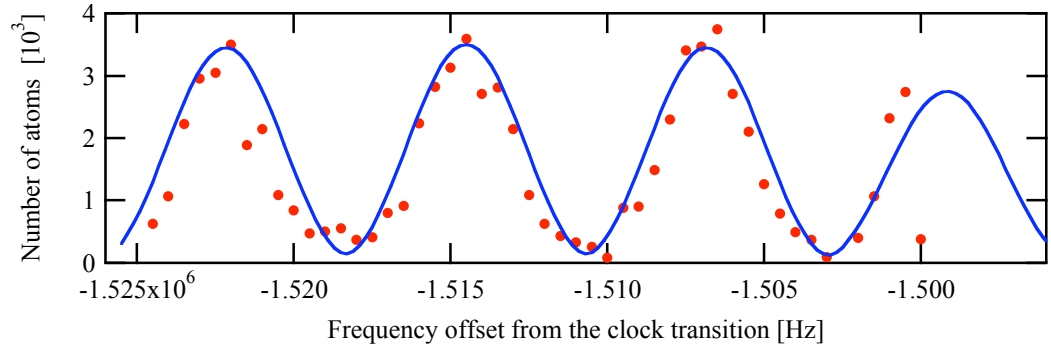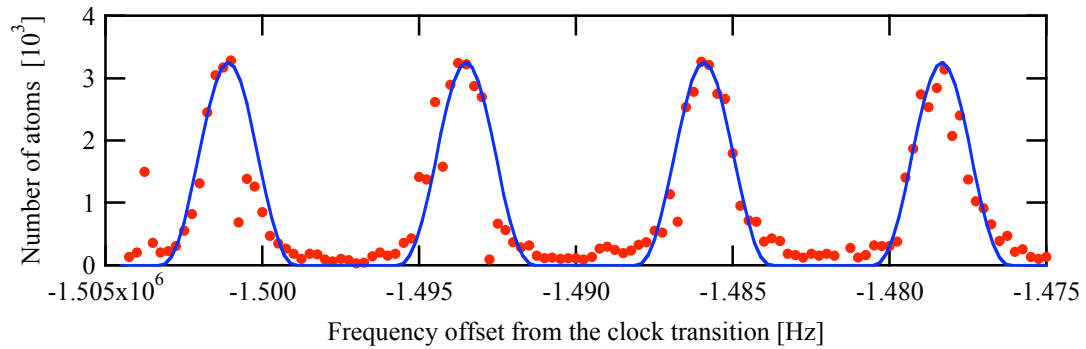
Figure 5.5: Microwave spectra of a lattice condensate with different pulse lengths (a) $\tau = 520$ μs and (b) $\tau = 1000$ μs. The amplitude envelope of the pulses is a Blackman pulse.

$F = 2$ hyperfine state interact with the light and are visible. The images above are taken with a short probe pulse (15 μs) in order to avoid blurring of the image due to heating of the atoms. The probe intensity is $I \approx 10 I_{sat}^0$. We image the unperturbed lattice condensate (see Figure 5.3(a)), by transferring the atoms in the lattice to the $F = 2, m_F = 0$ on the clock transition. Before transferring a single lattice site to the $F = 2, m_F = -1$ state, we first determine the correct transition frequency by taking a microwave spectrum across the condensate (see Figure 5.4 for an example). Figure 5.3(b) depicts the single lattice imaged without an additional microwave pulse on the clock transition such that the rest of the lattice remains dark. The image clearly shows a single lattice site. Alternatively, we can remove the atoms in this lattice site and image the remaining lattice sites (see Figure 5.3(c)). This is done by pulsing on the probe beam after the microwaves, such that the atoms in the $F = 2$ state are heated out of the lattice trap, whereas the atoms in the $F = 1$ state are not affected by the probe light and remain in the trap. We then take an image as described above. The populations of the lattice site have been almost completely removed, while the remaining lattice is only slightly perturbed. Due to the limitation of our resolution and to diffraction effects it is difficult to quantitatively determine the efficiency of the transfer from these images. In principle, we can manipulate any number of lattice site. In the following section, for example, we excite two lattice sites.

5.3   *Interfering two lattice sites*

In a Bose-Einstein condensate, the atoms macroscopically occupy a single-particle quantum state such that the whole condensate behaves as a coherent matter wave. In [5], the macroscopic quantum coherence of the BEC was observed as a matter-wave interference by releasing two spatially separated the condensates allowing them to overlap during the time of flight. The period of the interference pattern from two expanding condensates is given by the de Broglie wavelength of the relative motion

of the two independent condensates

$$\lambda_{rel} = \frac{h}{mv_{rel}}, \tag{5.20}$$

where the relative velocity is determined by

$$v_{rel} = \frac{d}{\tau_{exp}}. \tag{5.21}$$

Here d is the separation of the condensates, m the mass of the atoms, and τ_{exp} the time of flight. In this experiment, we excite two lattice sites to the $F = 2, m_F = -1$ state and let the condensates expand for $\tau_{exp} = 16$ ms. The experiment is done both of adjacent lattice sites $d = 5.3$ μm (see Figure 5.6) and lattice sites separated by lattice site $d = 10.6$ μm (see Figure 5.7).

For each setting the experiment is repeated 28 times. The probe power is $\approx 2I_{sat}^0$ and the probe time 50 μs. To analyze the data, we fit the axial density profile of the condensate, with

$$F(z) = G(z) \left[1 + A \cos \left(\frac{2\pi z}{\lambda_{rel}} + \phi \right) \right], \tag{5.22}$$

where $G(z)$ is a Gaussian envelope, A is the contrast of the interference pattern, and ϕ is the relative phase between the two condensate [91, 92]. The horizontal profile is obtained by averaging over a vertical region of 50 μm (see Figures 5.6(a) and 5.6(a) for an example). The fitted periods of 14.0 μm and 6.9 μm for adjacent lattice sites and lattice sites separated by a lattice site, respectively, are in good agreement with the expect values. In Figures 5.6(c) and 5.6(c), we summarize our results. The average contrast observed for adjacent sites was 0.31, whereas for lattice sites separated by a lattice site the average contrast was 0.15. In theory, the interference of two condensates should give a fringe visibility of 1. In our experiment the visibility of the fringes is limited by the size of the condensate in the direction of the imaging axis and the blurring of the image during the probe pulse. After a time of flight of 16 ms, the diameter of the cloud is ≈ 56 μm, whereas our depth of field is ≈ 10 μm.

74

Part of the condensate will therefore be out of focus and reduce the contrast of the fringes. Additionally, the cloud is blurred during imaging by $x \approx 2.8$ μm and is pushed along the probe beam direction by $z \approx 94$ μm. In both cases, the phase ϕ was randomly distributed between 0 and 2π indicating that the condensates are phase uncorrelated. This is expected since the condensates are created independently and tunneling between sites is negligible due to the large spacing of our optical lattice.

In summary, we have created an array of independent condensates in the standing wave potential of a CO_2 laser. The lattice spacing is 5.3 μm, which is larger than our imaging resolution ≈ 3 μm, and therefore allows us to image the *in situ* structure of the lattice using absorption imaging. Diffraction effects, however, prevent us from extracting quantitative measurements from the *in situ* images. We have successfully addressed and manipulated the single lattice sites using microwaves and thus have demonstrated that microwaves can be used to measure the number of atoms in an individual lattice site. By interfering two lattice condensates, we have shown the coherence of the individual lattice sites.

Averaged Column Density (a.u.)

Fringe contrast = 0.36
Relative phase = 143°

····· Experimental data
—— Theoretical fit

Position (μm)

(a)

(b)

(c)

Figure 5.6: Interference of two adjacent lattice sites. (a) Horizontal profile of the image shown in (b) averaged over a region of 50 μm. (b) Absorptive image of two interfering lattice sites after a time of flight of 16 ms. The field of view is 338 μm x 160 μm. (c) Polar plot of the fringe contrast and relative phases for 28 images of two interfering condensates.
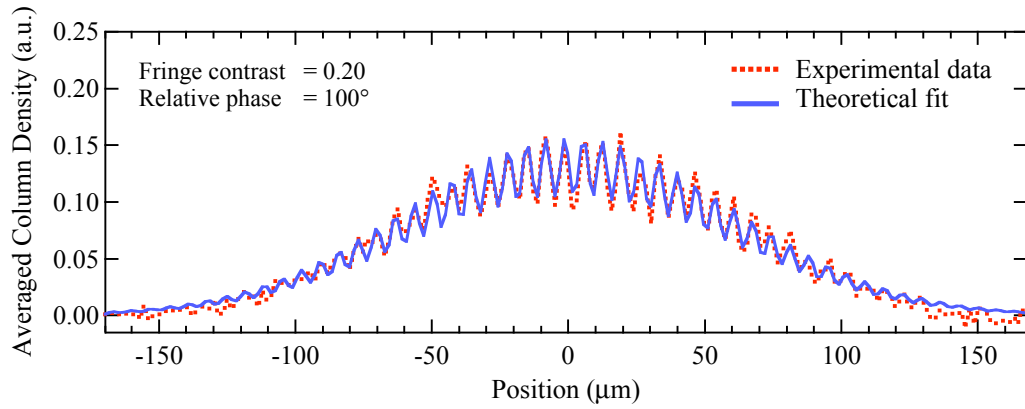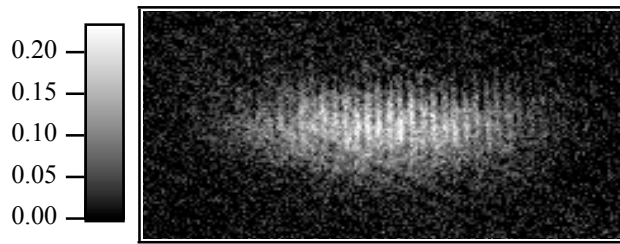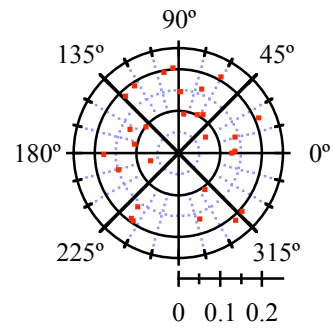
Figure 5.7: Interference of two adjacent lattice sites. (a) Horizontal profile of the image shown in (b) averaged over a region of 50 μm. (b) Absorptive image of two interfering lattice sites after a time of flight of 16 ms. The field of view is 338 μm x 160 μm. (c) Polar plot of the fringe contrast and relative phases for 28 images of two interfering condensates.

CHAPTER VI

QUANTUM PROJECTION NOISE

In this chapter, we determine the noise floor of our imaging system for both absorption and fluorescence imaging. The sensitivity of our imaging system is demonstrated by measuring small condensates created in the $F = 2$ state by transferring a small fraction of the total BEC from the $F = 1$ to the $F = 2$ ground state using microwave radiation. Additionally, we measure the fluctuations in the atom number and determine the contributions due to imaging noise, quantum projection noise, and fluctuations in the total atom number due to technical in noise in the experiment. Before presenting the results of our small atom number measurements, we explain the concept of quantum projection noise and derive magnitude of this noise for an ensemble of N uncorrelated particles. Finally, we implement a new calibration method based on quantum projection noise.

Measurements on an ensemble of uncorrelated particles are limited by quantum projection noise. This noise is an intrinsic property of quantum mechanics and is related to the uncertainty in the measurement of a quantum state. In order to illustrate the quantum projection noise let us consider a two-level atom with the two states $|\uparrow\rangle$ and $|\downarrow\rangle$. If the atom is prepared in either one of the two states $\phi = |\uparrow\rangle$ (or $|\Psi\rangle = |\downarrow\rangle$), a measurement of the state will always yield that the atom is in the upper (lower) state. However, if the atom is prepared in a superposition of the two states $\phi = c_\uparrow |\uparrow\rangle + c_\downarrow |\downarrow\rangle$ with $c_\uparrow \neq 0$ and $c_\downarrow \neq 0$, the outcome of the measurement, i.e. the atom is in the upper state or the atom is in the lower state, cannot be predicted with certainty. One measurement might indicate that the atom is in the upper state, whereas another measurement on an identical system can indicate that

the atoms is in the lower state. If state is normalized $|c_\uparrow|^2 + |c_\downarrow|^2 = 1$, then $|c_\uparrow|^2 = p_\uparrow$ and $|c_\downarrow|^2 = p_\downarrow$ correspond to the probabilities of finding the atoms in the upper and lower state, respectively. This indeterminacy in the measurement is independent of the state preparation and the resulting fluctuations in the measurement are referred to as quantum projection noise (QPN), according to the interpretation that in the measurement process the state vector is randomly projected onto one of the states.

Defining the projection operator $P_\uparrow \equiv |\uparrow\rangle\langle\uparrow|$, the variance of the measurement of the state $|\uparrow\rangle$ of a single atom can be calculated

$$(\Delta P_\uparrow)^2 \equiv \langle P_\uparrow^2\rangle - \langle P_\uparrow\rangle^2 \tag{6.1a}$$

$$= \langle P_\uparrow\rangle - \langle P_\uparrow\rangle^2 = p_\uparrow(1 - p_\uparrow). \tag{6.1b}$$

Given an ensemble of N identical but independent atoms, the probabilities will combine according to the binomial distribution such that the probability of measuring a given value of N_i atoms in the $|i\rangle$ state is

$$P(N_i, N, p_i) = \frac{N!}{N_i!\,(N - N_i)!}\,(p_i)^{N_i}\,(1 - p_i)^{(N - N_i)}, \tag{6.2}$$

which has a variance of

$$\sigma_i^2 = (\Delta P_{N_i})^2 = Np_i(1 - p_i), \tag{6.3}$$

and the covariance of measuring N_i and N_j with $i \neq j$ is

$$\sigma_{ij}^2 = -Np_ip_j. \tag{6.4}$$

Here, the states were labeled with i and j instead of the specific two-level labels in order to emphasize that this formalism is also valid for a multinomial distribution, for example for three-level atoms.

6.1 Small Atom Numbers in the $F = 2$ State

In order to demonstrated the sensitivity of our imaging system, we create small condensates in the $F = 2$ state by transferring a small fraction of the total BEC from

the $F = 1$ hyperfine ground state to the $F = 2$ ground state using microwaves. This allows us to test our imaging system and determine the smallest condensate that we can imaging in time of flight. In order to lift, the degeneracy of the Zeeman levels in the $F = 1$ and $F = 2$ hyperfine states, we apply a large magnetic field ≈ 2 G, which splits the energy levels of adjacent Zeeman states by ≈ 1.4 MHz. The frequency spectrum of the microwaves is determined by the pulse length. For pulse lengths ~ 100 μs, the width of the frequency spectrum is ~ 10 kHz, which two orders of magnitude lower than the frequency splitting of the energy levels. A on-resonance microwave transition from a Zeeman level in the $F = 1$ hyperfine ground state to one in the $F = 2$ hyperfine ground state therefore reduces to a closed two-level system as the radiative decay from the hyperfine ground states is negligible. See Figure 2.9 for a schematic of the Zeeman levels and the allowed transitions.

In our experiment we start with a pure $|F = 1, m_F = 0\rangle$ condensate and transfer the atoms on the clock transition to the $|F = 2, m_F = 0\rangle$ state, because this transition is insensitive to fluctuations of the magnetic field. The two-level system can be described by the wavefunction

$$\psi(t) = c_1(t)e^{-i\frac{E_1 t}{\hbar}}|1\rangle + c_2(t)e^{-i\frac{E_2 t}{\hbar}}|2\rangle, \tag{6.5}$$

where $|1\rangle$ and $|2\rangle$ represent the eigenfunctions of the Zeeman levels $|F = 1, m_F = 0\rangle$ and $|F = 2, m_F = 0\rangle$, respectively, and E_1 and E_2 are the corresponding energy eigenvalues. Assuming all the atoms are initially in the $|F = 1, m_F = 0\rangle$ state the coefficients $c_i(t)$ are given by

$$c_1(t) = \left[\cos\left(\frac{\Omega' t}{2}\right) + i\frac{\Delta}{\Omega'}\sin\left(\frac{\Omega' t}{2}\right)\right]e^{i\Delta t/2}, \tag{6.6a}$$

$$c_2(t) = -i\frac{\Omega}{\Omega'}\sin\left(\frac{\Omega' t}{2}\right)e^{-i\Delta t/2}, \tag{6.6b}$$

where Ω is the Rabi frequency, Δ is the detuning from resonance and $\Omega' = \sqrt{\Delta^2 + \Omega^2}$ [61]. For on-resoncence microwave radiation, the probabilities to find the atoms in

levels $|F = 1, m_F = 0\rangle$ and $|F = 2, m_F = 0\rangle$ as a function of the microwave pulse length are thus given by $p_1(t) = \cos^2\left(\frac{\Omega t}{2}\right)$ and $p_2(t) = \sin^2\left(\frac{\Omega t}{2}\right)$, respectively. An example, of such an oscillation is shown in the inset of Figure 6.1(a).

For various short microwave pulses, we measure the number of atoms excited to the $F = 2$ state. The atoms are imaged without the repump laser such that the atoms remaining in the $F = 1$ state remain dark. The measurement is repeated multiple times in order to determine the fluctuations in the atom numbers. As mentioned above, QPN also contributes to the fluctuations in atom number and therefore must be taken into account. The fluctuations of the atom number due to QPN is $\sigma^2_{\text{QPN}}(N_2) = p_2(1 - p_2)N = (1 - p_2)N_2 = N_2 - N_2^2/N$. In addition the total atom number will fluctuate due to technical noise in the experiment. In general, this noise can be described by $\sigma^2_{\text{tech}}(N) = (\beta N)^2$, where β is the percentage of fluctuations due to experimental imperfections. As a result, the technical noise for the atoms in the $F = 2$ state is given by $\sigma^2_{\text{tech}}(N_2) = (\beta N_2)^2$. Finally, there is also the imaging noise (see Chapters 3 and 4). In both imaging methods, the noise depends on the region of interest (see Equation 3.25 and Chapter 4.2.7). In order to keep the imaging noise as low as possible, the atom numbers where counted for short times of flight such that the region of interest was kept at a minimum. The experiment was done both for absorption and fluorescence imaging. The details of the experiments will be discussed separately below.

6.1.1 Absorption Imaging

Our initial test was done with absorption imaging. The camera (Andor iXon DV887DCS-UV) used has a quantum efficiency $q = 0.32$ and a pixel size $d_{pix} = 16 \ \mu$m. The transmission through our imaging system, i.e. the fraction of light that hits the camera after passing through the mirrors, windows, and lenses, is experimentally
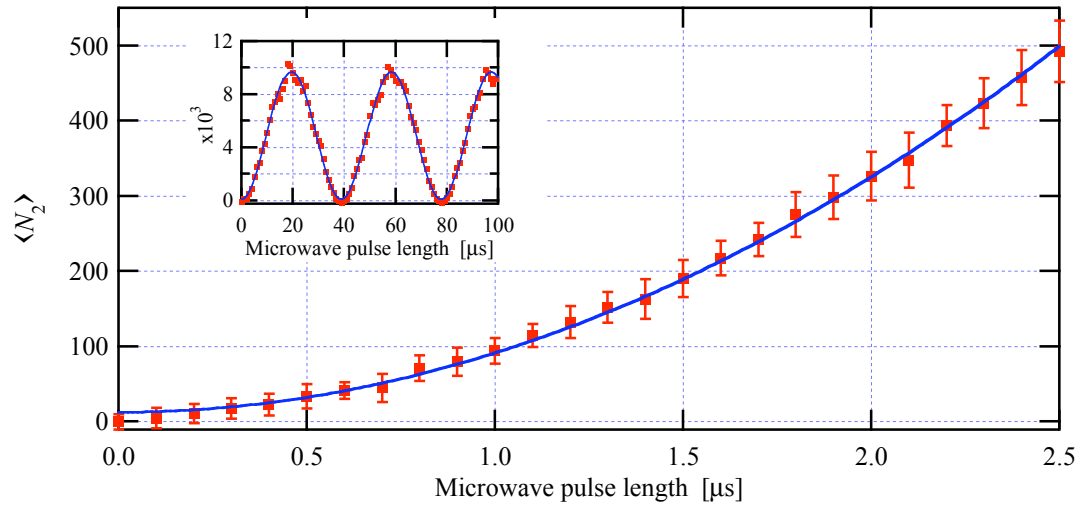
(a)
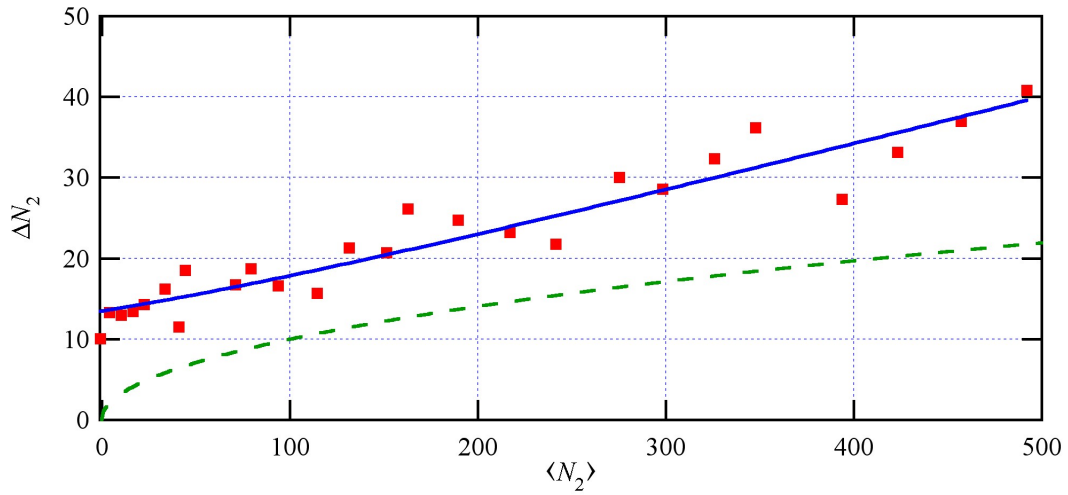
(b)

Figure 6.1: (a) Excitation of a small number of atoms from the $F = 1$ to the $F = 2$ hyperfine ground state using microwaves. The inset shows Rabi-flopping of the $F = 2$ atoms. For short microwave pulses we determine the average atom number and the corresponding fluctuations, which are, in this graph, indicated by the error bars. (b) The fluctuations are plotted versus the average number of atoms excited to the $F = 2$ state (red squares). The blue line is a fit to the expected noise and the green dashed line indicates the quantum projection noise as a function of the average number of atoms excited to the $F = 2$ state.

measured to be 0.88 and the magnification of our imaging system is 10×. Therefore the effective quantum efficiency is $q = 0.32 \times 0.88 = 0.28$ and the effective pixel area is $A_{pix} = 2.56~\mu\text{m}^2$. The experiment was done with a BEC with approximately $N = 12\,000$ atoms occupying 2 - 4 lattice sites. 12 ms before turning off the trap, a fraction of the atoms are transferred from the $|F = 1, m_F = 0\rangle$ state to the $|F = 2, m_F = 0\rangle$ state using microwaves. The number of atoms in the $F = 2$ state are imaged after a time of flight of 1 ms, such that the condensate is contained in a 20 x 20 pixel region of interest (ROI). For different microwave pulse lengths, the average number of atoms and the corresponding standard deviations are determined by repeating the experiment 20 times. The average number of atoms versus the length of the microwave pulse is shown in Figure 6.1(a), where the error bars indicate the experimental standard deviation. In Figure 6.1(b), the standard deviation is plotted as a function of the average atom number and the noise is fit to the expected noise form, in order to determine the noise floor of absorption imaging:

$$\Delta N_2 = \sqrt{\sigma_{\text{PSN}}^2 + \sigma_{\text{QPN}}^2 + \sigma_{\text{tech}}^2} \tag{6.7a}$$

$$= \sqrt{\sigma_{\text{PSN}}^2 + (1 - (N_2/N))N_2 + \beta^2 N_2^2}. \tag{6.7b}$$

The expected photon shot noise for a given average atom number is determined by summing the photon shot noise of each pixel, which is in turn computed from the average signal and reference images according to Equation 3.23. In this experiment, the expected photon shot noise is 11.2 atoms and varies by less than 0.1 % for the different atom numbers. The fit to the atom noise gives a photon shot noise $\sigma_{\text{PSN}} = 13.5 \pm 0.9$ atoms and technical fluctuations of 6.1%. The photon shot noise is in agreement with the expected value and the technical fluctuations agree with the observed experimental fluctuations of the total number of atoms in the BEC. A camera with an improved quantum efficiency q^* would reduce the photon shot noise according to $\sigma_{\text{PSN}}^* = \sqrt{q/q^*}\sigma_{\text{PSN}}$. After this experiment, we acquired a camera with $q^* = 0.98$.

83

If a condensate occupies a region 32 x 32 μm^2 large, the photon shot noise would be 7.7 atoms. Larger condensates require more expansion as they are otherwise too dense to be able to be counted properly. Generally, a minimum area of 100 x 100 μm^2 is required, which would have a photon shot noise of 24 atoms.

6.1.2 Fluorescence Imaging

We repeat the above experiment using fluorescence imaging with a better camera (Andor iKon DU934N-BR-DD) ($q = 0.98$ and $d_{pix} = 13$ μm) (see Figures 6.2 and 6.3). In fluorescence imaging the fundamental imaging limit is photon shot noise. However, the noise is in practice often limited by the readout noise of the camera.

The atoms are probed for 200 μs with $I_0 = 30I_{sat}^0$ so that the camera collects $a = 36.4$ photons per atom for atoms probed with a repump. Due to the large probe power and the fact that the polarization of the light is isotropic, 15% of the atoms in the $F = 2$ state that are probed without the repump are depumped to the $F = 1$ during the probe pulse. Once in the $F = 1$ state, the atoms remain dark, i.e. they no longer scatter the probe light. Consequently, the camera collects less photons for atoms in the $F = 2$ state that are probed without the repump, in other words $a_{\text{no\_repump}} = 27.3$ photons per atom. This value was determined in a separate experiment by comparing the number of photons counted when the atoms are probed with the repump to those probed without the repump. To reduce the readout noise, we bin the camera pixels 16 x 16. For a single pixel, the readout noise of the camera (8.3 electrons) corresponds to 0.23 atoms (0.30 atoms) per pixel, when the atoms are probed with (without) repump. For a ROI of 10 x 10 pixels corresponding to an area of 208 x 208 μm^2 (as used in the following experiment), the expected total readout noise is 2.3 atoms (3.0 atoms), which is over an order of magnitude less than the noise floor in absorption imaging for an equivalent ROI. As before, we start with a pure $|F = 1, m_F = 0\rangle$ and a smaller BEC with $N = 3\,800$ atoms in 1-2 lattice sites. The

(a)

(b)
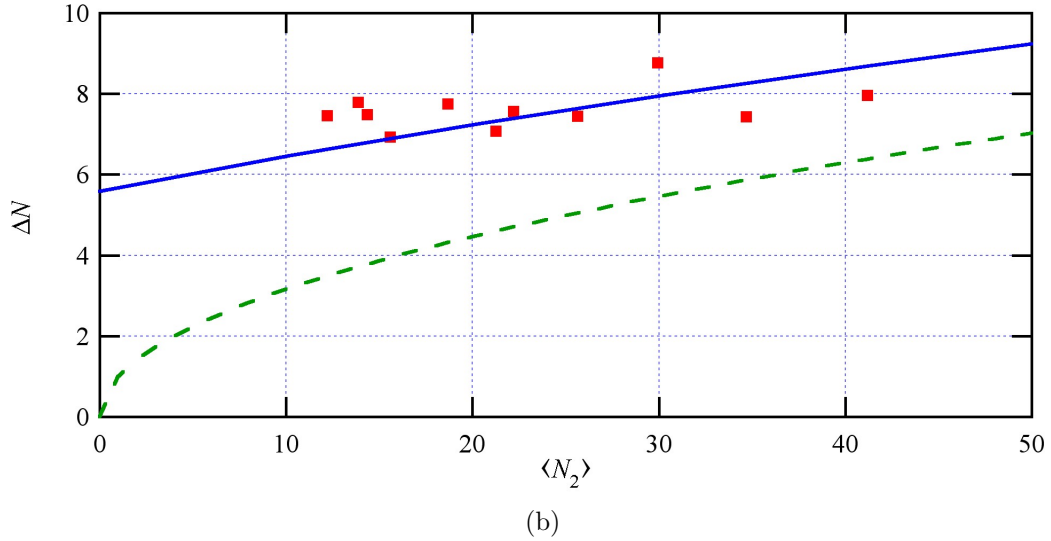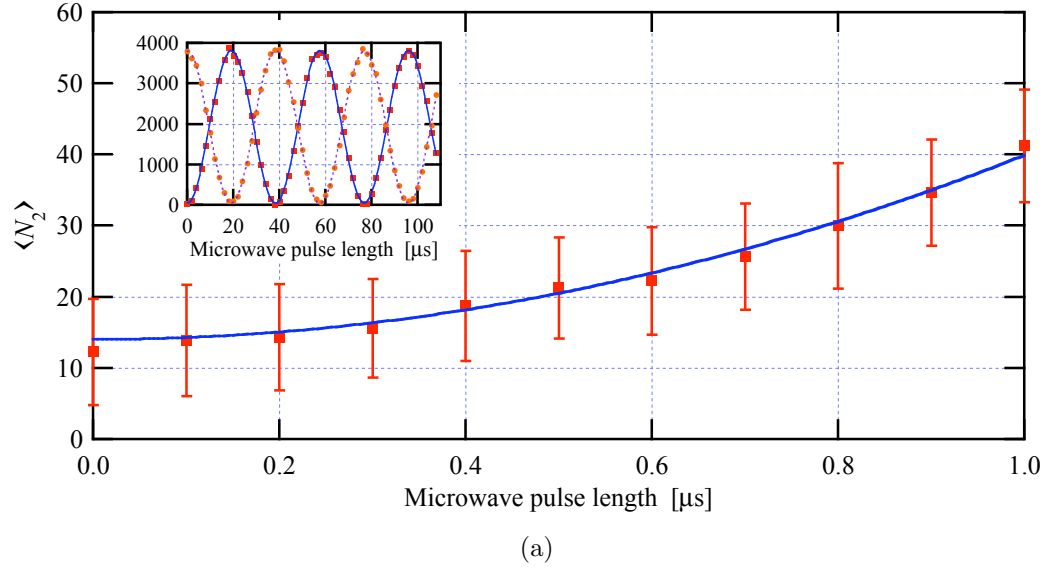
Figure 6.2: (a) Excitation of a small number of atoms from the $F = 1$ to the $F = 2$ hyperfine ground state using microwaves. The inset shows Rabi-flopping of both the $F = 1$ and $F = 2$ atoms. For short microwave pulses we determine the average atom number and the corresponding fluctuations, which are, in this graph, indicated by the error bars. (b) The fluctuations are plotted versus the average number of atoms excited to the $F = 2$ state (red squares). The blue line is a fit to the expected noise and the green dashed line indicates the quantum projection noise as a function of the average number of atoms excited to the $F = 2$ state.
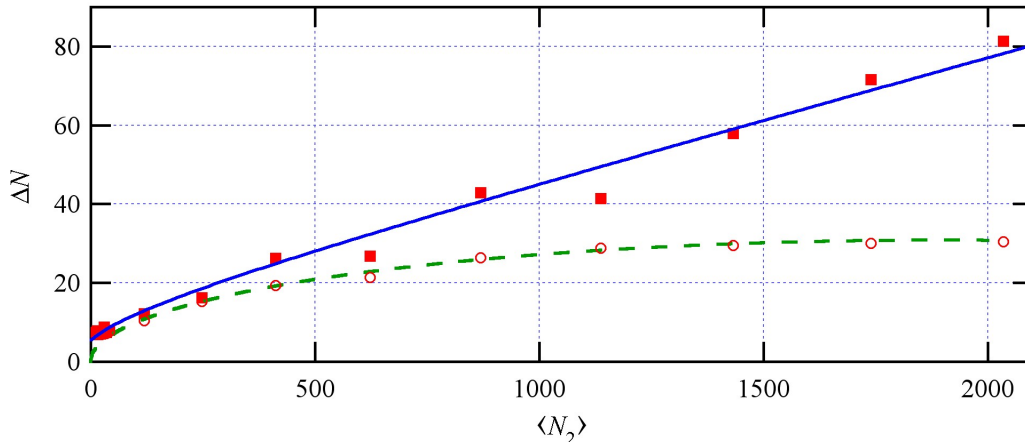
Figure 6.3: Quantum projection noise in a quantum state, which is in coherent superposition of the $|F = 1, m_F = 0\rangle$ and the $|F = 2, m_F = 0\rangle$ states after a microwave pulse. The fluctuations are plotted versus the average number in the $F = 2$ state (red sold squares). The data is fit to the expected noise and gives a technical noise of 3.5 %. As we also image the atoms in the $F = 1$ state, we can normalize the measurements of the atom in the $F = 2$ state to the total atom number and thus can eliminate technical noise (red open circles). The normalized data is for large atoms numbers, as expected, dominated by the quantum projection noise (green dashed line).

microwaves are pulsed on for 0.5 ms before the atoms are released from the trap.

In order to image both the atoms in the $F = 2$ state and the $F = 1$ state, we take two images in rapid succession, *i.e.* 2 ms apart. The $F = 2$ atoms are imaged after a time of flight of 3 ms without the repump and the $F = 1$ atoms are imaged after a time of flight of 5 ms with the repump. The time between the two imaging pulses is long enough for the atoms in the $F = 2$ state to disperse after being heated by the first imaging pulse, but is short enough to contain any potential diffraction of the remaining $F = 1$ BEC due to Bragg scattering from the first imaging pulse within the imaging ROI. The inset of Figure 6.2 shows a Rabi-flop between the two states. The fluctuations in atom number are determined for different microwave pulse lengths up to a π-pulse, by taking 100 data points for each setting. The trials with small atom numbers are shown in Figure 6.2 as rough comparison to the data taken with absorption imaging. The full range of data points is used to quantify the different

noise sources (see Figure 6.3).

Since we are also capable of counting the atom number in the $F = 1$ state, we can normalize the atom number in the $F = 2$ state to the total atom number of the condensate. This eliminates the technical noise of the experiment causing shot to shot fluctuations of the total atom number N. The normalized atom number in the $F = 2$ state is given by $N_2' = (\langle N \rangle / N) N_2$, where $\langle N \rangle$ is the average total number of atoms in the condensate and $N = N_1 + N_2$ is the total atom number of the current run. In Figure 6.3, the standard deviation is plotted as a function of the average atom for both the non-normalized and the normalized data. To quantify the different noise sources, we fit the data to the expected noise form for fluorescence imaging:

$$\Delta N_2 = \sqrt{\sigma_{\text{bkgscatter}}^2 + \sigma_{\text{RO}}^2 + + \sigma_{\text{PSN}}^2 + \sigma_{\text{QPN}}^2 + \sigma_{\text{tech}}^2} \qquad (6.8\text{a})$$

$$= \sqrt{\sigma_{\text{bkg}}^2 + ((1/a) + 1 - (N_2/N)) N_2 + \beta^2 N_2^2}, \qquad (6.8\text{b})$$

where the noise due to background scatter and the readout of the camera $\sigma_{\text{bkg}}^2 = \sigma_{\text{bkgscatt}}^2 + \sigma_{\text{RO}}^2$ can be considered to be constant and the photon shot noise of the atom signal is given by $\sigma_{\text{PSN}}^2 = (1/a)N_2$. The fit to the non-normalized data gives a background noise of 5.6 ± 1 atoms and a technical noise of $3.5\ \%$, which is equivalent to the observed fluctuations in the total atom number. Since the measured background noise is larger than the readout noise of the camera (≈ 3 atoms), there is a significant amount of background scatter corresponding to ≈ 5 atoms. As expected the normalized data follows the QPN curve closely indicating that the technical noise has been canceled out in the normalization process. Given this result, we can reliably count atom number with a standard deviation of about 6 atoms in an ROI with an area of 208 x 208 μm^2 and a probe time of 200 μs. This is a very remarkable result as not many experiments have been able to measure the atom numbers in a condensate with this low noise. Given these imaging parameters, we are able to measure the

atom shot noise of a condensate with $N = 36$ atoms. This is an exciting prospect because it would allow us to probe condensates for which the mean field approximation breaks down. Given our experimental conditions and imaging system, fluorescence imaging has the potential of lower imaging noise compared to absorption imaging, we therefore use fluorescence imaging to measure small atom numbers.

6.2 Calibration using QPN

In our experiment (described in more detail in Chapter 8) we investigate spin-mixing of a spin-1 BEC and therefore are interested in the QPN of a three level system. An atom in the $F = 1$ manifold constitutes a three level-system and can be described by the wave function:

$$\psi(t) = c_-(t)e^{-i\frac{E_- t}{\hbar}}|-\rangle + c_0(t)e^{-i\frac{E_0 t}{\hbar}}|0\rangle + c_+(t)e^{-i\frac{E_+ t}{\hbar}}|+\rangle, \qquad (6.9)$$

where $|-\rangle$, $|0\rangle$, and $|+\rangle$ represent the eigenfunctions of the Zeeman levels $m_F = -1$, $m_F = 0$, and $m_F = +1$, respectively, and E_-, E_0, and E_+ are the corresponding energy eigenvalues. In low magnetic fields, the energy difference between the $m_F = +1 \longleftrightarrow m_F = 0$ states and the $m_F = 0 \longleftrightarrow m_F = -1$ states is the same $E_- - E_0 = E_0 - E_+ = \hbar\omega = h \times 700$ Hz/mG. The variance in the measurement of the magnetization $M = N_+ - N_-$ for an ensemble of N independent spin-1 atoms is

$$(\Delta M)^2 = \sigma_+^2 + \sigma_-^2 + 2\sigma_{+-}^2 = \langle N_+ \rangle + \langle N_- \rangle - \langle N \rangle \left(p_- - p_+ \right)^2, \qquad (6.10)$$

where $\langle N_i \rangle$ is the average number of atoms in the quantum state $|i\rangle$ and $p_i = |c_i|^2$ is the probability of an atom to be in the quantum state $|i\rangle$. This QPN can be used to confirm the calibration of an imaging system by preparing the atoms in different well-defined superposition of the eigenstates $|i\rangle$.

Coherent superpositions of the three Zeeman levels of the $F = 1$ manifold can be created with radio-frequency (RF) transitions and a non-zero magnetic field is necessary to lift the degeneracy. For RF transitions the two two-level systems $m_F =$

$+1 \longleftrightarrow m_F = 0$ and $m_F = 0 \longleftrightarrow m_F = -1$ have the same Rabi frequency 2Ω and spontaneous decay can be neglected. To ensure a coherent superposition, it is necessary to start with a pure m_F state. Starting from a pure $m_F = 0$ and applying an RF-field of frequency ω_{RF}, the probability amplitudes $c_i(t)$ for the three Zeeman levels evolve, in the rotating-wave approximation, as:

$$c_\pm(t) = \left[\pm \frac{\Omega\Delta}{\Omega'^2} (1 - \cos(\Omega't)) + i \frac{\Omega}{\Omega'} \sin(\Omega't) \right] e^{\pm i \Delta t}, \tag{6.11a}$$

$$c_0(t) = \cos(\Omega't) + \left(\frac{\Delta}{\Omega} \right)^2 (1 - \cos(\Omega't)), \tag{6.11b}$$

where $\Delta = \omega_{RF} - \omega_0$ is the detuning from resonance and $\Omega' = \sqrt{\Delta^2 + 2\Omega^2}$. In this case, the probability to find the atom in the $m_F = -1$ state is always equal to the probability of finding the atom in the $m_F = +1$ state: $p_- = |c_-|^2 = p_+ = |c_+|^2$. For on resonance RF-pulses, the atoms will oscillate between the $m_F = 0$ state and the $m_F = \pm 1$ states (see Figure 6.4), and the corresponding probabilities are given by $p_0(t) = \cos^2(\Omega t)$ and $p_\pm(t) = \frac{1}{2} \sin^2(\Omega t)$. As a result, the variance in the magnetization $M = N_+ - N_-$ is given by:

$$(\Delta M)^2 = \langle N_+ \rangle + \langle N_- \rangle = \langle \tilde{N} \rangle = \langle N \rangle \sin^2(\Omega t), \tag{6.12}$$

with $\tilde{N} = N_+ + N_-$ and $N = N_+ + N_0 + N-$. Because the variance in the magnetization scales with the number of atoms in the $m_F = \pm 1$ states $(\tilde{N})$, the magnetization is said to have Poissonian fluctuations.

By applying RF-pulses of different lengths to a pure $m_F = 0$ condensate, we can control the number of atoms $\tilde{N}$ in the $m_F = \pm 1$ states and can exploit the $\tilde{N}$-scaling of the magnetization variance to calibrate the imaging system. In order to do the calibration, it is however necessary to consider other noise sources. As we are measuring the atom number difference between the $m_F = +1$ and the $m_F = -1$ states, fluctuations in the total atom number N due to technical noise in the experiment are to first order canceled out and can be ignored. Therefore we merely need to take into
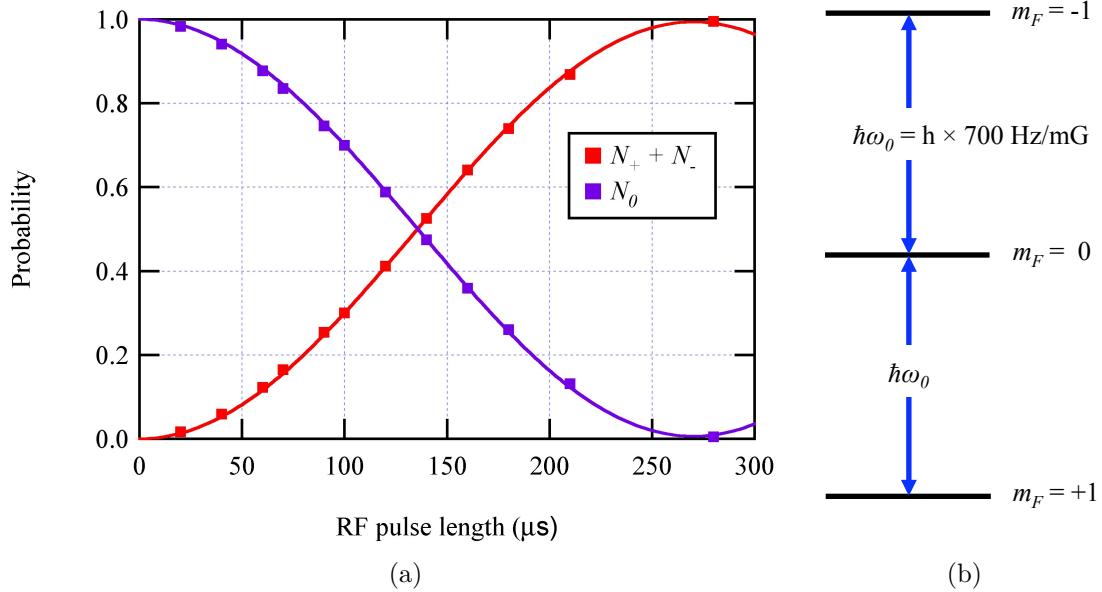
Figure 6.4: (a) A RF Rabi-flop starting from a pure $m_F = 0$ condensate. (b) Schematic of the Zeeman levels of the $F = 1$ hyperfine level. For small magnetic fields the splitting of the energy levels is $h \times 700$ Hz/mG.

account imaging noise. It is important to note that this calibration method is equally suited for absorption imaging.

For this calibration, we create a pure $|F = 1 \ m_F = 0\rangle$ condensate of about 4 000 atoms in a single lattice site. Next, we apply an resonant RF-pulse to create a coherent superposition of the three Zeeman levels as describe above, at a magnetic field of 430 mG. The condensate is probed after a free expansion of 7.5 ms using fluorescence imaging. We apply a Stern-Gerlach field during the first 4 ms of the expansion to separate the three spin components spatially. The condensate is probed for 100 μs and the resulting fluorescence signal is collected by a CCD camera. To ensure the spatial separation and therefore an independent detection of the three spin-components, we pulse on a Stern-Gerlach field during the first 4 ms of expansion.

The pixels of the camera are binned 16 x 16 in order to reduce the readout noise and the region of interest (ROI) of a spin component is 14 x 10 super-pixels. The fluctuations of the magnetization are measured as a function of the atom number $\langle \tilde{N} \rangle$
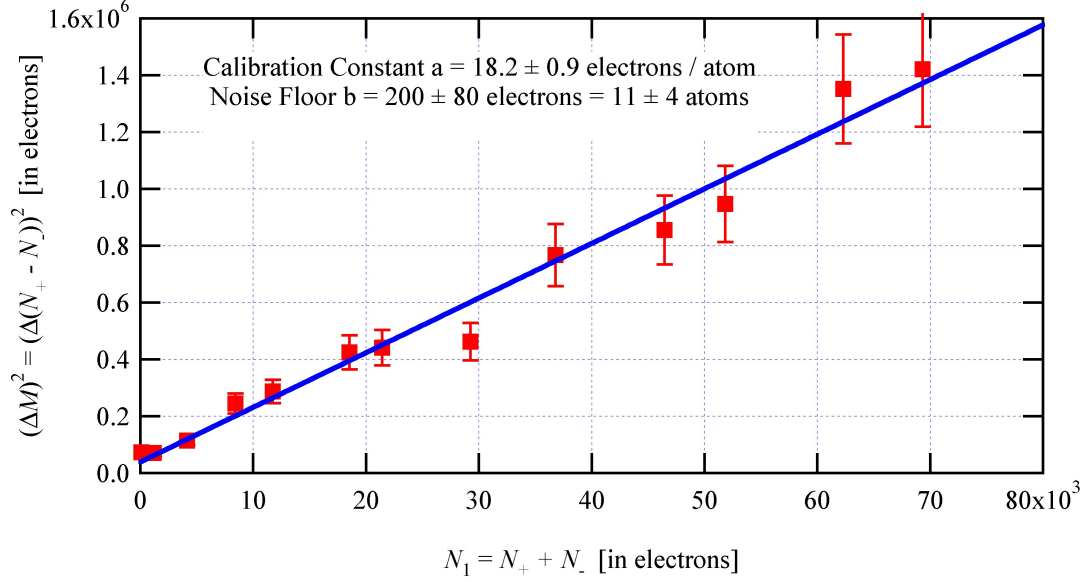
Figure 6.5: Calibration of the imaging system using quantum projection noise.

by taking 100 data points for various RF-pulse lengths. The data shown in Figure 6.5 is taken in terms of electrons counted by the camera. In order to extract the calibration constant a, which converts the number of electrons counted to number of atoms, the data is fit to the total expected noise

$$\left(\Delta M^{e^-}\right)^2 = \sigma^2_{\text{bkg}} + \sigma^2_{\text{PSN}} + \sigma^2_{\text{QPN}} \tag{6.13a}$$

$$= b^2 + (1+a)\langle \tilde{N}^{e^-}\rangle, \tag{6.13b}$$

where $\sigma^2_{bkg} = \sigma^2_{\text{RO}} + \sigma^2_{\text{BkgScatt}} = b^2$ is the constant noise due to the readout process of the camera and the photon shot noise of the background scatter, $\sigma^2_{PSN} = \langle \tilde{N}_{e^-}\rangle$ is the photon shot noise of the atom signal, and $\sigma^2_{QPN} = \langle \tilde{N}\rangle = a\langle \tilde{N}_{e^-}\rangle$ is the quantum projection noise associated with the prepared quantum state. The calibration factor is $a = 18.2\pm0.9$ electrons/atom and the noise floor is $b = 11\pm4$ atoms, and the errors given are one standard deviation. Since the readout noise of the camera is 7.6 atoms, the background scatter is approximately 8 atoms and therefore is currently limiting the noise floor of our imaging system. It is important to note that the noise values quoted above are for an ROI twice the size of that used for imaging a single spin

91

component. For an ROI of a single spin component with N atoms the detection noise is

$$\sigma^2 = \left((7.8)^2 + \frac{N}{18.2} \right) \text{ atoms}^2. \tag{6.14}$$

Consequently, for approximately $N > 65$ the atom shot noise is larger than the detection noise.

In summary, we have created small condensates (< 100 atoms) in the $F = 2$ hyperfine state by transferring a fraction of the total condensate from the $F = 1$ hyperfine ground state to the $F = 2$ hyperfine ground state using microwaves. In both absorption and fluorescence imaging, we have detected small condensates with a noise floor of ≈ 10 atoms. The fluctuations in the atom number fit the expected noise curves given imaging noise, quantum projection noise, and fluctuations in the total atom number due to experimental noise and therefore demonstrate a thorough understanding of the noise. By re-normalizing the atoms in the $F = 2$ state to the total atom number, we have been able to measure the number of atoms at the standard quantum limit. In a second experiment, we create super-positions in the Zeeman levels of the $F = 1$ hyperfine ground state using RF-radiation. The resulting quantum projection noise is used to calibrate the imaging system. This new method of calibration is very reliable and powerful as it requires no knowledge of the imaging parameters, such as probe time, probe power, quantum efficiency, etc. In conclusion, we have tested our imaging system and now have the necessary tool to observe sub-Poissonian spin statistics in a spin-1 condensate.

CHAPTER VII

SPIN-1 CONDENSATE THEORY

Bose-Einstein condensates of alkali-metal atoms, such as ^{23}Na and ^{87}Rb, have internal degrees of freedom due to their hyperfine spin structure. These internal spin degrees of freedom are frozen in magnetic traps and thus experiments in this type of trap mostly involve only one spin component. In far-off resonant optical traps, however, the spin degrees of freedom are made accessible. Thus optical traps allow the study of multi-spin-component BECs, called spinor condensates. Because of these internal degrees of freedom, the dynamics in spinor condensates are not restricted to the motional degrees of freedom and therefore exhibit richer quantum structure and quantum dynamics.

In this chapter, we will describe the interactions in a spin $f = 1$ condensate composed of three spin components $m_f = 0, \pm 1$. The theoretical description of this system follows closely the presentations given in [93, 94, 95]. The system of interest, a trapped spinor condensate in an external magnetic field is described by the Hamiltonian

$$H = \sum_{i=1}^{N} \left[\frac{p_i^2}{2M} + V_{trap}(\vec{r_i}) + E_i \right] + \frac{1}{2} \sum_{i=1}^{N} V_{int}. \tag{7.1}$$

The number of atoms in the condensate is given by N, and the mass of the atoms is given by M. Since the trap is a far-off resonant optical trap, the trapping potential V_{trap} can be assumed to be the same for all spin components [93]. E_i is the Zeeman shift due to a uniform external magnetic field $\vec{B}$ on the hyperfine structure of the atom, and V_{int} is the interaction between two atoms.
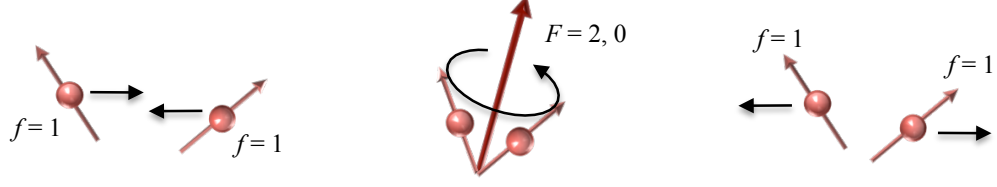
Figure 7.1: Intuitive picture of a binary collision of two spin-1 bosons. (Left) Two spin-1 bosons approach each other. (Center) the atomic spin of two bosons coupled to form a total spin. During this collision, they precess around this total spin, which can be $F = 0, 2$. (Right) After the collision, the two bosons break apart into two spin-1 bosons.

7.1   Microscopic Picture

Inside a spin-f condensate, the different spin components $(m_f = -f, -f+1, \dots, f)$ interact with each other through spin exchange collisions. These ultracold atomic interactions are dominated by two-body s-wave collisions and can be pictured as in Figure (Fig1). As two atoms approach each other, their spins ($|f_1 = f, \, m_{f1}\rangle$ and $|f_2 = f, \, m_{f2}\rangle$) interact and temporarily couple to form the total hyperfine spin state $|F, \, m_F\rangle$. During this collision the two spins precess around the total spin $\vec{F} = \vec{f_1} + \vec{f_2}$, whose allowed values are $F = 2f, 2f-1, \dots, 0$. Due to symmetry requirements on identical bosons, however, only the $F = even$ channels are permitted, as the spatial wavefunction of the two bosonic atoms is assumed to be symmetric. After the collision, the two atoms decouple and break apart with spins ($|f_1' = f, \, m_1'\rangle$ and $|f_2' = f, \, m_2'\rangle$), while the total angular momentum $m_F = m_{f1} + m_{f2} = m'_{f1} + m'_{f2}$ is conserved during the collision process. Using this two-body interaction model, the spin interaction term can be written as a sum of contributions from the different total spin F channels. For $f = 1$, it is:

$$V_{int}(\vec{r_1} - \vec{r_2}) = \delta(\vec{r_1} - \vec{r_2}) \sum_{F=0}^{2} g_F \sum_{m_F=-F}^{F} |F, \, m_F\rangle \langle F, \, m_F| \tag{7.2}$$

The coupling strength is $g_F = \frac{4\pi\hbar^2}{M} a_F$, where a_F is the s-wave scattering length for the total spin-F channel, and M is the atomic mass. Keeping in mind the symmetry

requirement for bosons and using the closure relationship

$$\sum_{F=0}^{2} \sum_{m_F=-F}^{F} |F, \, m_F\rangle \, \langle F, \, m_F| = 1, \tag{7.3}$$

in conjuction with the identity $2\vec{f_1} \cdot \vec{f_2} = \vec{F}^2 - \vec{f_1}^2 - \vec{f_2}^2$, the spin interaction term can be rewritten as:

$$V_{int}(\vec{r_1} - \vec{r_2}) = \delta(\vec{r_1} - \vec{r_2}) \left[c_0 + c_2 \vec{f_1} \cdot \vec{f_2} \right], \tag{7.4}$$

where c_0 and c_2 correspond to density- and spin-dependent interactions respectively and are given by

$$c_0 = \frac{g_0 + 2g_2}{3} = \frac{4\pi\hbar^2}{M} \bar{a} \tag{7.5}$$

and

$$c_2 = \frac{g_2 - g_0}{3} = \frac{4\pi\hbar^2}{M} \frac{\Delta a}{3}. \tag{7.6}$$

In the above expression $\bar{a} = (a_{F=0} + 2a_{F=2})/3$ is the mean s-wave scattering length, and $\Delta = (a_{F=0} - a_{F=2})$ is the scattering length difference. The spin-dependent interaction c_2 couples the different Zeeman states, which leads to spinor dynamics, such as spin-mixing and spin domain formation. The sign of c_2 determines the ground state structure of the atoms. For $c_2 < 0$, the spin-dependent interaction potential is minimized for a maximum $\vec{f_1} \cdot \vec{f_2}$. This is achieved when the spinors are all polarized in the same direction, and therefore an atom with $c_2 < 0$ is said to be ferromagnetic. In contrast, the ground state of an atom with $c_2 > 0$ requires the spinors to align in opposite directions. As a result, atoms with $c_2 > 0$ are said to be anti-ferromagnetic.

7.2 Zeeman Energy Shifts

Since external magnetic fields can influence or even dominate the internal spin interactions, it is important to study the behavior of a spinor condensate in an external magnetic field. Here, we will consider a static uniform magnetic field assumed $\hat{z}$-axis. The Zeeman effect of a uniform external magnetic field $\vec{B}$ on the hyperfine structure

95

is $V_B = H_{hf} - (g_J \vec{\mu_0} + g_I \vec{\mu_N}) \cdot \vec{B}$, where H_{hf} is the hyperfine interaction, g_J is the Lande g-factor for a valence electron with total angular momentum $\vec{J}$, μ_0 is the Bohr magneton, g_I is the Lande g-factor for an atom with total angular momentum $\vec{I}$, and μ_N is the nuclear magneton. The Zeeman shifts due to this field are

$$E_\pm = -\frac{E_{hfs}}{8} \mp g_I \mu_N B - \frac{1}{2} E_{hfs} \sqrt{1 \pm \alpha + \alpha^2}, \tag{7.7a}$$

$$E_0 = -\frac{E_{hfs}}{8} - \frac{1}{2} E_{hfs} \sqrt{1 + \alpha^2}, \tag{7.7b}$$

where $\alpha = (g_I \mu_N B + g_J \mu_0 B)/E_{hfs}$ [60].

7.3 Second Quantized Hamilton

Given the two-body spin interaction model described above (7.4), the Hamiltonian of a spin-1 condensate in an external field is

$$H = \sum_{i=1}^{N} \left[\frac{p_i^2}{2M} + V_{trap}(\vec{r_i}) + E_i \right] + \frac{1}{2} \sum_{i=1}^{N} \delta(\vec{r_1} - \vec{r_2}) \left[c_0 + c_2 \vec{f_1} \cdot \vec{f_2} \right]. \tag{7.8}$$

In the second quantization formalism, the Hamiltonian is

$$H = \sum_{\sigma'} \int d\vec{r'} \, \hat{\Psi}_{\sigma'}^\dagger(\vec{r'}) \left(-\frac{\nabla^2}{2M} + V_{trap} + E_{\sigma'} \right) \hat{\Psi}_{\sigma'}(\vec{r'}) +$$

$$\sum_{\sigma',\sigma'',\sigma''',\sigma''''} \int d\vec{r'} \, \hat{\Psi}_{\sigma'}^\dagger(\vec{r'}) \hat{\Psi}_{\sigma''}^\dagger(\vec{r'}) \langle \sigma', \sigma'' | c_0 + c_2 \vec{f_1} \cdot \vec{f_2} | \sigma'''', \sigma''' \rangle \hat{\Psi}_{\sigma'''}(\vec{r'}) \hat{\Psi}_{\sigma''''}(\vec{r'}),$$

$$\tag{7.9}$$

where $\hat{\Psi}_\sigma(\vec{r})$ $(\hat{\Psi}_\sigma^\dagger(\vec{r}))$ is the atomic field annihilation (creation) operator associated with the hyperfine spin state $|f = 1, m_f = \sigma\rangle$ at location $\vec{r}$,

$$\langle \sigma', \sigma'' | c_0 + c_2 \vec{f_1} \cdot \vec{f_2} | \sigma'''', \sigma''' \rangle =$$

$$\langle f_1 = 1, m_{f1} = \sigma'; f_2 = 1, m_{f2} = \sigma'' | c_0 + c_2 \vec{f_1} \cdot \vec{f_2} | f_1 = 1, m_{f1} = \sigma''''; f_2 = 1, m_{f2} = \sigma''' \rangle,$$

and the summation indices $\sigma', \sigma'', \sigma'''\sigma''''$ run through the values $(-1, 0, 1)$. Since we are interested in the spin-dependent interactions, we re-write the Hamiltonian as a sum of a spin-independent part H_n and spin dependent part H_s:

$$H = H_n + H_s, \tag{7.10}$$

where

$$H_n = \sum_{\sigma'} \int d\vec{r'}\ \hat{\Psi}_{\sigma'}^{\dagger} H_0 \hat{\Psi}_{\sigma'} + \frac{c_0}{2} \sum_{\sigma',\sigma''} \int d\vec{r'}\ \hat{\Psi}_{\sigma'}^{\dagger} \hat{\Psi}_{\sigma''}^{\dagger} \hat{\Psi}_{\sigma'} \hat{\Psi}_{\sigma''}, \tag{7.11}$$

with $H_0 = -\left(\hbar^2/2M\right)\nabla^2 + V_{trap}$, and where

$$H_s = \sum_{\sigma'} \int d\vec{r'}\ \hat{\Psi}_{\sigma'}^{\dagger}(\vec{r'})\left(E_{\sigma'}\right)\hat{\Psi}_{\sigma'}(\vec{r'}) +$$

$$\sum_{\sigma',\sigma'',\sigma''',\sigma''''} \int d\vec{r'}\ \hat{\Psi}_{\sigma'}^{\dagger}(\vec{r'})\hat{\Psi}_{\sigma''}^{\dagger}(\vec{r'}) \langle \sigma',\ \sigma''| c_2 \vec{f_1}\cdot\vec{f_2}|\sigma'''',\ \sigma''' \rangle \hat{\Psi}_{\sigma'''}(\vec{r'})\hat{\Psi}_{\sigma''''}(\vec{r'}). \tag{7.12}$$

Furthermore, we can express the spin-dependent Hamiltonian H_s in terms of the explicit individual spin components

$$H_s = E_1 \int d\vec{r'}\ \hat{\Psi}_1^{\dagger}\hat{\Psi}_1 + E_0 \int d\vec{r'}\ \hat{\Psi}_0^{\dagger}\hat{\Psi}_0 + E_{-1} \int d\vec{r'}\ \hat{\Psi}_{-1}^{\dagger}\hat{\Psi}_{-1}$$

$$+ \frac{c_2}{2} \int d\vec{r'}\ \hat{\Psi}_1^{\dagger}\hat{\Psi}_1^{\dagger}\hat{\Psi}_1\hat{\Psi}_1\ +\ \hat{\Psi}_{-1}^{\dagger}\hat{\Psi}_{-1}^{\dagger}\hat{\Psi}_{-1}\hat{\Psi}_{-1}\ +\ 2\hat{\Psi}_1^{\dagger}\hat{\Psi}_0^{\dagger}\hat{\Psi}_1\hat{\Psi}_0\ +\ 2\hat{\Psi}_{-1}^{\dagger}\hat{\Psi}_0^{\dagger}\hat{\Psi}_{-1}\hat{\Psi}_0$$

$$-\ 2\hat{\Psi}_1^{\dagger}\hat{\Psi}_{-1}^{\dagger}\hat{\Psi}_1\hat{\Psi}_{-1}\ +\ 2\hat{\Psi}_0^{\dagger}\hat{\Psi}_0^{\dagger}\hat{\Psi}_1\hat{\Psi}_{-1}\ +\ 2\hat{\Psi}_1^{\dagger}\hat{\Psi}_{-1}^{\dagger}\hat{\Psi}_0\hat{\Psi}_0. \tag{7.13}$$

In order to obtain the time evolution of the field operators, we use the Heisenberg equation of motion

$$i\hbar \frac{d\hat{\Psi}_i(\vec{r},\ t)}{dt} = \left[\hat{\Psi}_i(\vec{r},\ t),\ H\right], i = (1, 0, -1). \tag{7.14}$$

Substituting the Hamiltonian $H = H_n + H_s$, and applying the commutation relations for bosonic field operators, we get

$$i\hbar \frac{\hat{\Psi}_{\pm}(t)}{dt} = H_0 \hat{\Psi}_{\pm}\ +\ c_0 \left(\hat{\Psi}_{\pm}^{\dagger}\hat{\Psi}_{\pm}\ +\ \hat{\Psi}_0^{\dagger}\hat{\Psi}_0\ +\ \hat{\Psi}_{\mp}^{\dagger}\hat{\Psi}_{\mp}\right)\hat{\Psi}_{\pm}\ +$$

$$E_{\pm}\hat{\Psi}_{\pm}\ +\ c_2 \left[\left(\hat{\Psi}_{\pm}^{\dagger}\hat{\Psi}_{\pm}\ +\ \hat{\Psi}_0^{\dagger}\hat{\Psi}_0\ -\ \hat{\Psi}_{\mp}^{\dagger}\hat{\Psi}_{\mp}\right)\hat{\Psi}_{\pm}\ +\ \hat{\Psi}_{\mp}^{\dagger}\hat{\Psi}_0^2\right], \tag{7.15a}$$

$$i\hbar \frac{\hat{\Psi}_0(t)}{dt} = H_0 \hat{\Psi}_0\ +\ c_0 \left(\hat{\Psi}_{\pm}^{\dagger}\hat{\Psi}_{\pm}\ +\ \hat{\Psi}_0^{\dagger}\hat{\Psi}_0\ +\ \hat{\Psi}_{\mp}^{\dagger}\hat{\Psi}_{\mp}\right)\hat{\Psi}_0\ +$$

$$E_0\hat{\Psi}_0\ +\ c_2 \left[\left(\hat{\Psi}_{+}^{\dagger}\hat{\Psi}_{+}\ +\ \hat{\Psi}_{-}^{\dagger}\hat{\Psi}_{-}\right)\hat{\Psi}_0\ +\ 2\hat{\Psi}_{+}\hat{\Psi}_{-}\hat{\Psi}_0^{\dagger}\right], \tag{7.15b}$$

keeping in mind that $\hat{\Psi}_i^\dagger \hat{\Psi}_i = \hat{N}_i$ is the number operator for the spin component in the hyperfine state $|f = 1, \, m_f = i\rangle$ (hereafter refered to as spin i component). For large condensates ($N >> 1$) at near-zero temperatures, quantum fluctuations can be ignored and in this case the condensate is essentially described by the mean field $\psi_i = \left\langle \hat{\Psi}_i \right\rangle$, which gives rise to the Gross-Pitaevskii (GP) equations (7.16) discussed below.

7.4 Gross-Pitaevskii Equations for a spin-1 BEC

The following three coupled GP Equations govern the dynamics of spin-1 condensates in the mean field limit (at near-zero temperature) , where the ground state is macroscopically occupied and the three spinor operators can be approximated by a 3-dimensional vector order parameter.

$$i\hbar \frac{\partial \psi_0}{\partial t} = h_0 \psi_0 + c_0 n \psi_0 + E_0 \psi_0 + c_2(n_+ + n_-)\psi_0 + 2c_2 \psi_0^* \psi_+ \psi_- \qquad (7.16a)$$

$$i\hbar \frac{\partial \psi_\pm}{\partial t} = h_0 \psi_\pm + c_0 n \psi_\pm + E_\pm \psi_\pm + c_2(n_0 \pm (n_+ - n_-))\psi_\pm + c_2 \psi_0^2 \psi_\mp^* \qquad (7.16b)$$

where $h_0 = \frac{-\hbar^2 \nabla^2}{2m} + V$, E_i the Zeeman energy of the spin state i in a uniform static B field (7.7), $n = n_+ + n_0 + n_-$ is the total density, and $n_i = |\psi_i|^2$ is the density for the spin i component ($i = 0, \pm$).

7.5 Single Mode Approximation

In the single-mode approximation (SMA), the wave functions ψ_i ($i = 0, \pm$) share the same spatial mode. This is valid when the spin-dependent interaction (proportional to $|c_2|$) is negligible compared to the density-dependent interaction (proportional to $|c_0|$), and we can therefore assume the spatial mode function $\phi(\vec{r})$ is determined by the the spin-independent part of the Hamiltonian, namely $H_n = \frac{-\hbar^2 \nabla^2}{2m} + V + c_0 n$, with $H_n \phi = \mu \phi$. We thus make the substition (SMA)

$$\psi_i \xrightarrow{\text{SMA}} \sqrt{N} \phi(\vec{r}) e^{-i\mu t/\hbar} \xi_i(t) \, , \quad i = 0, \pm \, , \qquad (7.17)$$

where N is the total number of atoms, $\phi(\vec{r})$ is the common spatial mode function, μ is the chemical potential, and ξ_i is the internal spin state i satisfying $|\xi_+|^2 + |\xi_0|^2 + |\xi_-|^2 = 1$. We can now rewrite the GP equations (7.16) in terms of the ξ_i's by applying the SMA (7.17) and eliminating the spatial dynamics through $H_n\phi = \mu\phi$. The calculation is only shown in more detail for the spin state $i = 0$, that is for equation (7.16a), since the other two are obtained through the same procedure. After the substitution and canceling a factor $\sqrt{N}e^{-i\mu t/\hbar}$ on each side of the equation we get:

$$i\hbar\left(-\frac{i\mu}{\hbar}\xi_0 + \dot{\xi}_0\right)\phi = \xi_0(H_s + E_0)\phi + c_2N|\phi|^2\phi(|\xi_+|^2 + |\xi_-|^2) + 2c_2N|\phi|^2\phi\xi_0^*\xi_+\xi_- \ .$$

The relation $H_s\phi = \mu\phi$ allows the cancellation of the first term on each side of the above equation. We then multiply both sides by ϕ^* and integrate over $\vec{r}$, using the normalization of ϕ: $\int |\phi|^2 = 1$, and setting $c = c_2N\int |\phi|^4$ and $\rho_i = |\xi_i|$, to get:

$$i\hbar\dot{\xi}_0 = E_0\xi_0 + c(\rho_+ + \rho_-) + 2c\xi_0^*\xi_+\xi_- \ . \tag{7.18}$$

Similarly, substituting (7.17) into equation (7.16b) leads to:

$$i\hbar\dot{\xi}_\pm = E_\pm\xi_\pm + c(\rho_0 \pm (\rho_+ - \rho_-)) + c\xi_0^2\xi_\mp^* \ . \tag{7.19}$$

The total number of atoms $\rho_0 + \rho_+ + \rho_- = 1$ and the atomic magnetization $\rho_+ - \rho_- = m = (N_+ - N_-)/N$ are conserved and are therefore constants of the motion. Solving the two conservation equations for $\rho_\pm$ gives

$$\rho_\pm = \frac{1 - \rho_0 \pm m}{2} \ . \tag{7.20}$$

Using this identity, we can rewrite equations (7.18) and (7.19) in terms of ρ_0 only:

$$i\hbar\dot{\xi}_0 = E_0\xi_0 + c(1 - \rho_0) + 2c\xi_0^*\xi_+\xi_- \ , \tag{7.21a}$$

$$i\hbar\dot{\xi}_\pm = E_\pm\xi_\pm + c(\rho_0 \pm m) + c\xi_0^2\xi_\mp^* \ . \tag{7.21b}$$

In order to eliminate the E_i dependence and to simplify the coupled equations (7.21), we introduce a phase factor (recall $\rho_i = |\xi_i|^2$) and rewrite the ξ_i's as

$$\xi_\pm(t) = \sqrt{\rho_\pm}e^{-i\theta_\pm(t)}e^{-i(E_0\mp\eta)t/\hbar} \quad \text{and} \quad \xi_0(t) = \sqrt{\rho_0}e^{-i\theta_0(t)}e^{-iE_0t/\hbar}, \tag{7.22}$$

where $\eta = (E_+ - E_-)/2$ represents the linear Zeeman shift. Applying the requirement that the total number of atom is conserved, the equations (7.21b) can be written in terms of ρ_0 and the relative phase $\theta = \theta_+ + \theta_- - 2\theta_0$:

$$\dot{\rho}_0 = -\frac{2c}{\hbar}\rho_0\sqrt{(1-\rho_0)^2 - m^2}\sin\theta, \tag{7.23}$$

$$\dot{\theta} = -\frac{2\delta}{\hbar} + \frac{2c}{\hbar}(1-2\rho_0) + \frac{2c}{\hbar}\frac{(1-\rho_0)(1-2\rho_0) - m}{\sqrt{(1-\rho_0)^2 - m^2}}\cos\theta, \tag{7.24}$$

where $\delta = (E_+ - E_- 2E_0)/2$ is the quadratic Zeeman effect. The transformations (7.22) together with atom number and magnetization conservation allow us to reduce the three coupled GP-type equations ((7.18), (7.19)), describing the spinor dynamics, to two ((7.23), (7.24)). Classically, these equations describe the dynamics of a system governed by the energy functional (or Hamiltonian)

$$\mathcal{E} = c\rho_0\left(1 - \rho_0 + \sqrt{(1-\rho_0)^2 - m^2}\cos\theta\right) + \delta(1-\rho_0) \tag{7.25}$$

as they satisfy the relations $\dot{\rho}_0 = -(2/\hbar)\delta\mathcal{E}/\delta\theta$ and $\dot{\theta}_0 = (2/\hbar)\delta\mathcal{E}/\delta\rho_0$. In this simple classical analogy, $\mathcal{E}$ describes a non-rigid pendulum. Consequently, the spinor dynamics described by the two coupled non-linear differential equations above ((7.23) and (7.24)) are equivalent to those of a classical non-rigid pendulum. Since energy dissipation is not included in our model, $\mathcal{E}$ is a constant of motion and thus the phase-space trajectories are confined to equal energy contours. Examples for such energy contours for $m = 0$ are given in Fig. 2. Note that the sign of c_2 determines the ground state of a spinor condensate. In the ferromagnetic case $(c_2 < 0)$, the spinor phase for the ground state vanishes $\theta = 0$, whereas in the anti-ferromagnetic case $(c_2 > 0)$ it is given by $\theta = \pi$.
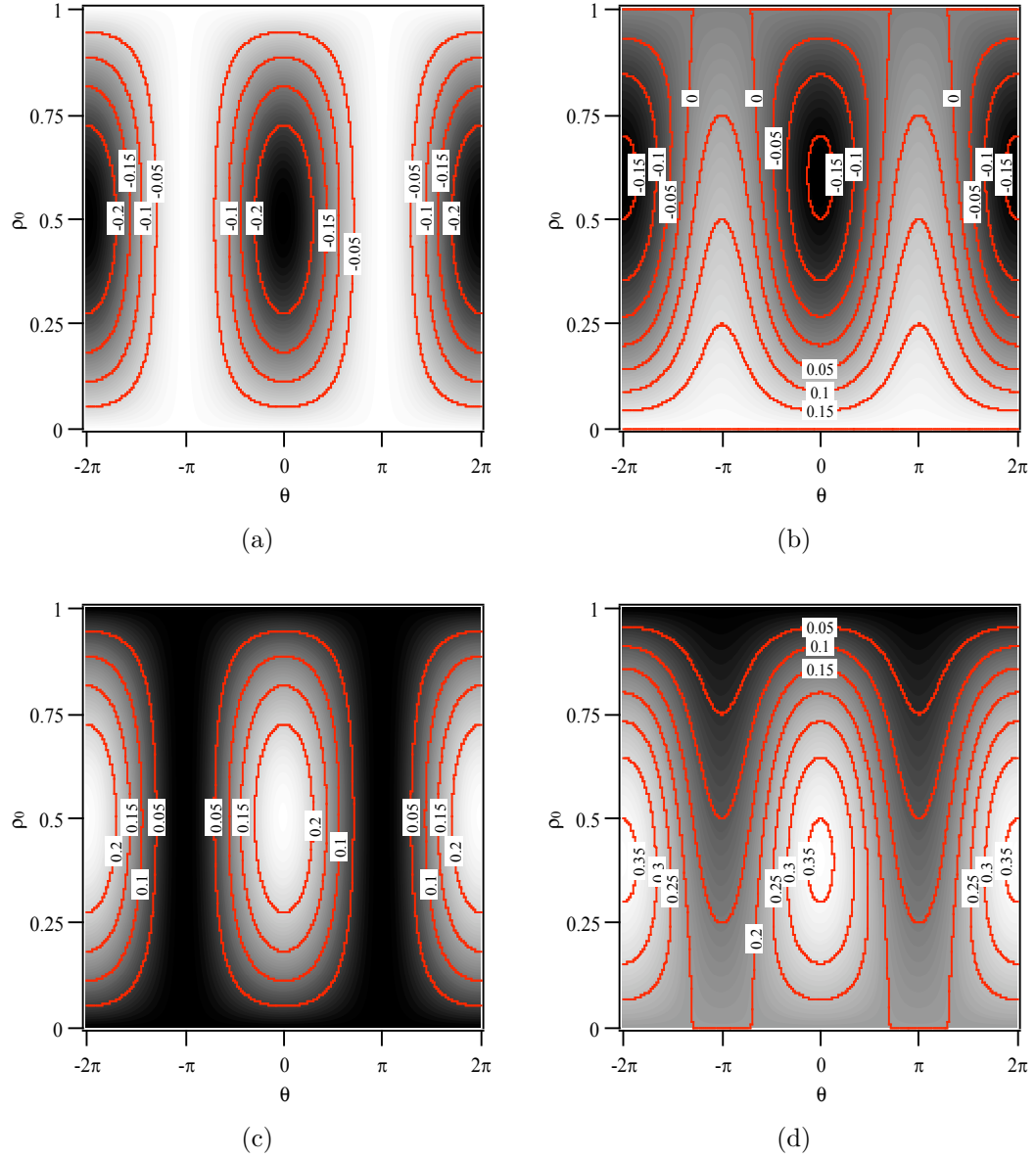
Figure 7.2: Energy contours for a spinor condensate with total magnetization $m = 0$, where ρ_0 is the fractional population of the $F = 1 m_F = 0$ state, and θ is the relative spinor phase. The energy per particle is in units of the spinor interaction $2|c_2|n$ and the darker regions represent lower energy. (a) and (b) Energy contours for ferromagnetic spinors ($c_2 < 0$). (c) and (d) Energy contours for anti-ferromagnetic spinors ($c_2 > 0$). (a) and (c) $q = 0$. (b) and (d) $q = 0.2 \times 2|c_2|n$.

CHAPTER VIII

SUB-POISSONIAN FLUCTUATIONS IN A SPINOR BEC

In the field of atom optics there recently has been much interest in the quantum properties of matter waves, in particular quantum correlations and entanglement. In analogy to quantum optics one could consider this the emergence of the field of quantum atom optics. The creation of non-classical squeezed states is a major focus in both quantum optics [40] and quantum atom optics. These states not only test the fundamentals for quantum mechanics but also have applications in quantum information and have the potential to improve sensitivity in interferometers. In optics, correlated photon pairs or squeezed states can be generated using optical processes such as four-wave mixing or parametric down-conversion. Matter wave analogues of these processes have been demonstrated in atomic collisions [52, 15] and molecular disassociation [14]. In these systems, the atom-atom interactions play the role of the nonlinear medium that allow the conversion processes.

In a $F = 1$ spinor condensate, the spin-spin interaction represents a type of four-wave mixing of the internal states of the matter wave. The spin-mixing term in the spin-dependent Hamiltonian allows coherent spin-changing collisions between two $m_F = 0$ atoms and a pair of $m_F = \pm 1$ atoms:

$$2 \left| m_F = 0 \right\rangle \leftrightharpoons \left| m_F = -1 \right\rangle + \left| m_F = +1 \right\rangle. \tag{8.1}$$

In previous work done in our lab [96], the coherence and reversibility of the spin-changing collisions was demonstrated. In this experiment, the third spin state ($m_F = +1$) is generated in a condensate, which initially only occupies the other two spin states, $m_F = 0$ and $m_F = -1$. This process is equivalent to degenerate four-wave mixing.

In the experiment described in this chapter, we investigate the production of $m_F = \pm 1$ atom pairs from a pure $m_F = 0$ condensate. This process can be interpreted as a matter-wave analogue of parametric down-conversion, which creates entanglement between photons with different polarization. Alternatively, the generation of pair correlation can be seen as the result of elastic spin-changing collisions between pairs of $m_F = 0$ atoms, which are constrained by the conservation of angular momentum, *i.e.* of the magnetization. Indeed, spin-mixing from a pure $m_F = 0$ condensate has been predicted to generate quantum entanglement and spin-squeezing [41, 42, 97] and therefore is an intriguing quantum system with potential applications in measurements of the magnetic field below the standard quantum limit [55].

Here, we report on the measurement of relative number squeezing between the atoms in the $m_F = +1$ state and in the $m_F = -1$ state after 200 ms of spin-mixing from a pure $m_F = 0$ condensate. The relative number squeezing corresponds to sub-Poissonian fluctuations in the magnetization $M = N_{+1} - N_{-1}$, where N_{+1} and N_{-1} are the number of atoms in the $m_F = +1$ and $m_F = -1$ state, respectively. For $\tilde{N} = N_{+1} + N_{-1} = (300, 2000)$ atoms in the $m_F = \pm 1$ states, the fluctuations in the magnetization $\Delta M = \Delta(N_{+1} - N_{-1})$ are reduced up to 10 dB below the classical shot noise limit. This is the first demonstration of sub-Poissonian spin statistics in a spin-1 condensate and provides a solid foundation for future experiments involving the demonstration of squeezing in a spinor condensate.

8.1 *Spin-Mixing from a pure* $m_F = 0$

In the mean field description (see Equations 7.16a 7.16b), a pure $|F = 1, m_F = 0\rangle$ condensate does not spin-mix since $\dot{\psi}_{\pm 1} = 0$. However, for a ferromagnetic condensate $(c_2 < 0)$ with zero magnetization, the ground state is not necessarily given by a pure $m_F = 0$ condensate. To better understand the process of spin-mixing from a pure $m_F = 0$ condensate, we consider the spin-dependent energy per particle in the mean

field:

$$\mathcal{E} = \frac{c_2}{2}n\langle\vec{F}\rangle^2 + q\langle\hat{F}_z^2\rangle, \tag{8.2}$$

where $\vec{F} = \hat{F}_x\hat{x} + \hat{F}_y\hat{y} + \hat{F}_z\hat{z}$ denotes the dimensionless spin vector operator with

$$\hat{F}_x = \frac{1}{\sqrt{2}}\left[(\hat{\psi}_{+1}^\dagger + \hat{\psi}_{-1}^\dagger)\hat{\psi}_0 + \hat{\psi}_0^\dagger(\hat{\psi}_{+1} + \hat{\psi}_{-1})\right], \tag{8.3a}$$

$$\hat{F}_y = \frac{i}{\sqrt{2}}\left[(\hat{\psi}_{+1}^\dagger - \hat{\psi}_{-1}^\dagger)\hat{\psi}_0 - \hat{\psi}_0^\dagger(\hat{\psi}_{+1} - \hat{\psi}_{-1})\right], \tag{8.3b}$$

$$\hat{F}_z = \hat{\psi}_{+1}^\dagger\hat{\psi}_{+1} - \hat{\psi}_{-1}^\dagger\hat{\psi}_{-1}, \tag{8.3c}$$

and $\hat{\psi}_j^\dagger$ ($\hat{\psi}_j$) being the atomic field creation (annihilation) operator associated with the $m_F = j$ hyperfine spin state [98, 99]. The first term in Equation 8.2 describes the spin-dependent interatomic interactions. For ^{87}Rb $F = 1$ atoms $c_2 < 0$ and therefore the spin interaction term is minimized for a large net magnetization $\langle\vec{F}\rangle^2$, which is maximized when the spinors are aligned and all point in the same direction. This spin configuration is referred to as a ferromagnetic phase. The ferromagnetic phase of a condensate with no magnetization along the quantization axis ($\langle\hat{F}_z\rangle = m = 0$) has a non-zero transverse magnetic field $\langle\vec{F}_x\rangle^2 + \langle\vec{F}_y\rangle^2 \neq 0$. The second term in Equation 8.2 takes into account the change in energy due to Zeeman shift E_j of the $m_F = j$ states in an external magnetic field with $q = (E_{+1} + E_{-1} - 2E_0)/2$ describing the quadratic Zeeman shift. (The ground state energy due to the linear Zeeman shift $\eta\langle\hat{F}_z\rangle$ with $\eta = (E_{-1} - E_{+1})/2$ has been omitted in Equation 8.2 because it is proportional to the magnetization $m = \langle\hat{F}_z\rangle$ along the quantization axis and therefore is conserved.) In our system $q \approx h \times (72\text{ Hz/G}^2)B^2$ given a magnetic field of magnitude B. In the single mode approximation:

$$\langle\hat{F}_z^2\rangle = \langle\hat{\psi}_{+1}^\dagger\hat{\psi}_{+1} + \hat{\psi}_{-1}^\dagger\hat{\psi}_{-1}\rangle = 1 - \rho_0, \tag{8.4}$$

with ρ_0 equal to the population in the $m_F = 0$ state. The Zeeman energy is thus minimized for a pure $m_F = 0$ condensate. As this state has no net magnetization ($\langle\vec{F}\rangle^2 = 0$), it is referred to as a polar state. Unlike the polar phase, the ferromagnetic

phase has a net transverse magnetization, which breaks the rotational symmetry of the polar phase. Since the two phases have distinct symmetries, there is a quantum phase transition at $q = 2|c_2|n$. In order to get an idea of the ground state populations of the spinor condensate, we invoke the single mode approximation (SMA). In the SMA, the spin operators can be reduced to $\hat{\psi}_j(\vec{r}) = \phi(\vec{r})\sqrt{\rho_j}e^{-i\theta_j}$, where $\phi(\vec{r})$ is the common spatial mode of the spin components and ρ_j the fractional spin population with $\sum_j \rho_j = 1$. As a result, the spin-dependent energy per particle can be written in terms of the fractional spin population ρ_0 and the relative phase $\theta = \theta_+ + \theta_- - 2\theta_0$:

$$\mathcal{E} = c_2 n\rho_0 \left[(1-\rho_0) + \sqrt{(1-\rho_0)^2 - m^2} \cos\theta\right] + q(1-\rho_0). \tag{8.5}$$

For ferromagnetic interactions $(c_2 < 0)$, the energy is minimized for $\theta = 0$ and it therefore follows that the ground state populations are determined by minimizing

$$\mathcal{E} = c_2 n\rho_0 \left[(1-\rho_0) + \sqrt{(1-\rho_0)^2 - m^2}\right] + q(1-\rho_0). \tag{8.6}$$

In a system with $m = 0$ and $q < 2n|c_2|$, the ground state populations are

$$\rho_0 = (1/2)(1 - q/2nc_2) \text{and} \tag{8.7a}$$

$$\rho_\pm = \frac{1}{4}(1 + q/2nc_2) \tag{8.7b}$$

otherwise $\rho_0 = 1$ and $\rho_{\pm 1} = 0$.

A pure $m_F = 0$ condensate with $q < 2n|c_2|$, is dynamically unstable because it is not in the ground state of the system. The relaxation to the minimum energy state requires the generation of $m_F = \pm 1$ pairs through a spin-exchange collision of two $m_F = 0$ atoms. However, the spin-mixing rate of a pure $m_F = 0$ condensate is zero. In order to initiate spin-mixing, a non-zero population in the $m_F = \pm 1$ states is necessary. The non-linear dynamics of the phase transition from a polar state to a ferromagnetic state have been studied in a variety of experiments for $F = 1$ systems [100, 99, 101, 102] and also for $F = 2$ systems [103, 104, 105, 106] and have been the topic of many theoretical invetigations [93, 107, 94, 108, 95, 109, 110, 111, 112, 113].

Besides classical noise, thermal and quantum fluctuations in the magnetization can initiate spin-mixing in a dynamically unstable condensate. The importance of the quantum fluctuations have been verified experimentally [104] in a $F = 2$ system. If only quantum fluctuations in the magnetization are present, then the amplification of these fluctuations through spin-mixing is equivalent to the parametric amplification of vacuum fluctuations in optics. In this analogy, the pure $m_F = 0$ condensate corresponds the coherent pump that generates a $m_F = \pm 1$ pair, with one being the signal and the other the idler. The nonlinear interaction within the condensate, namely the collisions, take the place of the non-linear medium and the input is either the vacuum state or a classical seed of atoms in the $m_F = \pm 1$ states.

For the spin-mixing experiments described in this chapter, we create a pure $m_F = 0$ condensate in a high magnetic field $B \approx 2$ G. In this field, the Zeeman energy dominates the spinor interaction and the condensate remains in the $m_F = 0$ state. The condensate contains $N_{\text{total}} \approx 3500$ atoms in a single lattice site. Given the trap frequencies $(\omega_\perp, \omega_z) = (2\pi \times 340, 2\pi \times 3500)$ Hz, the condensate has a peak density of $n_0 = 6.5 \times 10^{14}$ atoms/cm^3, and Thomas-Fermi radii $(r_\perp, r_z) = (3.2, 0.31)$ μm. The system is thus characterized by the spin-dependent interaction energy $2|c_2|n_0 = h \times 47$ Hz and the spin-healing length $\xi_s = \sqrt{\hbar^2/2m|c_2|n_0} = 1.6$ μm (here m is the mass of the atom), which describes the minimum size of a spin-domain. Since in our experiment $r_\perp > \xi_s$, spin domains can form in the radial direction this would violate the SMA. In order to initiate spin-mixing we rapidly quench the BEC across the quantum phase transition by lowering the magnetic field to 360 mG in 10 ms. At this final magnetic field $q = h \times 9.3$ Hz $< 2|c_2|n_0$. The spin populations are measured after a free expansion of 7.5 ms using fluorescence imaging as described in Chapter 6.2 with a probe intensity $I_0 = 31I_{sat}^0$ for 100 μs. During the first 4 ms of the expansion, a Stern-Gerlach field is applied in order to separate the three spin components spatially.

8.1.1   An Example

In this experiment, the average fractional population in the $m_F = 0$ state is determined for various hold times t (after the quench) see Figure 8.1. Initially ($t \lesssim 50$ ms), no significant spin-mixing is visible, while for $t \gtrsim 100$ ms the condensate undergoes spin-mixing. However, the degree of spin-mixing is unpredictable and varies from run to run, which is illustrated by the large error bars for the average population in the ρ_0 state. At $t = 200$ ms, for example, $\rho_0 = 0.65 \pm 0.22$ and both $\rho_0 = 0.34$ and $\rho_0 = 0.96$ can be observed (see Figure 8.2). This is not surprising because the $m_F = 0$ condensate is a meta-stable state and the spin-mixing process is triggered through noise (either classical or quantum). Finally ($t \gtrsim 1000$ ms), the spin populations reach equilibrium and the fluctuations in ρ_0 reduce to the level of the fluctuations expected due to atoms loss. We determine the ground state population by holding the condensate in the trap for over 3 s to ensure the condensate is in equilibrium. We measure $\rho_0 = 0.61 \pm 0.05$, which agrees well with the SMA prediction $\rho_0 = 0.60$ (see Equation 8.7) for the initial condition of our system. As the atoms are lost out of the trap, however, the spin-dependent interaction is reduced shifting the ground state of the system toward the polar state. After 3 s, the number of atoms left in the condensate is 500, which (in the SMA) is predicted to have the ground state population of $\rho_0 = 0.72$. The slightly increase of the fraction of atoms in the ρ_0 state for longer hold times (see Inset of Figure 8.1) can be explained by the decrease in the spin-dependent interaction due to atom loss.

8.2   Sub-Poissonian fluctuations in the magnetization

In this section, we describe our observation of sub-Poissonian fluctuations in the magnetization of a spin-1 condensate after spin-mixing from a pure $m_F = 0$ condensate in a single lattice site. The experimental conditions are described in Section 8.1. The noise driven spin-mixing from a pure $m_F = 0$ causes a significant variance in the
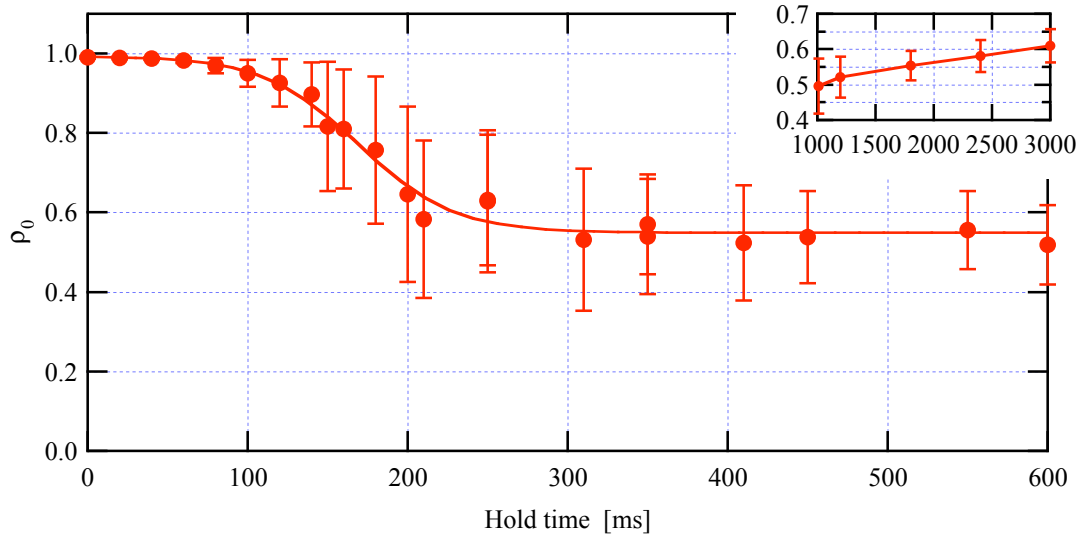
Figure 8.1: Spin-mixing from a pure $m_F = 0$ condensate: a plot of the average fractional population of the $m_F = 0$ state, namely, ρ_0 as a function of holding time after the quench of the condensate. In this experiment, two lattice sites are occupied and at $t = 0$ ms the total number of atoms in the condensate is 6600. The experimental was done in a magnetic field with $B = 360$ mG. The data points are an average of approximately 100 runs, the error bars indicate the experimental fluctuations and the line is added as an guide to the eye. In the inset, we show the data for long trap times ($t > 1$ s) for which the condensate is in a quasistatic equilibrium. Since the atom loss reduces the spin-dependent interactions, the ground state of the condensate is changing with the holding time. At 3 ms, the fractional population in the $m_F = 0$ state is determined to be $\rho_0 = 0.61 \pm 0.05$.
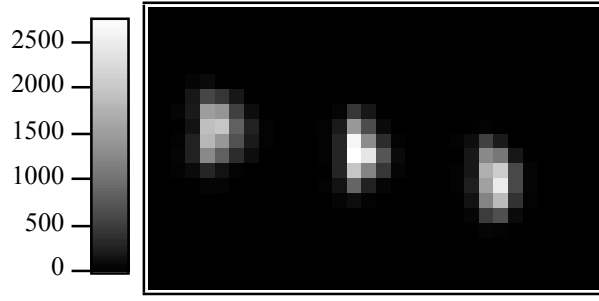
(a)
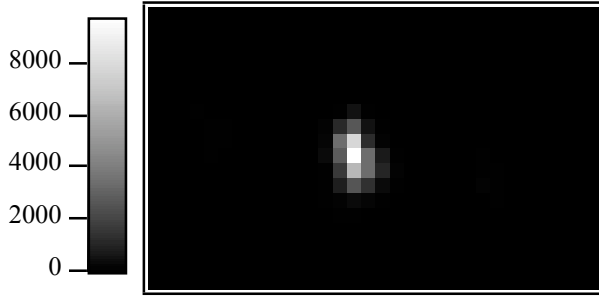
(b)
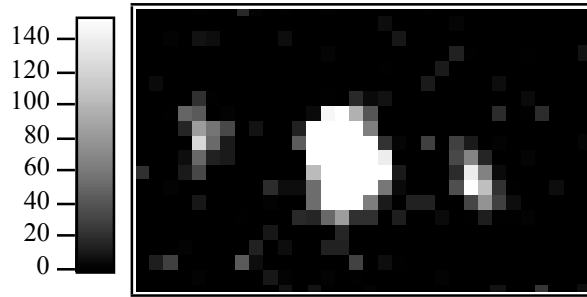
(c)

Figure 8.2: Images of a spin-1 condensate in a single lattice site after 200 ms of spin-mixing from a pure $m_F = 0$. The spin components in the image are from left to right are $m_F = +1$, $m_F = 0$, and $m_F = -1$. The degree of spin-mixing varies significantly from run to run. In image (a) the condensate has spin-mixed such that $\approx 66\,\%$ of the total population is in the $m_F = \pm 1$ states. For this example, $N_{+1} = 1101$, $N_0 = 1135$, and $N_{-1} = 1067$. In contrast, in image (b) the condensate has barely spin-mixed. Here $N_{+1} = 55$, $N_0 = 3009$, and $N_{-1} = 64$. Image (c) is the same as image (b). It is re-scaled to show the signal of the atoms in the $m_F = \pm 1$ states. In all images (a) - (c), the condensate is imaged after a time of flight of 7.5 ms and gravity points from right to left. The field of view of the images is 665.6 μm x 384 μm. The pixels are binned 16 x 16, in order to reduced the readout noise of the camera. As a result the area of a pixel in the image is 20.8 x 20.8 μm^2.

(a)

$N = N_{+1} + N_{-1}$
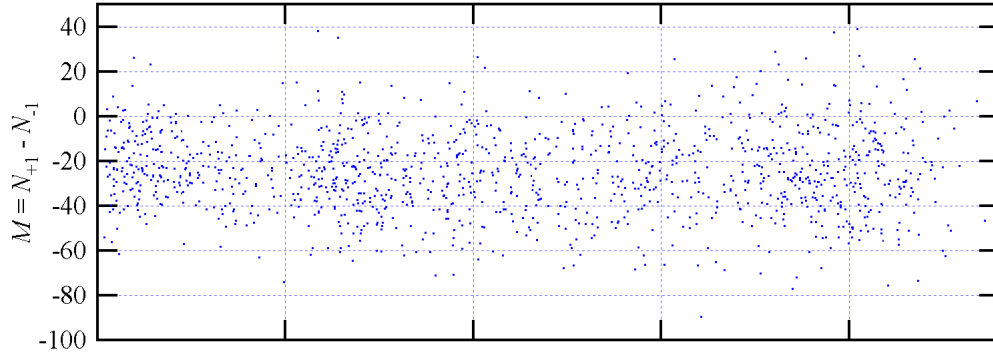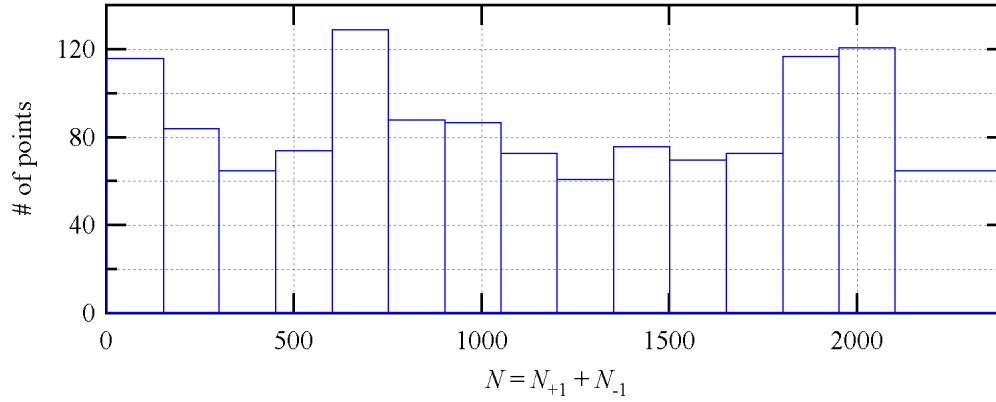
(b)

Figure 8.3: (a) Magnetization versus the number of atoms generated in the $m_F = \pm 1$ state after spin-mixing from a pure $m_F = 0$ condensate. (b) In order to make a comparison with a Poissonian distribution, we bin the data into bins with a width of 150 atoms as indicated in the graph.

degree of spin-mixing despite the fact that the experimental conditions are kept the same and the total atom number fluctuates by less than 3 %. We therefore repeat the experiment 1300 times and acquire datasets for different degrees of spin-mixing. In Figure 8.3(a), the magnetization $M = N_{+1} - N_{-1}$ is plotted versus the number of atoms $\tilde{N} = N_{+1} + N_{-1}$ in the $m_F = \pm 1$ states. This data is then binned into bins with a width of $\tilde{N} = 150$ atoms such that each dataset contains a sufficiently large number of data points (typically > 60) to determine the fluctuations of the magnetization (see Figure 8.3(b)). Two such datasets are shown as histogram plots in Figure 8.4. In order to illustrate the reduced magnetic fluctuations compared to the Poissonian case, the data is fit to a Gaussian distribution (solid blue line) and is compared to the expected Poissonian distribution (red dashed curve) given the same mean atoms number $\langle \tilde{N} \rangle$ in the $m_F = \pm 1$ states. For both these examples, the fluctuations in the magnetization or relative atom number are clearly sub-Poissonian.

To highlight the difference between the fluctuations of the magnetization generated through spin-mixing compared to those of a Poissonian distribution, we contrast the data with a coherent spin state generated through a radio frequency (RF) rotation (see Figure 8.6). The data for the coherent spin state is the same data used to calibrate the imaging system in Chapter 6.2. As in the spin-mixing experiment, we begin with a pure $m_F = 0$ BEC. However, instead of initiating spin-mixing, we apply a RF pulse (at a magnetic field of 430 mG) resonant with the Zeeman splitting between the $m_F = 0$ state and the $m_F = \pm 1$ states, and thus create a coherent (spin state) superposition of the 3 Zeeman levels in the $F = 1$ manifold. As mentioned in Chapter 6.2, the quantum projection noise of the magnetization $(\Delta M)^2$, associated with such a coherent spin state, is equal to the average number of atoms in the $m_F = \pm 1$ states, therefore exhibiting Poissonian statistics. In Figure 8.5, we show two histograms of the magnetization for a coherent spin state and compare them with those of the spin-mixed state. The Gaussian width of the distribution of

the magnetization is larger than for the corresponding spin-mixed state illustrating the reduced fluctuations in a spin-mixed state. In Figure 8.6, we plot the standard deviation of the magnetization versus the average atom number in the $m_F = \pm 1$ states for both the coherent spin state and the spin-mixed state. The graph clearly shows that the magnetic fluctuations are reduced for the spin-mixed state compared to the coherent state. The spin-mixed state is fit to a noise curve of the form

$$\Delta M = \sqrt{\sigma_{\text{bkg}}^2 + \sigma_{\text{PSN}}^2 + c\tilde{N}}, \tag{8.8}$$

where the photon shot noise σ_{PSN}^2 is not fit but given by the total number of atoms. The fit gives a background noise of $\sigma_{\text{bkg}}^2 = 15 \pm 1$ atoms, which is slightly larger than the previously determined background noise (due to the background scatter and the camera readout noise) of 11 ± 4 atoms, but it is within the margin of error. An increase in the background noise can be potentially related to a contamination of the initial pure $m_F = 0$ condensate with a few atoms in the $m_F = \pm 1$ states. Another reason for the increase could be a change in the background scatter, which can vary slightly from day to day. The fit also shows a small dependence of the noise on the number on the number of atoms in the $m_F = \pm 1$ states: $c = 0.05 \pm 0.02$. We suspect that this is also result of the atom loss. In the 200 ms of spin-mixing we loose $\approx 15\%$ of the total number of atoms in the trap. For a rough estimate of the noise due to atom loss, we assume the atoms spin-mix without loss after which 15% of the atoms are randomly discarded from the condensate. In this case, the spin components are lost out of the trap with an equal probability $q = (1 - p) = 0.15$. The initial atom number $N_i(t = 0 \text{ ms})$ of a spin component in the state $m_F = i$ state in terms of the measured atom number after 200 ms of spin-mixing $N_i(t = 200 \text{ ms})$ is $N_i(t = 0 \text{ ms}) = N_i(t = 200 \text{ ms})/q$. The noise in the atom number $N_i(t = 200 \text{ ms})$ is $\sigma_{\text{loss}}^2 = p(1 - p)N_i(t = 0 \text{ ms})$ and the noise in the magnetization due to atom loss is equal to $\sigma_{\text{loss}}^2 = p(1 - p)\tilde{N}(t = 0 \text{ ms}) = (1 - p)\tilde{N}(t = 0 \text{ ms}) = 0.15\tilde{N}$. This is clearly an overestimation of the noise because in reality the atoms are lost during

the spin-mixing process (not after spin-mxing). It is therefore not surprising that the rough estimation is three times as large as the measured value of $c = 0.05 \pm 0.02$.

To quantify how much the magnetic fluctuations are suppressed in comparison with a Poissonian distribution, we define a number squeezing parameter $\xi_N^2 = (\Delta M)^2/\tilde{N}$ (See Figure 8.8). Without correcting for detection noise, we see a suppression of the magnetic fluctuations by up to $10 \log_{10} \xi^2 = -6.8$ dB (blue circles). By taking into account the detection noise, we deduce a number squeezing factor of up to ≈ -10 dB (green squares).

The data clearly exhibits sub-Poissonian fluctuations in the magnetization, however, as can be seen from the data in Figure 8.4, there is a small, but statistically significant, deviation of the average magnetization from zero. In order to investigate this in more detail, the magnetization is plotted as a function of spin mixing time in Figure 8.9(a). In the same figure, the measured experimental standard deviation of the magnetization, ΔM, is shown by the error bars and is plotted separately in Figure 8.9(b) as a function of spin mixing time. The data is taken from the experiment described in Section 8.1.1, in which the condensate occupies two lattice sites instead of a single site as it is the case for the previously presented data. The observation that the magnetization drifts below zero and then gradually increases back to zero as the condensate decays is slightly puzzling. Although the drifts are comparable to the uncertainties in the measurement, there is a clear trend in the data. Possible explanations include a time-varying non-uniform background drift of either the camera or scatter level, although we nominally correct for such drifts using adjacent regions of the image containing no atoms. It is also possible that small magnetic field gradients or curvatures bias the trap to one component, which could lead to a bias in the loss rate. While this could explain the data at early times, it would not explain why the magnetization returns to zero for longer hold times. We note that similar drifts in the magnetization were observed in earlier spin mixing experiments

in our group [100, 58] (although with complete different apparatuses), and hence this warrants further investigation.

The fluctuations of the magnetization also exhibit interesting dynamics as shown in Figure 8.9(b). The initial growth in ΔM is dominated by σ_{PSN} as $\tilde{N} = N_{+1} + N_{-1}$ is increasing during this time. This growth is similar to the $\tilde{N}$ dependence shown in Figure 8.6 for the experiments performed at fixed time. The gradual reduction of ΔM for times $t \leq 500$ ms shown in 8.9(b) can be attributed to random, uncorrelated losses of the $m_F = \pm 1$ atoms. The effect of the random atom loss on the fluctuations can be described with a simple model once the condensate has reached as steady state. We assume that the condensate has reached a steady state after 450 ms of spin-mixing with $\tilde{N}(t = 450 \text{ ms}) = 2930$ atoms in the $m_F = \pm 1$ states. This spin-mixed state will have some initial noise in the magnetization because of the atom loss that is occurring during the spin-mixing, which we will group into the background noise σ_{bkg}^2. The decay rate of the atoms in the $m_F = \pm 1$ states for trap hold times ≥ 450 ms is determined by fitting the number of atoms in the $m_F = \pm 1$ as a function of trap hold time to an exponential. The fit shown in Figure 8.7 and gives a decay rate $R = 0.00065 \pm 0.00003$ 1/ms. Therefore the probability for an atom in the $m_F = \pm 1$ state to remain in the trap as a function of time is given by $p(t) = e^{-R(t-450 \text{ ms})}$, the average number of atoms in the $m_F = \pm 1$ states by $\tilde{N}(t) = p(t)\tilde{N}(t = 450 \text{ ms})$ atoms, and noise in the magnetization due to the atom loss by $\sigma_{\text{loss}}^2(t) = p(t)(1 - p(t))\tilde{N}(t = 450 \text{ ms})$. Since the number of atoms in the $m_F = \pm 1$ states in the trap changes with hold time, the photon shot noise will also depend on the trap hold time and is given by $\sigma_{\text{PSN}}^2 = \tilde{N}(t)/a$, where $a = 18.2$ electrons per atom is the calibration constant. The noise in the magnetization is fit to the expected magnetization for $t \geq 450$ ms:

$$\Delta M = \sqrt{\sigma_{\text{bkg}}^2 + \sigma_{\text{PSN}}^2 + \sigma_{\text{loss}}^2} \tag{8.9a}$$

$$= \sqrt{b^2 + \left(\frac{1}{a} + (1 - p(t))\right) p(t)\tilde{N}(t = 450 \text{ ms})}, \tag{8.9b}$$

114

with $p(t) = e^{-R(t-450 \text{ ms})}$ and where b is the only free parameter. The standard deviation of the magnetization as a function of spin-mix time and the fit are shown in Figure 8.9(b). The fit gives $b = 15 \pm 2$ atoms.

As the atoms are lost out of the trap, the fluctuations in the magnetization approach the classical limit. Assuming the noise in the measured magnetization is solely due to losses and that these losses occur after spin-mixing, the number squeezing parameter as a function of time is given by $\xi_N^2(t) = p(t)(1 - p(t))\tilde{N}/p(t)\tilde{N} = (1 - p(t))$. Here $\tilde{N}$ is the number of atoms in the $m_F = \pm 1$ after spin-mixing but before losses. For $t \to \infty$, $p(t) \to 0$, and $\xi_N^2 \to 1$: the system converges to a Poissonian distribution. The number squeezing parameter as a function of spin-mixing time is plotted in Figure 8.10. Initially, pairs of $m_F = \pm 1$ atoms are generated and the number squeezing parameter decreases. As expected, uncorrelated losses limit the relative number squeezing and eventually destroys the relative number squeezing. For a comparison with the previous data taken after 200 ms of spin-mixing (see Figure 8.8), we also plot the number squeezing parameter as a function of the average number of atoms in the $m_F = \pm$ states (see Figure 8.11).

In summary, we have generated up to 1150 $m_F = \pm 1$ atom pairs, with a standard deviation of less than 17 atoms (correcting for the imaging noise) and have created condensates with sub-Poissonian fluctuations in the relative atom numbers, i.e. the magnetization. The fluctuations are reduced up to 10 dB, which is limited by the atom loss out of the trap during the 200 ms of spin-mixing. This relative number squeezing is indicative of the the predicted pair-correlations in a spin-1 condensate [41, 42, 55] and therefore is a very exciting and promising result as it lays the foundation for future experiments involving spin-squeezing and entanglement measurements.
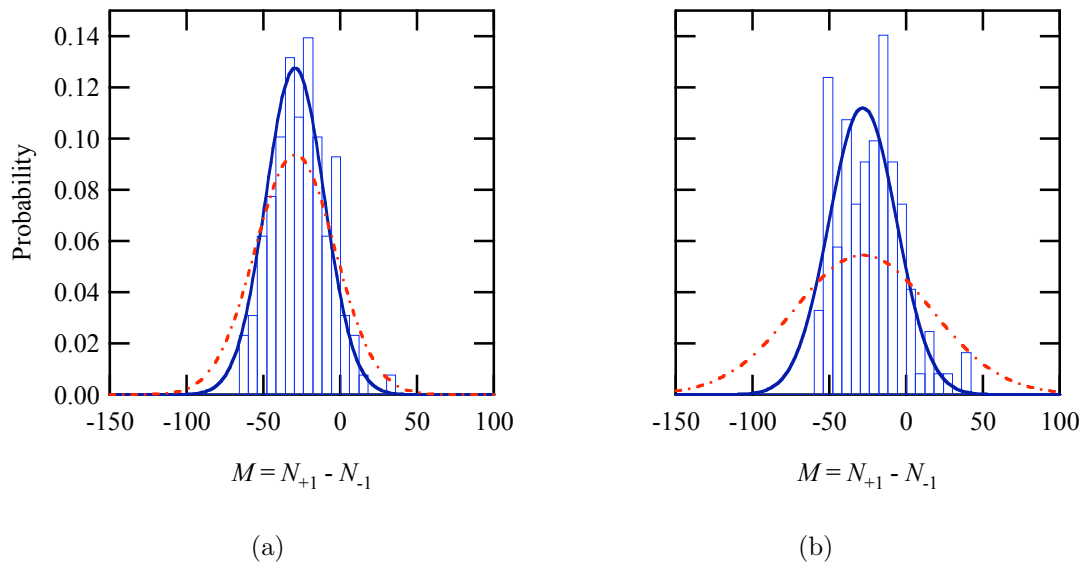
Figure 8.4: Histograms of the magnetization after spin-mixing for (a) $\langle \tilde{N} \rangle = 674$ atoms and (b) $\langle \tilde{N} \rangle = 2025$, where $\langle \tilde{N} \rangle$ is the average total number of atoms in the $m_F = \pm 1$ states for the corresponding bin. The blue lines are a Gaussian fit to the distributions, the corresponding widths are 19 ± 1 and 22 ± 2 atoms, respectively. Both these value are lower than the corresponding Poissonian distributions with width $\sqrt{\langle N \rangle}$ ($= 26$ and $= 45$ atoms, respectively), indicated with a a red dashed line.
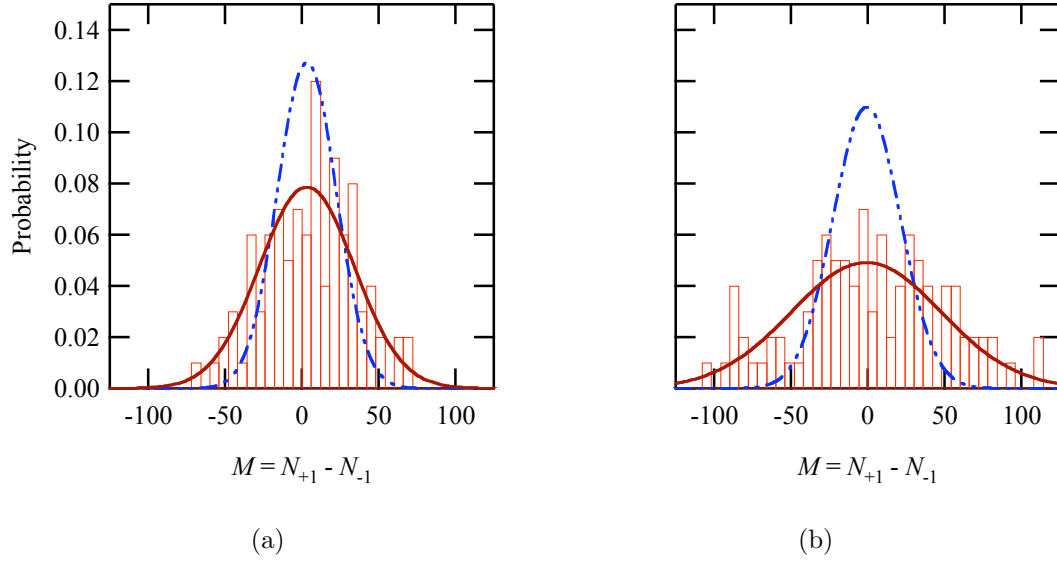
Figure 8.5: Histograms of the magnetization for a coherent spin state for (a) $\langle \tilde{N} \rangle = 644$ atoms and (b) $\langle \tilde{N} \rangle = 2018$, where $\langle \tilde{N} \rangle$ is the average total number of atoms in the $m_F = \pm 1$ states. The red lines are a Gaussian fit to the distributions, the corresponding widths are 31 ± 2 and 49 ± 4 atoms, respectively. Due to the detection noise, both these values are higher than the corresponding Poissonian distributions with width $\sqrt{\langle N \rangle}$ ($= 25$ and $= 45$ atoms, respectively). The widths of the the spin-mixed state with an equivalent average number of atoms in the $m_F = \pm 1$ states (see Figure 8.4) are indicated with a blue dashed line for comparison. The fluctuations in the magnetization are clearly larger for the coherent spin state compared to the spin-mixed state.
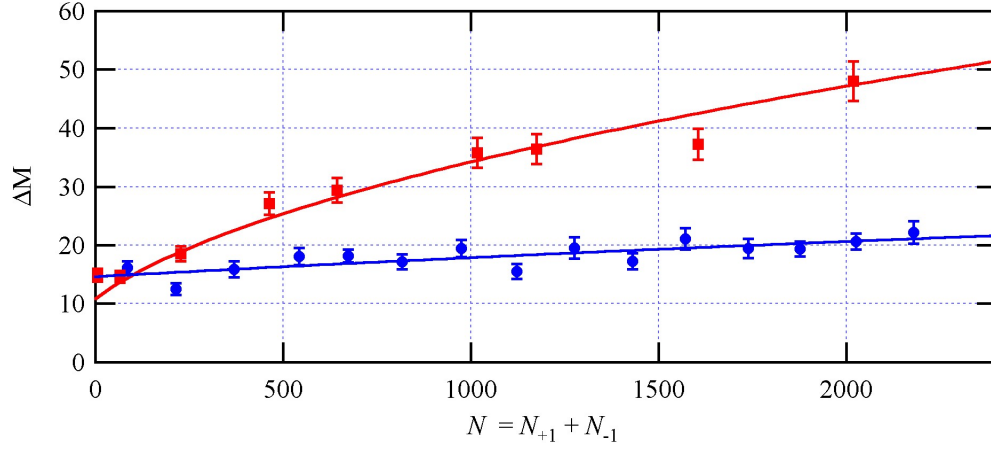
Figure 8.6: Fluctuations in the magnetization versus atom number for a coherent spin state (red squares and line) and a spin-mixed state (blue circles and line). The fluctuations in the magnetization are less for the spin-mixed state compared to the coherent spin state. The error bars correspond to the absolute uncertainty in the measurement of the standard deviation given the finite size of the sample: $\Delta\sigma = \sigma/\sqrt{2(T-1)}$, where T is the number of data points used to determine $\sigma = \Delta M$.
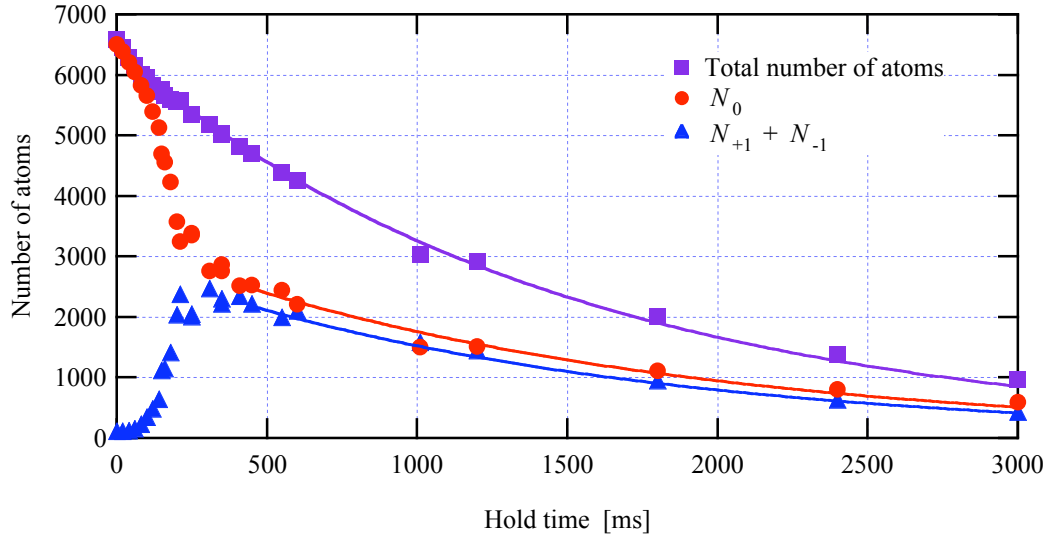
Figure 8.7: Number of atoms in the trap as a function of the trap hold time during spin-mixing from a $F = 1$, $m_F = 0$ condensate. The lifetime of the condensate is determined to be 1.5 s.
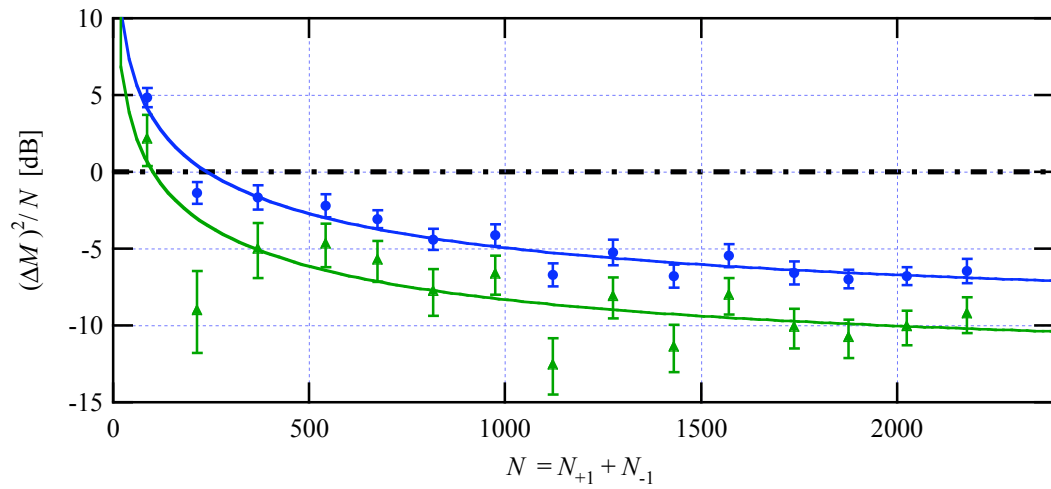
Figure 8.8: Number squeezing versus the degree of spin-mixing. The blue circles are the raw data and the green triangles are corrected for imaging noise. Even for a small number of $m_F = \pm 1$ generated atoms ($\tilde{N} > 214$), the number squeezing parameter is under the Poissonian limit (black dashed dotted line) for a coherent spin state. The error bars include the uncertainty due to the finite size of the sample and the uncertainties in the calibration constant and background scatter as determined by the fit shown in Figure 6.5. The lines indicate the fit used data in Figure 8.6.
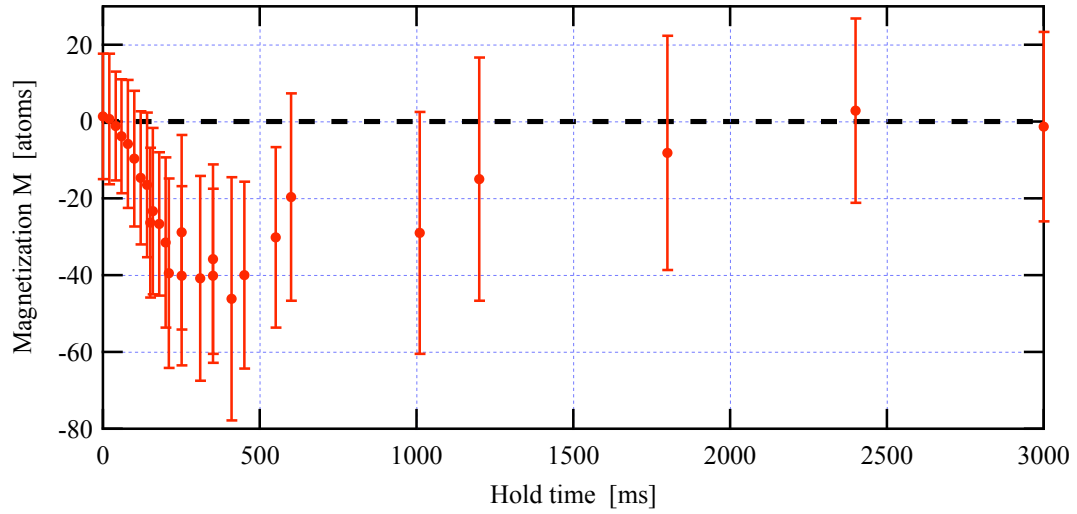
(a)
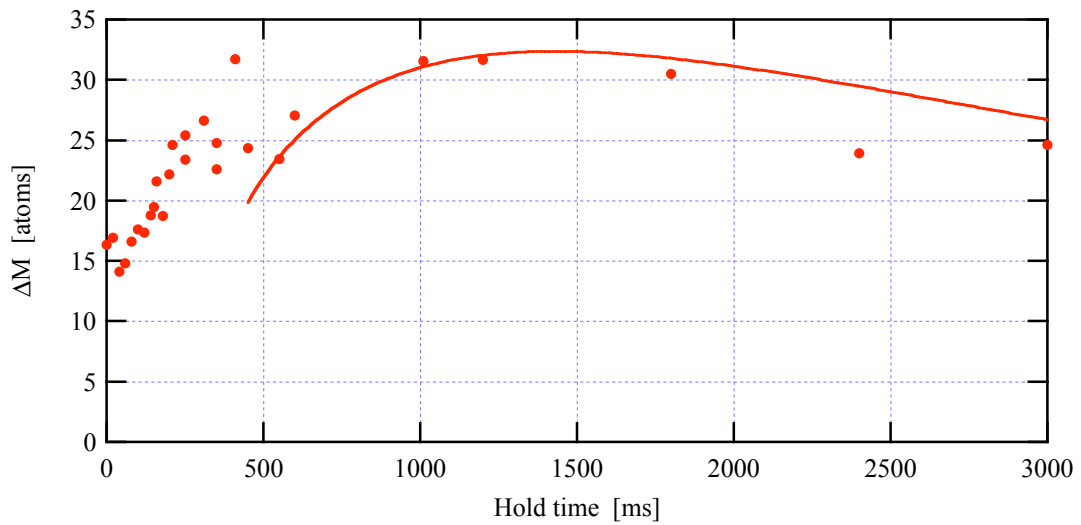
(b)

Figure 8.9: (a) Magnetization versus the hold time of the atoms in the trap. The error bars indicate the experimental standard deviation in the magnetization, which is separately plotted in (b) versus the hold time. The red line indicates the dependence of ΔM on the hold time due to atom loss out of the trap.
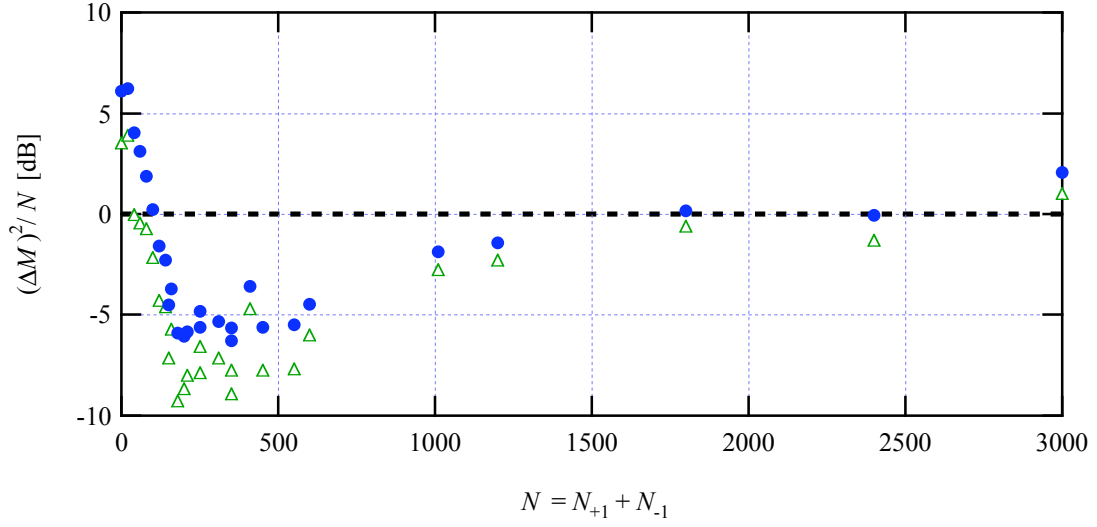
Figure 8.10: Number squeezing versus spin-mixing time. The blue circles are the raw data and the green triangles are corrected for imaging noise. As pairs of $m_F = \pm 1$ atoms are generated the number squeezing parameter decreases. The fluctuations in the magnetization are reduced by ≈ 8 dB. Uncorrelated losses due to the finite lifetime of the atoms in the trap limit the relative number squeezing. With increasing trap hold time the fluctuations approach the classical limit (black dashed line).
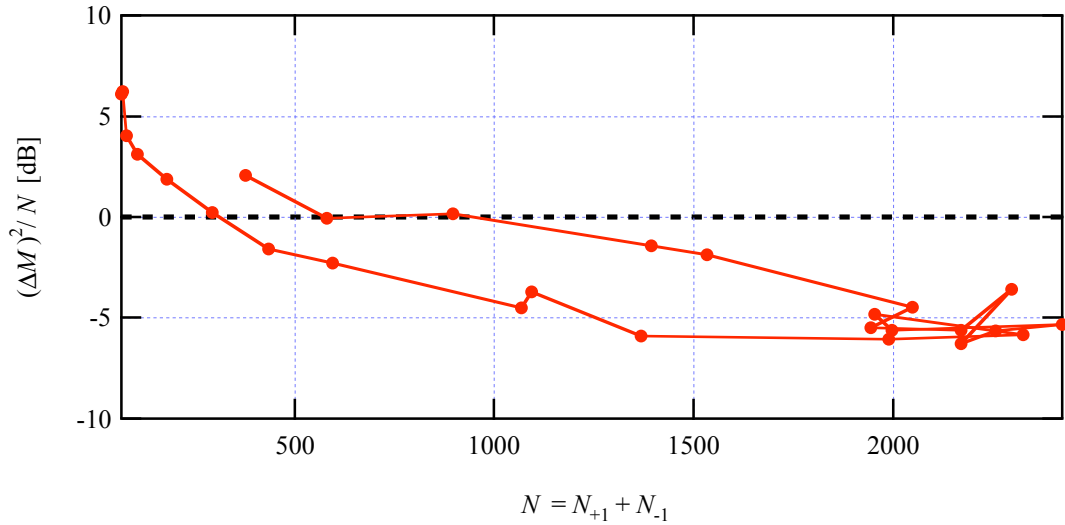
Figure 8.11: Number squeezing versus average number of atoms in the $m_F = \pm 1$ states. The data shown is the raw data. The line connects the data points in terms of trap hold time.

CHAPTER IX

FINAL REMARKS AND OUTLOOK

In this thesis, we have investigated the two methods of imaging used in our lab, absorption and fluorescence imaging, and have tested their noise limits. Furthermore, we have implemented a new method of calibrating our imaging set-up using quantum projection noise. The advantage of this method is that it is does not require the exact knowledge of the collection efficiency of the lens or the quantum efficiency of the camera. Given our goal to detect atom fluctuations under the atom shot noise limit $(< \sqrt{N})$, fluorescence imaging outperforms absorption imaging. For fluorescence imaging, the noise floor for counting the atoms in a single spin-component is ≈ 7 atoms for an area of 208 x 208 μm^2 large , whereas for absorption imaging it is ≈ 24 atoms for an area of 100 x 100 μm^2.

In one of our experiments, we have created an array of independent condensates in the standing wave potential of a CO_2 laser. The lattice spacing is 5.3 μm, which is larger than our imaging resolution ≈ 3 μm, and therefore allows us to image the *in situ* structure of the lattice using absorption imaging. Diffraction effects, however, prevent us from extracting quantitative measurements from the *in situ* images. We have successfully addressed and manipulated the single lattice sites using microwaves and thus have demonstrated that microwaves can be used to measure the number of atoms in an individual lattice site. By interfering two lattice condensates, we have shown the coherence of the individual lattice sites.

Finally, we have observed sub-Poissonian number fluctuations in the magnetization of a spin-1 condensate after 200 ms of spin-mixing from a pure $m_F = 0$ condensate. The fluctuations are reduced up to 10 dB with respect to a coherent spin

state. This measurement is very exciting because it opens the door to measurements of spin-mixing or entanglement. The creation of $m_F = \pm 1$ atoms pairs through the collision of two $m_F = 0$ atoms, can be considered a matter wave counterpart to parametric amplification in quantum optics. The pure $m_F = 0$ condensate is equivalent to the coherent pump out of which $m_F = \pm 1$ atom pairs are generated. As in quantum optics, the $m_F = \pm 1$ atom pairs are predicted to pair correlated [42, 41].

For our future work, we intend to measure the spin-squeezing generated through spin-mixing in a $m_F = 0$ condensate. In the un-depleted pump approximation the population of the $m_F = \pm 1$ components remains small compared to the population in the $m_F = 0$ state. In this case, the $m_F = \pm 1$ atom pairs can be described by a spin-1/2 system and the spin-squeezing condition is given by 9.4. Next, we will introduce the reader to the concept of spin-squeezing through the example of a spin-1/2 system.

9.1 Spin-Squeezing

Quantum fluctuations between two non-commuting observables are an intrinsic characteristic of quantum mechanics. The commutator $[\hat{A}, \hat{B}] = i\hat{C}$ of two non-commuting (Hermitian) observables $\hat{A}$ and $\hat{B}$ determines their uncertainty product

$$\langle(\Delta\hat{A})^2\rangle\langle(\Delta\hat{B})^2\rangle \leq \frac{1}{4}\langle\hat{C}\rangle^2. \tag{9.1}$$

For canonically conjugate operators $\hat{C} = \hbar$ and the uncertainty relationship reduces to the well-know Heisenberg uncertainty principle and is independent of the quantum state. In this case, the standard quantum limit (SQL) of the observables is given by $\frac{\hbar}{2}$. The uncertainty of an observable, for example $\langle(\Delta\hat{A})^2\rangle$, can be reduced under the SQL at the expense of a greater uncertainty in the other observable, $\langle(\Delta\hat{B})^2\rangle$. This redistribution of quantum fluctuations is often referred to as squeezing. In summary, the system can be regarded as squeezed if the uncertainty of one of the obervables, $\langle(\Delta\hat{A})^2\rangle$ or $\langle(\Delta\hat{B})^2\rangle$ is less than $\frac{\hbar}{2}$.

For spin systems, however, spin-squeezing requires a more stringent definition as

123

the spin-components are not canonically conjugate operators. This is necessary, if the definition of spin-squeezing should, as a minimum requirement, reflect quantum correlations between the individual atomic spins. Historically, atomic spin-squeezing was first considered for two-level atoms, which can be describe as a fictitious spin-1/2 system. To get a basic understand of spin-squeezing, or how one can define spin-squeezing, we will consider spin-squeezing in an ensemble a spin-1/2 particle (as is done in[22]).

The spin or angular moment of a system $\vec{J} = (J_x, J_y, J_z)$ is governed by the cyclic commutation relations $[J_i, J_j] = i\epsilon_{ijk}J_k$, where the indices i, j, k denote the components in any three orthogonal directions x, y, z and ϵ_{ijk} is the Levi-Civita symbol. Consequently, the components of the spin vector obey the uncertainty relationship $\langle \Delta J_i^2 \rangle \langle \Delta J_j^2 \rangle \geq \frac{1}{4} |\langle J_k \rangle|^2$. A coherent spin state (CSS) can be defined as an eigenstate $|\theta, \phi\rangle$ of a spin-component in the (θ, ϕ) direction, $J_{\theta,\phi} = J_x \sin\theta\cos\phi + J_y \sin\theta\sin\phi + J_z \cos\theta$, with eigenvalue J, where θ and ϕ denote polar and azimuth angles.

Let us now consider an ensemble of spin-1/2 particles. A CSS of a spin-1/2 can be written as $|\theta, \phi\rangle = \cos\frac{\theta}{2}|+\rangle + e^{i\phi}\sin\frac{\theta}{2}|-\rangle$, where $|+\rangle$ $(|-\rangle)$ is the eigenstate of S_z with eigenvalues $+\frac{1}{2}$ $(-\frac{1}{2})$. CSSs have a minimum uncertainty product, and therefore the components normal to (θ, ϕ) each have a variance at the SQL, i.e. are equal to $\frac{1}{4}$. An ensemble of N independent such CSSs with spin-1/2 corresponds to N spin-1/2 elements all pointing in the same mean direction (θ, ϕ) resulting in a total spin-J system, with $J = \frac{N}{2}$. This spin-J system is also a CSS. As there are no correlations between the spins, the variances of the different spin-components simply add. Consequently, the components normal to the (θ, ϕ) direction have a variance $\frac{N}{4}$ equal to the SQL. For simplicity, let us assume that the spin system is pointing in the $\hat{z}$-direction. If $N >> 1$, measurements of the J_x and J_y components can be described by a Gaussian probability distribution centered at the origin ($\langle J_x \rangle = \langle J_y \rangle = 0$) with a distribution width equal to $\langle (\Delta J_x)^2 \rangle = \langle (\Delta J_y)^2 \rangle = \frac{N}{4}$. By rotating the CSS, $\langle (\Delta J_x)^2 \rangle$

or $\langle(\Delta J_y)^2\rangle$ can be reduced under $\frac{N}{4}$. However, after the rotation the quantum state of the system remains a CCS, which would imply that squeezing is coordinate dependent and not state dependent. Therefore a more appropriate definition of spin-squeezing would be a state for which the variance of a spin component normal to the mean spin vector $\langle\vec{J}\rangle$ is less than $\frac{J}{2} = \frac{N}{4}$. We can therefore define a spin-squeezing parameter

$$\xi_S^2 \equiv \frac{2\langle(\Delta J_\perp)^2\rangle}{J}, \tag{9.2}$$

where $J_\perp$ is a spin component normal to the mean spin vector $\langle\vec{J}\rangle$ and the spin system can be considered squeezed if $\xi_S^2 < 1$. In this case, and given $N >> 1$, the probability distribution of the normal components is no longer isotropic, but is "squeezed" in one direction and stretched in the other. In order to squeeze a spin system it is necessary to generate quantum mechanical correlations or entanglement between the elementary spins. Therefore the squeezing parameter ξ_S indicates the degree of correlation between the spins. Because linear Hamiltonians merely rotate a quantum state, nonlinear interactions are required to generate correlations for spin-squeezing. An example of such a nonlinear interaction are collisions between atoms in a BEC, which has been predicted to generate entanglement [43] and has recently been implemented experimentally for spin-1/2 systems in a ^{87}Rb BEC [31, 18, 38, 37].

It is important to note that a state, which is spin squeezed under the above condition, does not necessarily improve the signal-to-noise ratio of a projection noise limited measurement. For example, in Ramsey spectroscopy or atom interferometry the squeezing definition above is not sufficient. In this case, a more relevant definition of the squeezing parameter is

$$\xi_R^2 \equiv \frac{2J\langle(\Delta J_\perp)^2\rangle}{|\langle\vec{J}\rangle|^2}, \tag{9.3}$$

For $\xi_R^2 < 1$ the precision of a measurement can be improved beyond the SQL, where ξ_R^{-1} corresponds to the increase in signal-to-noise over an uncorrelated state. Since $\xi_S \leq \xi_R$, metrological gain also satisfies the above criterion for correlations [114, 23].

More recently, spin squeezing has been defined in terms of multi-particle entanglement [43]:

$$\xi_E^2 \equiv \frac{2J\langle(\Delta J_{n1})^2\rangle}{\langle J_{n2}\rangle^2 + \langle J_{n3}\rangle^2}, \tag{9.4}$$

where $J_n = \hat{n} \cdot \vec{J}$ and the $\hat{n}_i$s are mutually orthogonal unit vectors. For $\xi_E^2 < 1$ the state of the atoms has been proven to be non-seperable, i.e. entangled [43]. Thus spin-squeezing defined in this manner is a sufficient requirement for entanglement. Note that if $\langle J_{n1}\rangle = 0$, then ξ_E and ξ_R are identical.

We have describe spin-squeezing for spin-1/2 systems. The spin-1 systems is much more involved. Although a spin-1 system can be split up into three spin-1/2 subsystems, the subsystems are not independent of each other and therefore cannot be squeezed independently [115]. However, the spin-squeezing condition for a spin-1/2 system can be extended to a spin-1 system as a criterion of many-particle entanglement [97, 115]. In the case of a three-level system, one can construct the two orthonormal states $|a\rangle$ and $|b\rangle$ from arbitrary superpositions of the three levels $|+\rangle$, $|-\rangle$, and $|0\rangle$, which in our case are the Zeeman levels of the $F = 1$ ground state. We can then define $\vec{J}_{ab} = \sum_{i=1}^{N} \vec{j}_i$ with the individual spin-1/2 operators $j_i^x = (|a\rangle\langle b| + |b\rangle\langle a|)/2$, $j_i^y = i(|a\rangle\langle b| - |b\rangle\langle a|)/2$, and $j_i^z = (|b\rangle\langle b| - |a\rangle\langle a|)/2$. The squeezing parameter for each spin-1/2 subsystem can then be defined as previously (see Equation 9.4):

$$\xi_{ab}^2 \equiv \frac{N\langle(\Delta J_{ab}^{n1})^2\rangle}{\langle J_{ab}^{n2}\rangle^2 + \langle J_{ab}^{n3}\rangle^2}, \tag{9.5}$$

where $J_{ab}^n = \hat{n} \cdot \vec{J}_{ab}$, the $\hat{n}_i$s are mutually orthogonal unit vectors, and N is the number of atoms in the ensemble. $\xi_{ab} < 1$ is an indication of multi-particle entanglement of the three level atoms. A more thorough analysis of a spin-1 condensate is work in progress.

APPENDIX A

TABLE OF CONSTANTS AND PROPERTIES OF ^{87}RB

Fundamental constants (2002 CODATA recommended values) and useful ^{87}Rb properties [60].

Quantity	Symbol	Value
Fundamental Constants		
Speed of light	c	$2.997\ 924\ 58 \times 10^8$ m/s (exact)
Permeability of Vacuum	μ_0	$4\pi \times 10^{-7}$ N/A^2 (exact)
Permitivity of Vacuum	ϵ_0	$(\mu_0 c^2)^{-1}$
Planck Constant	h	$6.626\ 069\ 3(11) \times 10^{-34}$ J s
Elementary Charge	e	$1.602\ 176\ 53(14) \times 10^{-19}$ C
Bohr Magneton	μ_B	$9.274\ 009\ 49(80) \times 10^{-24}$ J / T
Boltzmann Constant	k_B	$1.380\ 650\ 3(24) \times 10^{-23}$ J / K
Basic Properties of ^{87}Rb		
Atomic Number	Z	37
Atomic Mass	m	$1.443\ 160\ 60(11) \times 10^{-25}$ kg
Natural Abundance		$27.83\,\%$
Nuclear Spin	I	$3/2$
Ground $(5^2S_{1/2})$ State Properties		
Fine Structure Landé g-factor	g_J	$2.002\ 319\ 304\ 373\ 7(80)$
Nuclear g-factor		$-0.000\ 995\ 141\ 4(10)$
Hyperfine Splitting		$6,834,682,610.904\ 34(3)$ Hz
D_2 $(5^2S_{1/2} \rightarrow 5^2P_{3/2})$ Transition		
Wavelength (vacuum)	λ	$780.241\ 209\ 686(13)$ nm
Lifetime	τ	$26.24(4)$ ns
Decay Rate	Γ	$2\pi\ 6.065(9)$ MHz
$\lvert F = 2, m_f = \pm 2 \rangle \rightarrow \lvert F' = 3, m_F = \pm 3 \rangle$		
Saturation	I_{sat}	$1.669(2)$ mW /cm^2
Resonnance Cross Section	σ_0	2.907×10^{-9} cm^2
Scattering Lengths (s-wave)		
Scattering Length for Spin-0 Channel	$a_{F=0}$	$101.8(2)a_0$
Scattering Length for Spin-2 Channel	$a_{F=2}$	$100.4(1)a_0$

REFERENCES

[1] M. H. Anderson, J. R. Ensher, M. R. Matthews, C. E. Wieman, and E. A. Cornell, "Observation of Bose-Einstein Condensation in a Dilute Atomic Vapor," *Science* **269**, 198 (1995).

[2] K. B. Davis, M. O. Mewes, M. R. Andrews, N. J. van Druten, D. S. Durfee, D. M. Kurn, and W. Ketterle, "Bose-Einstein Condensation in a Gas of Sodium Atoms," *Phys. Rev. Lett.* **75**, 3969 (1995).

[3] C. C. Bradley, C. A. Sackett, J. J. Tollett, and R. G. Hulet, "Evidence of Bose-Einstein Condensation in an Atomic Gas with Attractive Interactions," *Phys. Rev. Lett.* **75**, 1687 (1995).

[4] C. C. Bradley, C. A. Sackett, and R. G. Hulet, "Bose-Einstein Condensation of Lithium: Observation of Limited Condensate Number," *Phys. Rev. Lett.* **78**, 985 (1997).

[5] M. R. Andrews, C. G. Townsend, H.-J. Miesner, D. S. Durfee, D. M. Kurn, and W. Ketterle, "Observation of Interference Between Two Bose Condensates," *Science* **275**, 637 (1997).

[6] M.-O. Mewes, M. R. Andrews, D. M. Kurn, D. S. Durfee, C. G. Townsend, and W. Ketterle, "Output Coupler for Bose-Einstein Condensed Atoms," *Phys. Rev. Lett.* **78**, 582 (1997).

[7] E. W. Hagley, L. Deng, M. Kozuma, J. Wen, K. Helmerson, S. L. Rolston, and W. D. Phillips, "A Well-Collimated Quasi-Continuous Atom Laser," *Science* **283**, 1706 (1999).

[8] I. Bloch, T. W. Hänsch, and T. Esslinger, "Atom Laser with a cw Output Coupler," *Phys. Rev. Lett.* **82**, 3008 (1999).

[9] M. Schellekens, R. Hoppeler, A. Perrin, J. V. Gomes, D. Boiron, A. Aspect, and C. I. Westbrook, "Hanbury Brown Twiss Effect for Ultracold Quantum Gases," *Science* **310**, 648 (2005).

[10] A. Öttl, S. Ritter, M. Köhl, and T. Esslinger, "Correlations and Counting Statistics of an Atom Laser," *Phys. Rev. Lett.* **95**, 090404 (2005).

[11] T. Jeltes, J. M. McNamara, W. Hogervorst, W. Vassen, V. Krachmalnicoff, M. Schellekens, A. Perrin, H. Chang, D. Boiron, A. Aspect, and C. I. Westbrook, "Comparison of the Hanbury Brown-Twiss effect for bosons and fermions," *Nature* **445**, 402 (2007).

[12] T. Rom, T. Best, D. van Oosten, U. Schneider, S. Folling, B. Paredes, and I. Bloch, "Free fermion antibunching in a degenerate atomic Fermi gas released from an optical lattice," *Nature* **444**, 733 (2006).

[13] S. Fölling, F. Gerbier, A. Widera, O. Mandel, T. Gericke, and I. Bloch, "Spatial quantum noise interferometry in expanding ultracold atom clouds," *Nature* **434**, 481 (2005).

[14] M. Greiner, C. A. Regal, J. T. Stewart, and D. S. Jin, "Probing Pair-Correlated Fermionic Atoms through Correlations in Atom Shot Noise," *Phys. Rev. Lett.* **94**, 110401 (2005).

[15] A. Perrin, H. Chang, V. Krachmalnicoff, M. Schellekens, D. Boiron, A. Aspect, and C. I. Westbrook, "Observation of Atom Pairs in Spontaneous Four-Wave Mixing of Two Colliding Bose-Einstein Condensates," *Phys. Rev. Lett.* **99**, 150405 (2007).

[16] C.-S. Chuu, F. Schreck, T. P. Meyrath, J. L. Hanssen, G. N. Price, and M. G. Raizen, "Direct Observation of Sub-Poissonian Number Statistics in a Degenerate Bose Gas," *Phys. Rev. Lett.* **95**, 260403 (2005).

[17] A. Itah, H. Veksler, O. Lahav, A. Blumkin, C. Moreno, C. Gordon, and J. Steinhauer, "Direct Observation of a Sub-Poissonian Number Distribution of Atoms in an Optical Lattice," *Phys. Rev. Lett.* **104**, 113001 (2010).

[18] J. Esteve, C. Gross, A. Weller, S. Giovanazzi, and M. K. Oberthaler, "Squeezing and entanglement in a Bose-Einstein condensate," *Nature* **455**, 1216 (2008).

[19] S. Whitlock, C. F. Ockeloen, and R. J. C. Spreeuw, "Sub-Poissonian Atom-Number Fluctuations by Three-Body Loss in Mesoscopic Ensembles," *Phys. Rev. Lett.* **104**, 120402 (2010).

[20] N. Gemelke, X. Zhang, C.-L. Hung, and C. Chin, "In situ observation of incompressible Mott-insulating domains in ultracold atomic gases," *Nature* **460**, 995 (2009).

[21] C. Sanner, E. J. Su, A. Keshet, R. Gommers, Y.-i. Shin, W. Huang, and W. Ketterle, "Suppression of Density Fluctuations in a Quantum Degenerate Fermi Gas," *Phys. Rev. Lett.* **105**, 040402 (2010).

[22] M. Kitagawa and M. Ueda, "Squeezed spin states," *Phys. Rev. A* **47**, 5138 (1993).

[23] D. J. Wineland, J. J. Bollinger, W. M. Itano, and D. J. Heinzen, "Squeezed atomic states and projection noise in spectroscopy," *Phys. Rev. A* **50**, 67 (1994).

[24] J. Hald, J. L. Sørensen, C. Schori, and E. S. Polzik, "Spin Squeezed Atoms: A Macroscopic Entangled Ensemble Created by Light," *Phys. Rev. Lett.* **83**, 1319 (1999).

[25] A. Kuzmich, L. Mandel, and N. P. Bigelow, "Generation of Spin Squeezing via Continuous Quantum Nondemolition Measurement," *Phys. Rev. Lett.* **85**, 1594 (2000).

[26] J. Appel, P. J. Windpassinger, D. Oblak, U. B. Hoff, N. Kjrgaard, and E. S. Polzik, "Mesoscopic atomic entanglement for precision measurements beyond the standard quantum limit," *Proceedings of the National Academy of Sciences* **106**, 10960 (2009).

[27] A. Louchet-Chauvet, J. Appel, J. J. Renema, D. Oblak, N. Kjaergaard, and E. S. Polzik, "Entanglement-assisted atomic clock beyond the projection noise limit," *New Journal of Physics* **12**, 065032 (2010).

[28] M. H. Schleier-Smith, I. D. Leroux, and V. Vuletić, "States of an Ensemble of Two-Level Atoms with Reduced Quantum Uncertainty," *Phys. Rev. Lett.* **104**, 073604 (2010).

[29] M. Koschorreck, M. Napolitano, B. Dubost, and M. W. Mitchell, "Sub-Projection-Noise Sensitivity in Broadband Atomic Magnetometry," *Phys. Rev. Lett.* **104**, 093602 (2010).

[30] W. Wasilewski, K. Jensen, H. Krauter, J. J. Renema, M. V. Balabas, and E. S. Polzik, "Quantum Noise Limited and Entanglement-Assisted Magnetometry," *Phys. Rev. Lett.* **104**, 133601 (2010).

[31] C. Orzel, A. K. Tuchman, M. L. Fenselau, M. Yasuda, and M. A. Kasevich, "Squeezed States in a Bose-Einstein Condensate," *Science* **291**, 2386 (2001).

[32] M. Greiner, O. Mandel, T. Esslinger, T. W. Hansch, and I. Bloch, "Quantum phase transition from a superfluid to a Mott insulator in a gas of ultracold atoms," *Nature* , 39 (2002).

[33] F. Gerbier, S. Fölling, A. Widera, O. Mandel, and I. Bloch, "Probing Number Squeezing of Ultracold Atoms across the Superfluid-Mott Insulator Transition," *Phys. Rev. Lett.* **96**, 090401 (2006).

[34] J. Sebby-Strabley, B. L. Brown, M. Anderlini, P. J. Lee, W. D. Phillips, J. V. Porto, and P. R. Johnson, "Preparing and Probing Atomic Number States with an Atom Interferometer," *Phys. Rev. Lett.* **98**, 200405 (2007).

[35] G.-B. Jo, Y. Shin, S. Will, T. A. Pasquini, M. Saba, W. Ketterle, D. E. Pritchard, M. Vengalattore, and M. Prentiss, "Long Phase Coherence Time and Number Squeezing of Two Bose-Einstein Condensates on an Atom Chip," *Phys. Rev. Lett.* **98**, 030407 (2007).

[36] W. Li, A. K. Tuchman, H.-C. Chien, and M. A. Kasevich, "Extended Coherence Time with Atom-Number Squeezed States," *Phys. Rev. Lett.* **98**, 040402 (2007).

[37] C. Gross, T. Zibold, E. Nicklas, J. Estve, and M. K. Oberthaler, "Nonlinear atom interferometer surpasses classical precision limit," *Nature* **464**, 1165 (2010).

[38] M. F. Riedel, P. Böhi, Y. Li, T. W. Hänsch, A. Sinatra, and P. Treutlein, "Atom-chip-based generation of entanglement for quantum metrology," *Nature* **464**, 1170 (2010).

[39] R. Loudon, *The Quantum Theory of Light*, Third ed. (Oxford University Press, Oxford, 2000).

[40] H.-A. Bachor and T. C. Ralph, *A guide to experiments in quantum optics / Hans-A. Bachor and Timothy C. Ralph*, 2nd, rev. and enlarged ed. ed. (Wiley-VCH, Weinheim ; Chichester :, 2004).

[41] H. Pu and P. Meystre, "Creating Macroscopic Atomic Einstein-Podolsky-Rosen States from Bose-Einstein Condensates," *Phys. Rev. Lett.* **85**, 3987 (2000).

[42] L.-M. Duan, A. Sørensen, J. I. Cirac, and P. Zoller, "Squeezing and Entanglement of Atomic Beams," *Phys. Rev. Lett.* **85**, 3991 (2000).

[43] A. Sorensen, L.-M. Duan, J. I. Cirac, and P. Zoller, "Many-particle entanglement with Bose-Einstein condensates," *Nature* **409**, 63 (2001).

[44] T. Opatrný and G. Kurizki, "Matter-Wave Entanglement and Teleportation by Molecular Dissociation and Collisions," *Phys. Rev. Lett.* **86**, 3180 (2001).

[45] K. V. Kheruntsyan and P. D. Drummond, "Quantum correlated twin atomic beams via photodissociation of a molecular Bose-Einstein condensate," *Phys. Rev. A* **66**, 031602 (2002).

[46] C. M. Savage, P. E. Schwenn, and K. V. Kheruntsyan, "First-principles quantum simulations of dissociation of molecular condensates: Atom correlations in momentum space," *Phys. Rev. A* **74**, 033620 (2006).

[47] K. Mølmer, A. Perrin, V. Krachmalnicoff, V. Leung, D. Boiron, A. Aspect, and C. I. Westbrook, "Hanbury Brown and Twiss correlations in atoms scattered from colliding condensates," *Phys. Rev. A* **77**, 033601 (2008).

[48] K. V. Kheruntsyan, M. K. Olsen, and P. D. Drummond, "Einstein-Podolsky-Rosen Correlations via Dissociation of a Molecular Bose-Einstein Condensate," *Phys. Rev. Lett.* **95**, 150405 (2005).

[49] A. J. Ferris, M. K. Olsen, and M. J. Davis, "Atomic entanglement generation and detection via degenerate four-wave mixing of a Bose-Einstein condensate in an optical lattice," *Phys. Rev. A* **79**, 043634 (2009).

[50] V. Krachmalnicoff, J.-C. Jaskula, M. Bonneau, V. Leung, G. B. Partridge, D. Boiron, C. I. Westbrook, P. Deuar, P. Ziń, M. Trippenbach, and K. V. Kheruntsyan, "Spontaneous Four-Wave Mixing of de Broglie Waves: Beyond Optics," *Phys. Rev. Lett.* **104**, 150402 (2010).

[51] L. Deng, E. W. Hagley, J. Wen, M. Trippenbach, Y. Band, P. S. Julienne, J. E. Simsarian, K. Helmerson, S. L. Rolston, and W. D. Phillips, "Four-wave mixing with matter waves," *Nature* **398**, 218 (1999).

[52] J. M. Vogels, K. Xu, and W. Ketterle, "Generation of Macroscopic Pair-Correlated Atomic Beams by Four-Wave Mixing in Bose-Einstein Condensates," *Phys. Rev. Lett.* **89**, 020401 (2002).

[53] J. M. Vogels, J. K. Chin, and W. Ketterle, "Coherent Collisions between Bose-Einstein Condensates," *Phys. Rev. Lett.* **90**, 030403 (2003).

[54] M. Vengalattore, J. M. Higbie, S. R. Leslie, J. Guzman, L. E. Sadler, and D. M. Stamper-Kurn, "High-Resolution Magnetometry with a Spinor Bose-Einstein Condensate," *Phys. Rev. Lett.* **98**, 200801 (2007).

[55] J. D. Sau, S. R. Leslie, M. L. Cohen, and D. M. Stamper-Kurn, "Spin squeezing of high-spin, spatially extended quantum fields," *New Journal of Physics* **12**, 085011 (2010).

[56] E. L. Raab, M. Prentiss, A. Cable, S. Chu, and D. E. Pritchard, "Trapping of Neutral Sodium Atoms with Radiation Pressure," *Phys. Rev. Lett.* **59**, 2631 (1987).

[57] M. D. Barrett, J. A. Sauer, and M. S. Chapman, "All-Optical Formation of an Atomic Bose-Einstein Condensate," *Phys. Rev. Lett.* **87**, 010404 (2001).

[58] M.-S. Chang, *Coherent Spin Dynamics of a Spin-1 Bose-Einstein Condensate*, PhD thesis Georiga Institute of Technology 2006.

[59] C. Klempt, T. van Zoest, T. Henninger, O. Topic, E. Rasel, W. Ertmer, and J. Arlt, "Ultraviolet light-induced atom desorption for large rubidium and potassium magneto-optical traps," *Phys. Rev. A* **73**, 013410 (2006).

[60] D. A. Steck, "Rubidium 87 D Line Data," 2003.

[61] H. J. Metcalf and P. van der Straten, *Laser Cooling and Trapping* (Springer-Verlag, New York, 1999).

[62] C. J. Foot, *Atomic Physics (Oxford Master Series in Atomic, Optical and Laser Physics)* (Oxford University Press, USA, 2005).

[63] D. J. Han, M. T. DePue, and D. S. Weiss, "Loading and compressing Cs atoms in a very far-off-resonant light trap," *Phys. Rev. A* **63**, 023405 (2001).

[64] T. Kinoshita, T. Wenger, and D. S. Weiss, "All-optical Bose-Einstein condensation using a compressible crossed dipole trap," *Phys. Rev. A* **71**, 011602 (2005).

[65] R. Grimm, M. Weidemüller, and Y. B. Ovchinnikov, "Optical dipole traps for neutral atoms," *Adv. At. Mol. Opt. Phys.* **42**, 95 (2000) physics/9902072.

[66] R. Scheunemann, F. S. Cataliotti, T. W. Hnsch, and M. Weitz, "An optical lattice with single lattice site optical control for quantum engineering," *Journal of Optics B: Quantum and Semiclassical Optics* **2**, 645 (2000).

[67] D. Schrader, I. Dotsenko, M. Khudaverdyan, Y. Miroshnychenko, A. Rauschenbeutel, and D. Meschede, "Neutral Atom Quantum Register," *Phys. Rev. Lett.* **93**, 150501 (2004).

[68] K. D. Nelson, X. Li, and D. S. Weiss, "Imaging single atoms in a three-dimensional array," *Nat Phys* **3**, 556 (2007).

[69] M. J. Gibbons, S. Y. Kim, K. M. Fortier, P. Ahmadi, and M. S. Chapman, "Achieving very long lifetimes in optical lattices with pulsed cooling," *Phys. Rev. A* **78**, 043418 (2008).

[70] G. Reinaudi, T. Lahaye, Z. Wang, and D. Guéry-Odelin, "Strong saturation absorption imaging of dense clouds of ultracold atoms," *Opt. Lett.* **32**, 3143 (2007).

[71] Beer, "Bestimmung der Absorption des rothen Lichts in farbigen Flssigkeiten," *Annalen der Physik* **162**, 78 (1852).

[72] W. Ketterle, D. S. Durfee, and D. M. Stamper-Kurn, "Making, probing and understanding Bose-Einstein condensates (cond-mat/9904034)," in *International School of Physics "Enrico Fermi", Course CXL*, edited by M. Inguscio, S. Stringari, and C. E. Wieman Varenna, Lake Como, Italy 1999 IOS Press.

[73] B. P. Anderson and M. A. Kasevich, "Macroscopic Quantum Interference from Atomic Tunnel Arrays," *Science* **282**, 1686 (1998).

[74] M. Ben Dahan, E. Peik, J. Reichel, Y. Castin, and C. Salomon, "Bloch Oscillations of Atoms in an Optical Potential," *Phys. Rev. Lett.* **76**, 4508 (1996).

[75] M. Albiez, R. Gati, J. Fölling, S. Hunsmann, M. Cristiani, and M. K. Oberthaler, "Direct Observation of Tunneling and Nonlinear Self-Trapping in a Single Bosonic Josephson Junction," *Phys. Rev. Lett.* **95**, 010402 (2005).

[76] D. Jaksch, C. Bruder, J. I. Cirac, C. W. Gardiner, and P. Zoller, "Cold Bosonic Atoms in Optical Lattices," *Phys. Rev. Lett.* **81**, 3108 (1998).

[77] T. Kinoshita, T. Wenger, and D. S. Weiss, "Observation of a One-Dimensional Tonks-Girardeau Gas," *Science* **305**, 1125 (2004).

[78] Z. Hadzibabic, P. Kruger, M. Cheneau, B. Battelier, and J. Dalibard, "Berezinskii-Kosterlitz-Thouless crossover in a trapped atomic gas," *Nature* **441**, 1118 (2006).

[79] O. Morsch and M. Oberthaler, "Dynamics of Bose-Einstein condensates in optical lattices," *Rev. Mod. Phys.* **78**, 179 (2006).

[80] I. Bloch, J. Dalibard, and W. Zwerger, "Many-body physics with ultracold gases," *Rev. Mod. Phys.* **80**, 885 (2008).

[81] A. D. Cronin, J. Schmiedmayer, and D. E. Pritchard, "Optics and interferometry with atoms and molecules," *Rev. Mod. Phys.* **81**, 1051 (2009).

[82] S. Kuhr, W. Alt, D. Schrader, I. Dotsenko, Y. Miroshnychenko, W. Rosenfeld, M. Khudaverdyan, V. Gomer, A. Rauschenbeutel, and D. Meschede, "Coherence Properties and Quantum State Transportation in an Optical Conveyor Belt," *Phys. Rev. Lett.* **91**, 213002 (2003).

[83] O. Mandel, M. Greiner, A. Widera, T. Rom, T. W. Hansch, and I. Bloch, "Controlled collisions for multi-particle entanglement of optically trapped atoms," *Nature* **425**, 937 (2003).

[84] R. Scheunemann, F. S. Cataliotti, T. W. Hänsch, and M. Weitz, "Resolving and addressing atoms in individual sites of a CO_2-laser optical lattice," *Phys. Rev. A* **62**, 051801 (2000).

[85] T. Gericke, P. Wurtz, D. Reitz, T. Langen, and H. Ott, "High-resolution scanning electron microscopy of an ultracold quantum gas," *Nat Phys* **4**, 949 (2008).

[86] S. Friebel, C. D'Andrea, J. Walz, M. Weitz, and T. W. Hänsch, "CO_2-laser optical lattice with cold rubidium atoms," *Phys. Rev. A* **57**, R20 (1998).

[87] C. Pethick and H. Smith, *Bose-Einstein condensation in dilute gases* (Cambridge University Press, 2002).

[88] Y. Castin and R. Dum, "Bose-Einstein Condensates in Time Dependent Traps," *Phys. Rev. Lett.* **77**, 5315 (1996).

[89] F. L. Pedrotti, L. M. Pedrotti, and L. S. Pedrotti, *Introduction to Optics (3rd Edition)*, 3 ed. (Benjamin Cummings, 2006).

[90] M. Kasevich and S. Chu, "Laser cooling below a photon recoil with three-level atoms," *Phys. Rev. Lett.* **69**, 1741 (1992).

[91] Z. Hadzibabic, S. Stock, B. Battelier, V. Bretin, and J. Dalibard, "Interference of an Array of Independent Bose-Einstein Condensates," *Phys. Rev. Lett.* **93**, 180403 (2004).

[92] G. Cennini, C. Geckeler, G. Ritt, and M. Weitz, "Interference of a variable number of coherent atomic sources," *Phys. Rev. A* **72**, 051601 (2005).

[93] T.-L. Ho, "Spinor Bose Condensates in Optical Traps," *Phys. Rev. Lett.* **81**, 742 (1998).

[94] C. K. Law, H. Pu, and N. P. Bigelow, "Quantum Spins Mixing in Spinor Bose-Einstein Condensates," *Phys. Rev. Lett.* **81**, 5257 (1998).

[95] W. Zhang, D. L. Zhou, M.-S. Chang, M. S. Chapman, and L. You, "Coherent spin mixing dynamics in a spin-1 atomic condensate," *Phys. Rev. A* **72**, 013602 (2005).

[96] M.-S. Chang, Q. Qin, W. Zhang, L. You, and M. S. Chapman, "Coherent spinor dynamics in a spin-1 Bose condensate," *Nat Phys* **1**, 111 (2005).

[97] L.-M. Duan, J. I. Cirac, and P. Zoller, "Quantum entanglement in spinor Bose-Einstein condensates," *Phys. Rev. A* **65**, 033619 (2002).

[98] W. Zhang, S. Yi, and L. You, "Mean field ground state of a spin-1 condensate in a magnetic field," *New Journal of Physics* **5**, 77 (2003).

[99] L. E. Sadler, J. M. Higbie, S. R. Leslie, M. Vengalattore, and D. M. Stamper-Kurn, "Spontaneous symmetry breaking in a quenched ferromagnetic spinor Bose-Einstein condensate," *Nature* **443**, 312 (2006).

[100] M.-S. Chang, C. D. Hamley, M. D. Barrett, J. A. Sauer, K. M. Fortier, W. Zhang, L. You, and M. S. Chapman, "Observation of Spinor Dynamics in Optically Trapped ^{87}Rb Bose-Einstein Condensates," *Phys. Rev. Lett.* **92**, 140403 (2004).

[101] M. Vengalattore, S. R. Leslie, J. Guzman, and D. M. Stamper-Kurn, "Spontaneously Modulated Spin Textures in a Dipolar Spinor Bose-Einstein Condensate," *Phys. Rev. Lett.* **100**, 170403 (2008).

[102] S. R. Leslie, J. Guzman, M. Vengalattore, J. D. Sau, M. L. Cohen, and D. M. Stamper-Kurn, "Amplification of fluctuations in a spinor Bose-Einstein condensate," *Phys. Rev. A* **79**, 043631 (2009).

[103] C. Klempt, O. Topic, G. Gebreyesus, M. Scherer, T. Henninger, P. Hyllus, W. Ertmer, L. Santos, and J. J. Arlt, "Multiresonant Spinor Dynamics in a Bose-Einstein Condensate," *Phys. Rev. Lett.* **103**, 195302 (2009).

[104] C. Klempt, O. Topic, G. Gebreyesus, M. Scherer, T. Henninger, P. Hyllus, W. Ertmer, L. Santos, and J. J. Arlt, "Parametric Amplification of Vacuum Fluctuations in a Spinor Condensate," *Phys. Rev. Lett.* **104**, 195303 (2010).

[105] M. Scherer, B. Lücke, G. Gebreyesus, O. Topic, F. Deuretzbacher, W. Ertmer, L. Santos, J. J. Arlt, and C. Klempt, "Spontaneous Breaking of Spatial and Spin Symmetry in Spinor Condensates," *Phys. Rev. Lett.* **105**, 135302 (2010).

[106] J. Kronjäger, C. Becker, P. Soltan-Panahi, K. Bongs, and K. Sengstock, "Spontaneous Pattern Formation in an Antiferromagnetic Quantum Gas," *Phys. Rev. Lett.* **105**, 090402 (2010).

[107] T. Ohmi and K. Machida, "Bose-Einstein Condensation with Internal Degrees of Freedom in Alkali Atom Gases," *Journal of the Physical Society of Japan* **67**, 1822 (1998).

[108] H. Pu, C. K. Law, S. Raghavan, J. H. Eberly, and N. P. Bigelow, "Spin-mixing dynamics of a spinor Bose-Einstein condensate," *Phys. Rev. A* **60**, 1463 (1999).

[109] W. Zhang, D. L. Zhou, M.-S. Chang, M. S. Chapman, and L. You, "Dynamical Instability and Domain Formation in a Spin-1 Bose-Einstein Condensate," *Phys. Rev. Lett.* **95**, 180403 (2005).

[110] H. Saito and M. Ueda, "Spontaneous magnetization and structure formation in a spin-1 ferromagnetic Bose-Einstein condensate," *Phys. Rev. A* **72**, 023610 (2005).

[111] H. Saito, Y. Kawaguchi, and M. Ueda, "Breaking of Chiral Symmetry and Spontaneous Rotation in a Spinor Bose-Einstein Condensate," *Phys. Rev. Lett.* **96**, 065302 (2006).

[112] A. Lamacraft, "Quantum Quenches in a Spinor Condensate," *Phys. Rev. Lett.* **98**, 160404 (2007).

[113] J. D. Sau, S. R. Leslie, D. M. Stamper-Kurn, and M. L. Cohen, "Theory of domain formation in inhomogeneous ferromagnetic dipolar condensates within the truncated Wigner approximation," *Phys. Rev. A* **80**, 023622 (2009).

[114] D. J. Wineland, J. J. Bollinger, W. M. Itano, F. L. Moore, and D. J. Heinzen, "Spin squeezing and reduced quantum noise in spectroscopy," *Phys. Rev. A* **46**, R6797 (1992).

[115] O. E. Müstecaplıoğlu, M. Zhang, and L. You, "Spin squeezing and entanglement in spinor condensates," *Phys. Rev. A* **66**, 033611 (2002).